THE INFLUENCE OF NEARSHORE BARS ON INFRAGRAVITY ENERGY AT THE SHORELINE

A Thesis

by

NICHOLAS CARROLL COX

Submitted to the Office of Graduate Studies of
Texas A&M University
in partial fulfillment of the requirements for the degree of

MASTER OF SCIENCE

December 2011

Major Subject: Civil Engineering

THE INFLUENCE OF NEARSHORE BARS ON INFRAGRAVITY ENERGY AT THE SHORELINE

A Thesis

by

NICHOLAS CARROLL COX

Submitted to the Office of Graduate Studies of
Texas A&M University
in partial fulfillment of the requirements for the degree of

MASTER OF SCIENCE

Approved by:

Co-Chairs of Committee,	Jennifer Irish
	James Kaihatu
Committee Members,	Robert Weiss
Head of Department,	John Niedzwecki

December 2011

Major Subject: Civil Engineering

ABSTRACT

The Influence of Nearshore Bars on Infragravity Energy

at the Shoreline. (December 2011)

Nicholas Cox, B.S., Clemson University

Co-Chairs of Advisory Committee, Dr. Jennifer Irish
Dr. James Kaihatu

Bathymetric features such as nearshore sandbars can alter local nearshore hydrodynamic processes such as the production of infragravity energy. These bathymetric features may act to reduce or increase the amount of infragravity energy that reaches the shoreline. To determine the influence of the bathymetric features on infragravity energy, the numerical nearshore processes model XBeach was used to simulate infragravity energy at the shoreline. Numerical simulations were completed for three types of bathymetric scenarios: continuous alongshore bar, bar-rip, and no-bar.

The presence of the bar reduces the amount of infragravity energy at the shoreline when compared with the no-bar scenario. This reduction was characterized by modifying an empirical parameterization for significant infragravity swash developed by Stockdon et al. (2006) for barred beaches. Results show that the amount of infragravity energy in the form of swash is dependent on the bar height and depth, in addition to the offshore wave height and wavelength.

The bar-rip bathymetry produces significant alongshore variation in infragravity energy. The alongshore variations may be due to refracted wave energy or the production

of an edge wave by the rip. The magnitude of infragravity energy in the alongshore direction is found to be correlated with the surf zone width. Finally, erosion for the bar-rip scenario is studied qualitatively. The shape of the shoreline is modified during storm events, and is found to take the shape of the alongshore distribution of infragravity energy.

Since infragravity swash influences beach erosion, results of this research may be used as part of an erosion vulnerability scale. Such information on erosion vulnerability is important for the design of coastal protection systems and the protection of coastal communities.

ACKNOWLEDGEMENTS

I first must thank Dr. Jennifer Irish for providing me with the opportunity to work on this research project. Working with her has been an invaluable experience, and this research would not have been possible without the wealth of knowledge that she has provided in all aspects of this work. I also would like to thank my committee members, Dr. James Kaihatu and Dr. Robert Weiss for their time spent reviewing, and their thoughts on this thesis. I must also thank the sponsor of this research, Joint Airborne Lidar Bathymetry Technical Center of Expertise, for providing this research. Finally, I would like to thank Jordan Schaefer for his help throughout this project.

NOMENCLATURE

$\hat{A}$	profile scale factor for equilibrium profile
A	wave action balance
a	wave amplitude
a_b	breaking wave amplitude
A_s	sediment transport coefficient
a_s	swash amplitude
C	depth averaged sediment concentration
$\hat{c}$	sediment concentration
c	wave celerity
C_d	drag coefficient
C_{eq}	equilibrium sediment concentration
c_g	group velocity
D	wave dissipation due to friction
D_b	expected value of wave dissipation
D_{HIGH}	elevation of dune crest
D_{LOW}	elevation of dune toe
D_s	sediment diffusion coefficient
D_w	wave energy dissipation
E_w	wave energy
f	wave frequency
f	Coriolis force
F	momentum flux
F_x	wave stress in x-direction

F_y	wave stress in y-direction
g	gravity
h	water depth
H	wave height
H_0	offshore wave height
h_B	depth of bar
H_b	wave breaking height
H_{max}	maximum wave height
H_{rms}	root mean square wave height
$H_{s,\infty}$	deep water significant wave height
k	wave number
KE	kinetic energy
L	wavelength
L_0	offshore wavelength
m	constant in equilibrium profile
p	pressure
PE	potential energy
Q_b	probability of wave breaking
R_2	two-percent runup
R_{HIGH}	high runup value
R_{LOW}	low runup value
S_{IG}	significant infragravity swash
S_m	momentum part of wave radiation stress
S_r	roller energy

S_w	wave radiation stress
S_{xx}	wave radiation stress
T	wave period
T_{rep}	representative wave period
T_s	sediment adaptation time
u	wave velocity
$\bar{u}$	depth averaged velocity
u_{rms}	root mean square orbital velocity
y	offshore distance from shoreline for equilibrium profile
α	factor in wave energy dissipation equation
α_b	bed slope calibration factor
β	beach slope
β_f	beach face slope
γ_{max}	wave breaking index
ε	vertical turbulent diffusion
η	water surface elevation
$\bar{\eta}_{max}$	maximum setup at the shoreline
$\bar{\eta}$	setup / setdown
θ	wave angle of incidence
ν_h	horizontal viscosity
ξ	Iribarren Number
$\xi_{0,storm}$	storm Iribarren number
ξ_b	surf similarity parameter
ρ	water density

σ	intrinsic wave frequency
τ	bed shear stress
ω	incident wave frequency

TABLE OF CONTENTS

Page

LIST OF FIGURES

Page

Page

Page

LIST OF TABLES

Page

1 INTRODUCTION

1.1 Importance of Research

Beaches are often the first line of defense for coastal communities, and serve as protection against the large waves that are produced by storms. Topographical features such as wide berms and large dunes are able to absorb the energy of the waves as they crash into the beach. However, the role of local nearshore bathymetric features in the protection of a beach during a storm is not well known. Bathymetric features such as nearshore sandbars may alter the local nearshore hydrodynamics. Specifically, these bathymetric features may act to protect the beach through a reduction of wave energy or to facilitate erosion in certain areas. Investigating the role of local nearshore bathymetric features during a storm can aid in determining areas of a beach that may or may not need additional coastal defenses such as beach nourishments or seawalls.

1.2 Overview of Research Methods

The goal of this research is to identify the influence of nearshore sandbars and bar-rips on infragravity energy at the shoreline. Specifically, the infragravity energy is studied in the form of the two-percent runup and significant infragravity swash of long waves (Stockdon et al., 2006). In order to do this, bathymetric LiDAR data is analyzed to determine the cross-shore spatial distribution of sandbars in the nearshore zone. This information is then used to determine different bathymetric scenarios. The influence of these bathymetric scenarios is tested with the numerical model XBeach (eXtreme beach

---

This thesis follows the style of Coastal Engineering.

behavior). XBeach is a nearshore processes model that simulates the propagation and dissipation of wave groups, and effectively simulates infragravity waves and their effect on nearshore processes (Roelvink et al., 2009). Simulations are completed that are designed to test how the wave height and cross-shore spatial distribution of nearshore bar and bar-rips influence the infragravity energy at the shoreline. The two-percent runup and significant infragravity swash are then calculated using data output from the numerical model. In order to assist in analyzing the infragravity energy data, wave breaking for each simulation is also investigated. The two-percent runup and significant infragravity swash are used to determine the influence that the presence of nearshore sandbars and bar-rips have on infragravity energy at the shoreline.

1.3 Thesis Organization

This thesis is divided into 5 sections. This section has described the importance of this work, and given an introduction to the research that was completed. Section 2 provides an overview of the scientific background for this thesis by presenting existing research that pertains to this work. This includes a review of nearshore sandbars, nearshore processes, infragravity energy in the form of runup and swash, and modeling of nearshore processes. The third section gives a thorough description of the methods used, including determining the different bathymetric scenarios to test, the inputs for the numerical model, and methods used to calculate the two-percent runup and significant infragravity swash. The fourth section displays major results of the research, and finally the fifth section provides a conclusion of all major findings.

2 BACKGROUND AND LITERATURE REVIEW

2.1 Introduction

In the past decade, hurricanes such as Hurricane Katrina and Hurricane Ike have served as reminders to the extensive damage that occurs when an area is impacted by an extreme storm. These disasters severely impact society in the United States, resulting in the loss of life, as well as billions of dollars in damage to the economy (McComb, 2011). In order to reduce this damage, coastal defenses such as beach nourishment, restoration of wetlands, or seawalls can be strategically placed in regions that are most vulnerable to these extreme storms. However, these types of projects cost on the order of millions of dollars (e.g. Davis et al., 2000, Parsons et al., 2001), and in order to efficiently protect the coast, the vulnerability of different regions of the coast should be quantified in order to protect the most susceptible regions.

It is well known that the onshore topography of an area plays a vital role in the amount of damage a region sustains due to a storm. For example, areas behind large beach and dune systems are less susceptible to hurricanes than areas behind narrow beaches and no dunes (Sallenger, 2000). However. it is not well known what effects different features of the nearshore bathymetry, such as nearshore sandbars and beach cusps, have on the vulnerability of a region. Specifically, the geometry and spatial variation of these features may play a role in the amount of wave energy that reaches the shore. It is known that nearshore sandbars have a greater influence at low tide (Stockdon et al., 2006), and in general when the water level above the sandbar is lower. Therefore, this thesis will study how the location of nearshore sandbars will affect beaches during

extreme storm events for the time period before the surge inundates the nearshore region. This period is important as severe erosion may occur due to the direct impact of large waves on the beach. To determine the effect of the nearshore sandbars on the beach, indicators of beach vulnerability such as wave runup and infragravity swash will be studied. These results can be used as part of a beach erosion vulnerability scale based on nearshore bathymetry. This scale can be used in making informed decisions about the implementation of smart coastal defenses.

2.2 Nearshore Bathymetry

In order to study the role that nearshore sandbars play in the vulnerability of a beach during a storm event, it is important to have a general knowledge of nearshore bathymetry and expected bathymetric evolution during a storm. The following section describes theories behind basic nearshore bathymetric profiles, with a brief review of characteristics of beaches with nearshore sandbars. Also, general ideas behind sandbar formation are given, as the exact mechanism that causes nearshore sandbar formation and subsequent migration is not fully understood (Dulou et al., 2002).

To describe a beach profile in its most basic shape, the general form of the equilibrium beach profile is used. The equilibrium beach profile is the result of various forces acting on sediment in the nearshore zone. These forces can be either constructive or destructive with regard to sediment accreting or eroding. Constructive forces include normal daily wave action, while destructive forces include gravity, which tends to flatten the profile (Dean and Dalrymple, 2002). When the forces are equal, the equilibrium

beach profile is the result (Dean and Dalrymple, 2002). The main assumption of the equilibrium beach profile is that its shape is generally determined by the turbulence in the surf zone that is introduced by breaking waves. The turbulence is considered to be represented by the amount of energy that is dissipated as the waves break. The basic concept is the idea that a sediment particle with particular dimensions is able to withstand a certain amount of wave energy dissipation (Dean and Dalrymple, 2002). If this amount of dissipation is reached, the sediment particle is no longer in equilibrium, and is transported elsewhere. The equilibrium profile is given in the following equation, where h is the water depth, and y is the distance from the shoreline, which is described as the interface between land and water (Dean and Dalrymple, 2002).

$$h(y) = \widehat{A}y^m \tag{2-1}$$

The profile scale factor $\widehat{A}$ is a function of sediment grain size, and along with the exponent m, varies by geographic location. The equilibrium beach profile is used for many different coastal engineering purposes, such as designing beach nourishment, and will be used in this thesis as an aid to create an accurate cross-shore bathymetric profile.

The equilibrium beach profile does not describe nearshore sandbars, so a more complex description of the nearshore profile is necessary (Dean and Dalrymple, 2002). The nearshore bathymetric features of an area are dependent on several factors, with two important factors being the local wave environment and sediment characteristics. Based on these, a nearshore bathymetric profile will take a dissipative form, a reflective form, or one of four intermediate forms which have both dissipative and reflective characteristics. These include (in order of increasing reflective characteristics, and

decreasing dissipative characteristics) 1 – longshore bar-trough, 2 – rhythmic bar and beach, 3- transverse bar and rip, and 4 – ridge-runnel or low tide terrace (Wright and Short, 1984). Of these, the longshore bar-trough profiles, as well as a longshore bar-trough profile with a rip added, are studied in this thesis. The longshore bar-trough profile is usually found in areas with moderate breaker heights and a small tidal range, typically on the order of 1m or less. This profile type develops from a preceding dissipative profile as a change in wave conditions causes sediment to accrete and a bar is formed (Wright et al., 1986). General characteristics of the longshore bar-trough include a shallow bar with a steep shoreward face, a deep trough, and a relatively steeper beach face (Wright et al., 1986). The dissipative portion of this profile is the bar, which usually has a mild offshore slope. A typical longshore bar-trough profile is shown in Figure 2-1.

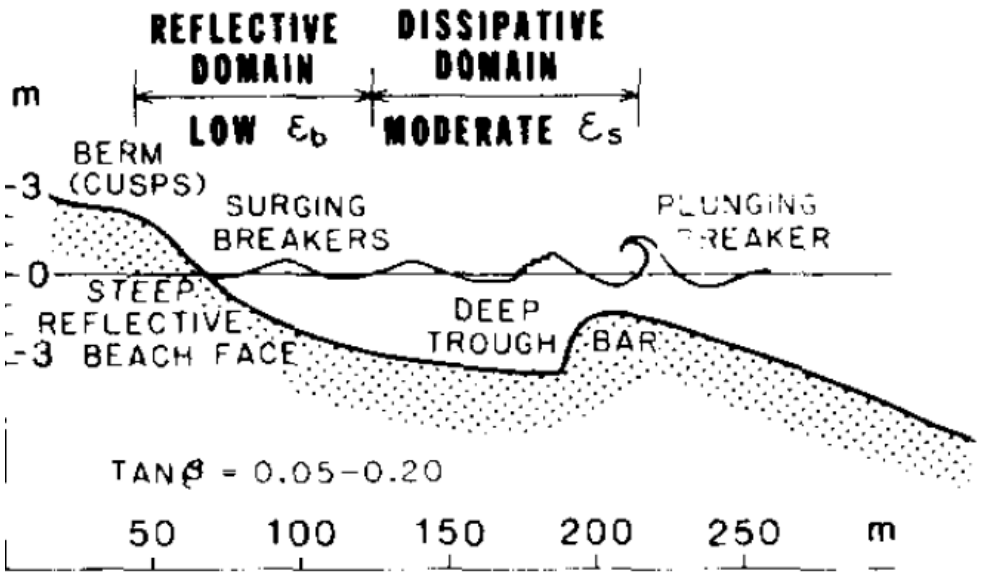

Figure 2-1 Longshore Bar-Trough Profile. The bathymetry studied in this thesis is referred to as a longshore bar-trough profile. This is a dissipative profile; the waves break over the bar, then reform over the deeper trough (From Wright and Short, 1984).

As incident waves approach the bar, the wave shoals and eventually the wave breaks and energy is dissipated over the bar. The wave then reforms over the deep trough and approaches the steeper beach face. Depending on the wave steepness and beach face slope, the wave is described as either a spilling, plunging or surging wave. This is defined by the Iribarren number, or surf similarity parameter, where β is the beach slope, H_0 is the deep water wave height, and L_0 is the deep water wavelength.

$$\xi = \frac{\tan\beta}{\sqrt{\frac{H_0}{L_0}}} \tag{2-2}$$

Each wave type results in an uprush of water on the beach face, a characteristic of reflective beaches. This uprush is known as swash, which is studied in this thesis and will be discussed later. The nearshore bathymetry used in this thesis is representative of a typical longshore bar-trough beach profile.

Many different theories and models have been proposed for the migration of nearshore sandbars. However, all of these include the variation of wave heights with the distance from the shoreline (Dulou et al., 2002). This is illustrated in the breakpoint model, in which a breaking plunging wave creates a jet of water that reaches the bottom and erodes sediment which then forms the bar. Therefore, if larger wave heights exist as they do during storm conditions, waves break further offshore, moving the bar in the offshore direction (Dean and Dalrymple, 2002).

2.3 LiDAR data

In order to understand how wave energy is affected by nearshore bathymetric

features, it is necessary to have an accurate view of the spatial extent and size of the bathymetric features being studied. This requires high resolution bathymetric data. Without this information, it is not possible to accurately predict how a certain sandbar will affect the amount of erosion on a beach during an extreme storm event. Therefore, high resolution data is an important part of the research done for this thesis.

The topic of this research involves the effects of sandbars on the vulnerability of beaches in the nearshore region. In order for a numerical study to be completed, it is necessary to use a grid that accurately reflects nearshore sandbars that occur in nature. According to Plant et al. (2009), appropriate smoothing of raw bathymetric data is necessary for creating an accurate computational grid. Over-smoothing of the bathymetry can result in large wave height errors, leading to large modeling uncertainties. Therefore, depending on the scales of the processes in the model, the data output is coupled to the accuracy of the computational grid that is used as input. As can be seen in Figure 2-2, there is a balance between over-smoothing and under-smoothing bathymetric data for use in a numerical model. Small-scale variations in the bathymetry such as sand ripples may need to be smoothed, while large scale variations such as sand bars should be maintained. The x-axis in Figure 2-2 represents the smoothing scale, while the y-axis represents wave height error.

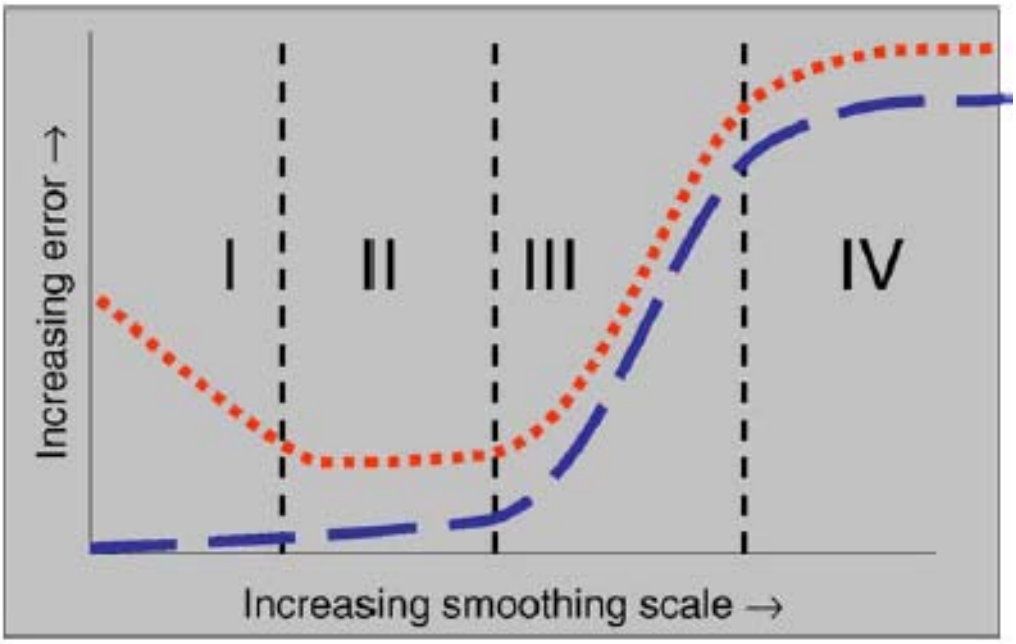

Figure 2-2 Bathymetric Smoothing Scale.The amount of smoothing to raw bathymetric data can have a large effect on wave heights. The x-axis in this figure represents the smoothing scale, while the y-axis represents wave height error. Small-scale variations in the bathymetry should be smoothed, while large scale variations should not be smoothed (From Plant et al., 2009).

Another requirement for the work done in this thesis is the availability of high resolution bathymetric data in the alongshore and cross-shore direction. For instance, if raw bathymetric data is used that only describes a cross-shore nearshore bathymetric profile every 100 m, a nearshore sandbar that exists may not be captured by the data. In order to test the effect of bars and bar-rips on coastal vulnerability, the spatial variations of the bars and bar-rips, as well as the variations in bar and bar-rip dimensions must be known. To satisfy the requirements for high density data in both the alongshore and the cross-shore directions, LiDAR (Light Detection and Ranging) data is used for this thesis. LiDAR data is highly accurate, with vertical accuracies around 15 cm and horizontal accuracies of about 1 m (Irish et al., 2000), and is readily available for most of the

United States coastline. The accuracy of LiDAR data leads to its use in the study of dune microtopography, beach volume change due to hurricanes, and other coastal applications where accurate measurements of either topography or bathymetry are necessary (e.g. Brock and Purkis, 2009, Wozencraft and Millar, 2005, Robertson et al., 2007). LiDAR data is an important resource for this thesis, and has become a fundamental tool for the study of the coastal region, leading to a greater knowledge of the nearshore region and a better understanding of the nearshore processes (Brock et al., 2002, Brock and Purkis, 2009).

2.4 Storm Impact Scale

The following section discusses the ideas behind a storm impact scale, and the importance of a type of beach vulnerability scale that depends on nearshore bathymetric features.

By determining the magnitude of a storms impact on a beach compared to the magnitude of nearshore bathymetric features, such as a sandbar, an impact scale can be created as in Sallenger (2000). This scale can be used to better describe how a certain sandbar might affect a beach during an extreme storm event. This is because the geologic impact of an extreme storm on a section of beach is not only dependent on parameters directly related to the storm, such as wave heights, but also on the bathymetry of the region being impacted (Sallenger, 2000). This includes the type of morphological features found in the area, as well as the size and spatial arrangement of those features. For example, the impact of a storm with 3 m wave heights on an area

without a nearshore sandbar may be greater than that of a storm with 5 m wave heights on an area with nearshore sandbars. Also, the effect may be different for bars located at different distances from the shoreline, and for bars at different depths. In order to determine this effect, indicators of erosion such as wave runup and energy dissipation can be compared to the amount of sand that is eroded on the beach. It is important to note that this type of scale is different than scales such as the Saffir-Simpson hurricane wind scale, which is meant for scaling the wind speed of a hurricane, but is mistakenly used for predicting the impacts of hurricanes on beaches (Sallenger, 2000).

An example of such a scale is the impact scale for barrier islands by Sallenger (2000). The impact of a storm event on a barrier island was split into four distinct regimes. Each regime has unique characteristics associated with the impact on the barrier island, as within each regime the sediment transport pattern is different. Transitions between regimes represent periods where the magnitude of the impact of the storm on a beach changes considerably. The four regimes defined by Sallenger (2000) are based on four parameters; the maximum and minimum runup, R_{HIGH}, and R_{LOW}, and the highest and lowest elevations of the dune, D_{HIGH} and D_{LOW}. These four parameters are illustrated in Figure 2-3.

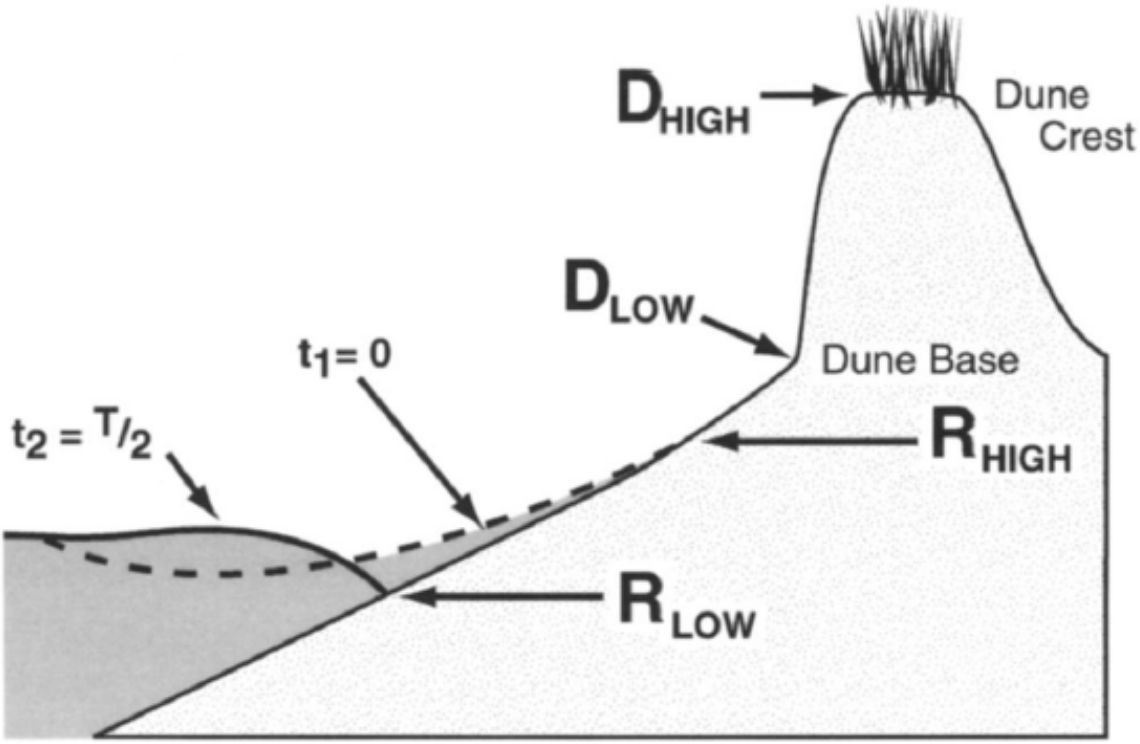

Figure 2-3 Sallenger (2000) Impact Regimes. The parameters used to describe the impact scale (From Sallenger, 2000).

The first regime is defined as the "swash regime", and is the period of time when the runup is less than the minimum dune elevation, described as the first threshold value (Sallenger, 2000).

$$\frac{R_{HIGH}}{D_{HIGH}} = \frac{D_{LOW}}{D_{HIGH}} \tag{2-3}$$

During this regime, time averaged sediment transport yields no net change at the beach, as the storm erodes sand from the beach, only to have it returned by wave action after the storm passes. As the wave heights increase, eventually the runup reaches the dune.

This is the second regime and is described as the “collision regime”, where the threshold value in the above equation is surpassed (Sallenger, 2000). During this regime, the sand that is eroded from the dune is not returned to the dune, yielding net erosion when time averaged over the regime. As the storm progresses, a third regime can be reached. This is known as the “overwash regime,” and is defined as the point where R_{HIGH} is greater than D_{HIGH} (Sallenger, 2000). During this regime, the dune is repeatedly overwashed by runup, as the water level increases due to the combination of storm surge and wave setup. The sand that is eroded is carried inland, where it is deposited, leading to possible net inland migration of the barrier island. The final regime is the “inundation regime,” and is defined as the point where the barrier island is inundated by water, and R_{LOW} is greater than D_{HIGH} (Sallenger, 2000). During this regime the processes acting on the top of the dune are no longer confined to runup. These processes are more complicated, and less understood than those of the previous regimes (Sallenger, 2000). These regimes are significant, as the beach is affected differently during each of them. The impact of a storm on a beach can be scaled based on each of these regimes.

The local bathymetry can affect how a beach is impacted by a storm event. A scale such as the one used by Sallenger (2000) for dune variations on barrier islands does not exist for nearshore bathymetry. It is the goal of this research to determine how nearshore sandbars affect the vulnerability of beaches during storms. This information may be used in a scale such as the one created by Sallenger (2000).

2.5 Nearshore Processes

2.5.1 Nearshore Processes Introduction

In order to properly plan for coastal defenses along coastlines that are affected by hurricanes and other large storm events, it is important to know how the nearshore bathymetry affects the nearshore processes that govern erosion. Variables associated with the spatial configuration of nearshore sandbars, such as the distance between the bar and the shoreline and the depth of the bar, may affect erosion rates during storm events. Also, the width of the area between adjacent sandbars, which is known as a rip, may cause local areas of increased erosion. To study the interaction between these nearshore bathymetric features and nearshore processes such as infragravity motions at the shoreline, a numerical model is used. In order for the numerical model to be accurate, it must simulate many processes that occur throughout the nearshore region. The following section describes these processes.

2.5.2 Refraction, Shoaling and Diffraction

Waves propagating from offshore eventually reach the shallow water near the shore, called the nearshore region, and begin to interact with the local bathymetry. This results in wave shoaling, refraction, and diffraction. As the waves reach shallow water, the decrease in depth causes the wave length to decrease. This is governed by the dispersion relationship, which refers to frequency dispersion (Dean and Dalrymple, 2002). Frequency dispersion is the relationship between wavelength and wave speed. In the following equations, h is the water depth, L is the wavelength, T is the wave period, σ is the angular frequency of the wave, and k is the wave number.

$$\sigma^2 = gk \tanh kh \tag{2-4}$$

$$\sigma = \frac{2\pi}{T} \tag{2-5}$$

$$k = \frac{2\pi}{L} \tag{2-6}$$

The wave period is constant, causing the wave speed to decrease. The wave energy flux must be conserved, and in order to compensate for the decrease in wave speed, the wave height increases (Dean and Dalrymple, 2002). This is known as shoaling. If a wave reaches the shoreline at an angle, the local decrease in wave speed at the section of the wave in shallower water causes the wave to change direction, a process known as refraction. Finally, diffraction occurs as a wave interacts with an object that protrudes from the surface of the water, such as a breakwater. As the wave passes by the object, the interaction results in the wave turning towards the structure. Wave shoaling, refraction and diffraction are all fundamental nearshore processes, and should be considered if applicable to the problem being studied. In this thesis, shoaling and refraction are considered, as they are simulated in the numerical model that is used. Shoaling will occur in all simulations as the waves enter shallow water, while refraction will occur in the bar-rip simulations, as the wave interacts with the bathymetry where the bar and rip meet. Refraction should not occur in the bar and no-bar simulations as the waves approach the shoreline at a 90 degree angle, and the bathymetry is such that the wave will always be in the same water depth in the alongshore direction.

2.5.3 Wave Energy, Breaking and Dissipation

As waves reach the nearshore zone, they carry energy obtained from the wind. This energy takes the form of both potential and kinetic energy. The potential energy and the kinetic energy of a wave are equal, as seen below (Dean and Dalrymple, 1984).

$$KE = PE = \frac{1}{16}\rho g H^2 \tag{2-7}$$

The total wave energy is then defined in the following equation.

$$E = \frac{1}{8}\rho g H^2 \tag{2-8}$$

Wave energy propagates from offshore into the nearshore region, where wave breaking occurs, and wave energy is dissipated. The process of wave breaking is important for nearshore hydrodynamics. The basic variables that describe wave breaking are wave height and water depth. McCowan (1894) first described where wave breaking begins as the point where the ratio of wave height to water depth reaches a threshold known as the breaking index.

$$\left(\frac{H}{h}\right)_{max} = \gamma_{max} \tag{2-9}$$

This description of wave breaking limits waves with a certain amount of energy to breaking at a certain water depth. However, waves of any energy may be breaking or not at a given point (Roelvink, 1993). Therefore, a more appropriate description of wave breaking may be a probabilistic approach, where the probability of breaking increases with increasing wave energy and decreasing water depth. The probability of wave breaking described by Roelvink et al. (2009) is given in the following equations.

$$Q_b = 1\text{-}\exp\left(-\left(\frac{H_{rms}}{H_{max}}\right)^n\right) \tag{2-10}$$

$$H_{rms} = \sqrt{\frac{8E_w}{\rho g}} \tag{2-11}$$

$$H_{max} = \frac{\gamma \tanh kh}{k} \tag{2-12}$$

The probability of wave breaking stays high as the ratio of wave height to water depth is maintained. If it is not, the probability of wave breaking decreases and the wave may cease breaking until the probability of breaking increases, and the wave may begin to break again.

Wave energy dissipation is a complex process, and cannot be measured directly (Roelvink, 1993). An estimation of wave energy dissipation, averaged over all wave directions, is found as the product of the probability of wave breaking as given in Equation (2-10), and the expected value of dissipation, D_b (Roelvink, 1993).

$$D_w = D_b Q_b \tag{2-13}$$

$$D_b = 2\frac{\alpha}{T_{rep}} E_w \tag{2-14}$$

Wave breaking normally results in a region of turbulent whitewater. This bore-like area of the wave is defined as a surface roller, and can be thought of as a volume of water being carried by the wave that travels at the same speed of the wave (Svendsen,

1984). The surface roller carries its own energy, obtained from the breaking wave. The roller energy also dissipates as the wave continues to break. The roller energy is related to wave energy dissipation as well as the roller energy dissipation. The energy of the surface roller adds to the energy of the wave. This increases the radiation stress, which acts to move the location of maximum setdown shoreward. Radiation stress and setdown are discussed in the following section. The surface roller can be visualized as the gray region in Figure 2-4.

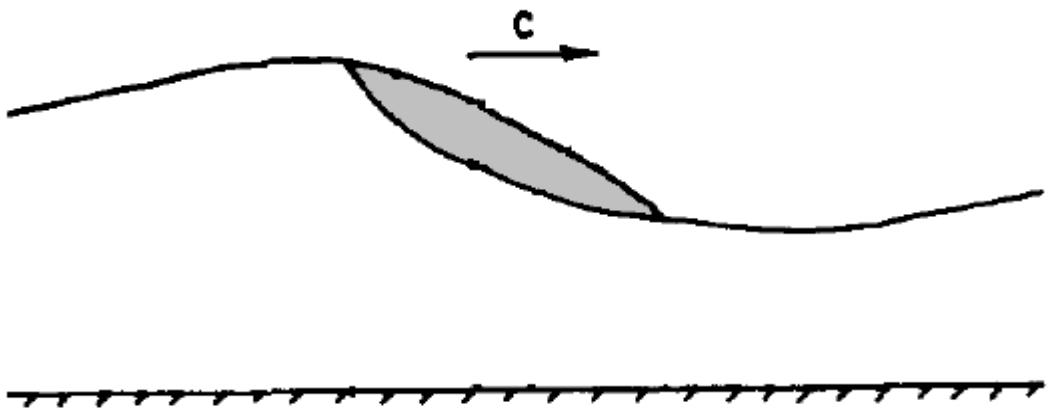

Figure 2-4 Surface Roller. The surface roller is the turbulent whitewater that travels along with the wave after wave breaking. The roller is the gray region of the figure (Modified from Svendsen, 1984).

2.5.4 Setup and Setdown

The shoreline is defined as the location where the water meets the land. The elevation of the shoreline above the still water level changes in time as waves impact the beach, and the water rushes up and subsequently back down the beach face. Further, the

height of the shoreline can be decomposed into two parts, wave setup and swash, which are often combined to describe wave runup. Wave setup is then the time averaged water level elevation above still water level at the shoreline, while swash is defined as the water level variations about the setup. Setup is discussed in this section, while runup and swash are discussed Section 2.5.6. Figure 2-5 illustrates the definitions of setup, $\bar{\eta}$, swash, η' and runup, R.

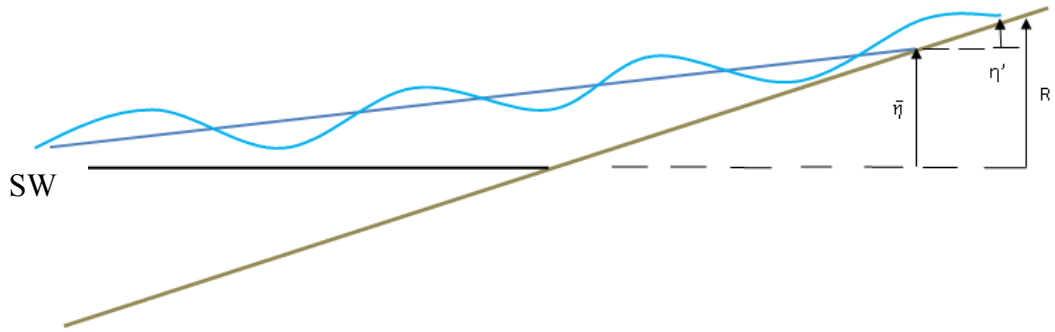

Figure 2-5 Illustration of Setup, Swash, and Runup. Setup is defined as the mean water level at the shoreline, while swash is the variation in the water level about the setup. Runup is then the setup added to the swash.

As waves propagate through the nearshore region they carry energy and momentum. The wave energy is eventually dissipated in the form of breaking; however the excess momentum of the wave is transferred to the water column. According to linear wave theory, the time averaged momentum flux of a wave traveling perpendicular to the coast for a unit width is given as the following equation (Svendsen, 1984).

$$F = \overline{\int_{-h}^{\eta} (\rho u^2 + p)\, dz} \qquad (2\text{-}15)$$

However, some of this momentum flux is due to the pre-existing hydrostatic

pressure. The term radiation stress is then introduced as the momentum flux due purely to the wave. This term was first introduced by Longuet-Higgins and Stewart (1962).

$$S_{xx} = F- \frac{1}{2}\rho g h^2 \tag{2-16}$$

The radiation stress equation contains terms for both momentum and pressure, with the momentum being related to wave height squared as in the following equation (Svendsen, 1984).

$$S_m = \frac{1}{16}\rho g H^2 \left(1+ \frac{2kh}{\sinh 2kh}\right) \tag{2-17}$$

Therefore, as the wave shoals, the increase in wave height increases the amount of momentum carried by the wave, and there is a larger force placed on the water column. Water tends to be dispelled from the region of wave shoaling and the mean water surface is lowered, creating a negative slope from offshore to the point of breaking. This is known as setdown. The momentum is dissipated during wave breaking and the radiation stress is lowered due to a decrease in wave height. This creates a force imbalance, and in order to restore the balance the mean water level experiences an inclination from the point of breaking to the shoreline. The time averaged elevation of the shoreline above the still water level due to this inclination is what was previously defined as wave setup. The extra weight of the water due to the setup counteracts the force of the increased radiation stress in the region before wave breaking. The theoretical expression given by Longuet-Higgins and Stewart (1962) for setdown, derived for varying water depth and steady wave trains, is as follows, where $a = H/2$ is the wave amplitude, H is the wave height, $k = 2\pi / L$ is the wave number, L is the wavelength, and

h is the water depth.

$$\bar{\eta} = -\frac{1}{2}\frac{a^2 k}{\sinh(2kh)} \tag{2-18}$$

This expression predicts a small slope in the setdown up to the region of rapid shoaling and wave breaking, where a steep setdown slope is predicted.

An early data set from an experiment by Saville (1961) qualitatively verified the theoretical expression of setdown (Longuet-Higgins and Stewart, 1962). However, the purpose of this experiment did not involve investigating setdown and setup, and therefore the data are not good for verifying how well the theoretical expression predicts setdown and setup. Bowen et al. (1968) performed a laboratory experiment to test the setdown. Measurements of the water surface were made from well outside the break point up to the beach. These measurements showed that the setdown expression from Longuet-Higgins and Stewart (1962) accurately predicted setdown away from the break point, but close to and at the point of breaking the measured setdown was not as severe as predicted. Bowen et al. (1968) attributed this to the difference in the observed wave height and the wave height predicted by linear wave theory. Observations were also made of the setup during the experiment, as Longuet-Higgins and Stewart (1962) had predicted that the slope of the setup would be proportional to the beach slope. The experiments by Bowen et al. (1968) found this to be true, but also noticed that there is an exponential rise in the water surface very close to the shoreline. This was confirmed in experiments by Van Dorn (1976). The experimental setdown and setup found by Bowen et al. (1968) can be seen in Figure 2-6.

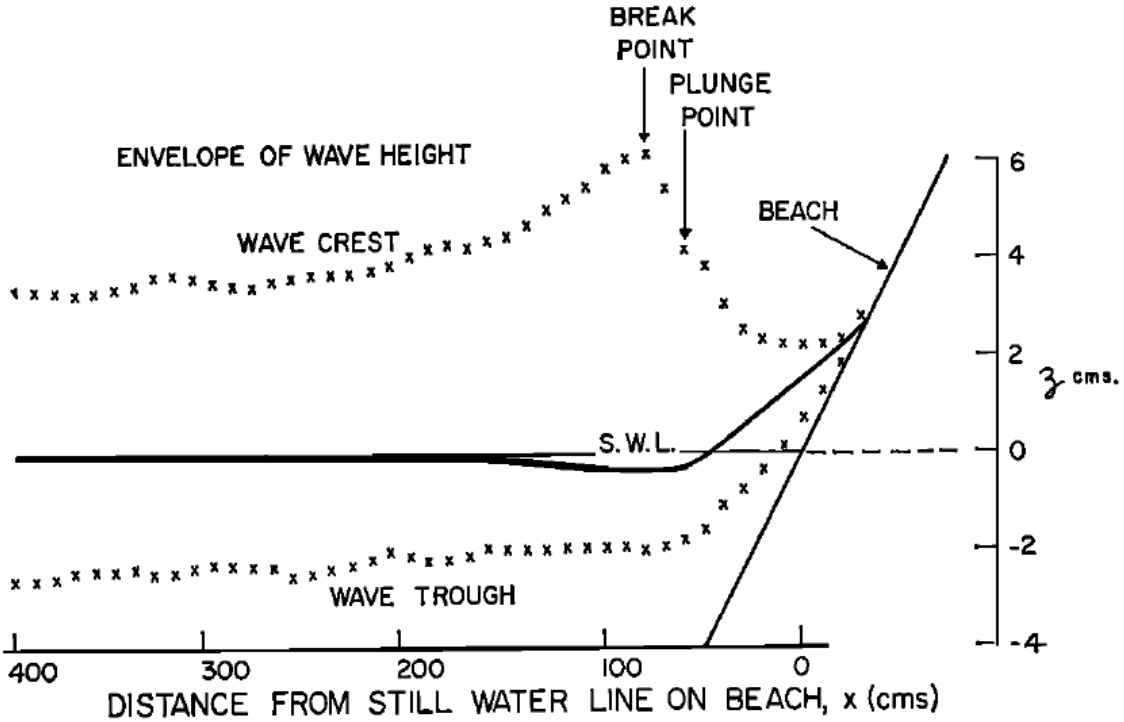

Figure 2-6 Setdown and Setup. Bowen et al. (1968) performed a laboratory experiment that showed how well actual measurements of setdown and setup compared to the theoretical predictions of setdown and setup (From Bowen et al., 1968).

The following theoretical expression for the maximum setup at the shoreline was given by Battjes (1974), where γH_b is a constant proportion of the breaking wave height.

$$\overline{\eta}_{max} = 0.3\gamma H_b \tag{2-19}$$

The first field experiment completed that verified the theoretical work done by Longuet-Higgins and Stewart (1962), Battjes (1974) and the laboratory work done by Bowen et al. (1968) on wave setup was done by Guza and Thornton (1981). Wave setup was measured on a gently sloping beach absent of any offshore bar structure. The experiment confirmed the existence of setup in the nearshore, and also confirmed the

exponential slope of the water surface very near the shoreline. It was also found that the maximum setup was independent of the local beach slope and was only dependent on the offshore significant wave height in deep water, which is similar to the theoretical result of Battjes (1974).

$$\bar{\eta}_{max} = 0.17 H_{s,\infty} \tag{2-20}$$

A field experiment by Holman and Sallenger (1985) countered the ideas of Battjes (1974) and Guza and Thornton (1981) that described setup as a function of wave height. It is argued that setup, when non-dimensionalized by significant wave height, is more proportional to a surf similarity parameter known as the Iribarren number (Equation 2-2), a form of the non-dimensional number that was first used in laboratory experiments by Hunt (1959).

2.5.5 Bound Long Wave

The concept of wave setup and setdown leads into a discussion on the bound long wave. As previously stated, waves arrive in the nearshore region in wave groups, consisting of waves with varying sizes, as shown in Figure 2-7. The larger waves carry more momentum, and thus have a larger radiation stress associated with them than smaller waves. The gradients in radiation stress between the large and small waves create a fluctuation in the water surface, in a similar way to wave setdown and setup due to breaking, as discussed previously (Longuet Higgins and Stewart, 1962). The water surface tends to be depressed under larger waves, and rises under smaller waves, as the additional water mass counteracts the increase in radiation stress under the larger waves. This is represented by the line representing the water surface level η in Figure 2-7. As

the wave groups propagate towards shore, the water surface fluctuations travel with the wave group. This fluctuation is known as a forced, or bound long wave (Longuet-Higgins and Stewart, 1962). As the wave group breaks, the bound long wave is released as a free long wave. This is thought to be one of the sources of infragravity energy in the surf zone (e.g. Holman 1981).

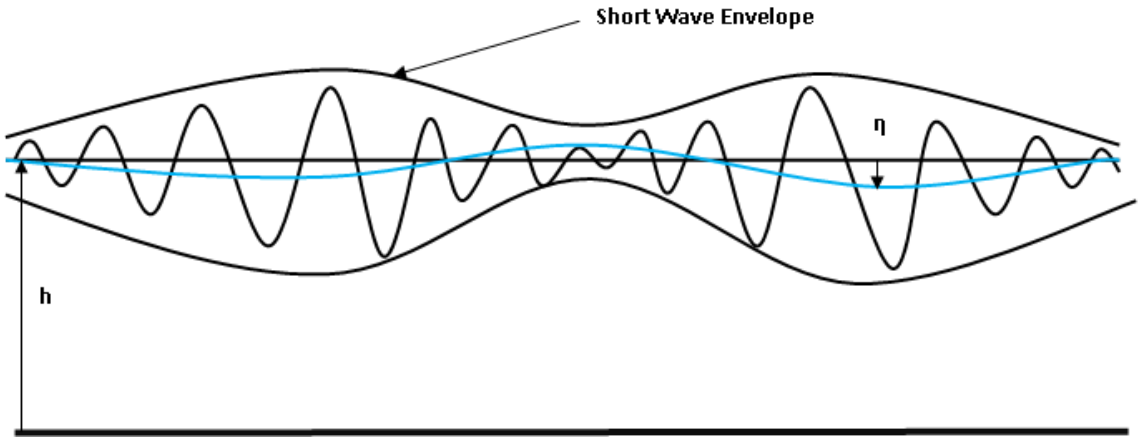

Figure 2-7 Bound Long Wave. The water surface is depressed under the higher waves in wave groups, and rises up under the smaller waves in the wave group. This creates a variation in the water surface known as a bound long wave. The water surface is represented in the figure by η.

2.5.6 Wave Runup and Swash

As previously mentioned, wave setup is only one component of the water level at the shoreline. Variations about the setup are defined as swash. Water level variations at the shoreline can be broken into incident band and infragravity band energy (e.g. Stockdon et al., 2006). Incident band energy generally refers to frequencies greater than 0.05 hz, while infragravity motions generally refer to frequencies from about 0.004 hz -

0.05 hz. Infragravity energy in the surf zone was first observed by Munk (1949), and has been shown to dominate surf zone processes during storm conditions (e.g. Holman, 1981; Raubenheimer and Guza, 1996). Incident wave energy in the surf zone has been shown to be saturated, as increasing wave heights do not result in a greater water level variations at the shoreline. It is important to note that the direct cause of the infragravity motions at the shoreline is not known. There are generally two lines of thought for the generation of the infragravity motions. The first is two dimensional in nature, and involves a forced progressive wave that is released after wave breaking and reflects off the shore, combining with the incoming progressive component to create a standing wave. Studies that support this theory include Munk (1949), Tucker (1950), and Suhayda (1974). The second theory is that infragravity motions are three dimensional edge waves. These waves propagate in the alongshore direction of the beach, and dissipate in the offshore direction (Huntley, 1976). Examples of studies that support this theory include Huntley (1976), Bowen and Guza (1978), Holman (1981), and Holman and Bowen (1984). Many of the differences are due to the differences in experimental locations, and different site bathymetries. Knowing the cause of infragravity motions is not necessary for the work done for this thesis, but is an important concept to understand when studying infragravity energy in the surf zone.

Studies involving shoreline water level oscillations typically refer to either swash or runup, which is directly related to swash as runup is equal to the swash variations plus the constant setup. This section will discuss studies of both runup and swash. Early descriptions of swash included Hunt (1959) who described the wave up-rush as a

function of offshore wave height, period and beach slope.

$$\frac{R}{H} = \frac{2.3 \tan\alpha}{\left(\frac{H}{T^2}\right)^{1/2}} \tag{2-21}$$

Miche (1951) described monochromatic waves as consisting of both progressive and standing components. The progressive component is dissipated in wave breaking, while the standing component is described as swash. Miche (1951) proposed that the amplitude of the swash with wave breaking would be the same as without wave breaking. Therefore, he suggested that swash is saturated, and the largest swash oscillations will occur at a wave height just large enough to break. A further increase in wave height will lead to energy dissipation and the swash amplitude does not increase. Battjes (1974) found an empirical relationship between swash amplitude, a_s, breaking wave height, H_b, and a surf similarity parameter that is a function of beach slope, β, breaking wave amplitude, a_b, and incident wave frequency, ω by measuring swash oscillations due to incident breaking waves.

$$2a_s = 0.4H_b\xi_b^2 \tag{2-22}$$

$$\xi_b^2 = \frac{\pi g\beta^2}{a_b\omega^2} \tag{2-23}$$

By substituting the second equation into the first, it is clear that there is no dependence on wave height.

$$\varepsilon_s = \frac{a_s\omega^2}{\pi g\beta^2} \tag{2-24}$$

These results suggest that swash oscillations become saturated, and do not increase with increasing incident wave height (Guza and Thornton, 1982). Guza and Thornton (1982) note however that energy associated with low frequency swash does increase with an increase in significant wave height. Their study of swash oscillations on a beach with a small slope determined that there was a linear relationship between swash amplitudes and incident wave height. The subscript s in the following equation stands for significant wave height and runup, while the v is for the vertical swash elevation. Guza and Thornton (1982) assumed that swash is a Gaussian process, and is narrow banded. The significant swash elevation was defined as 4σ, four times the standard deviation of the swash time-series. Note that in the following equation, R stands for swash instead of runup.

$$R_s^v = 3.48\ (\text{cm}) + 0.71\ H_s\ (\text{cm}) \qquad (2\text{-}25)$$

Holman and Sallenger (1985) collected field measurements of setup and swash on a steep beach with an offshore bar. It was found that the Iribarren number used by Hunt (1959) was important in predicting wave runup, with the foreshore slope used as the beach slope in the calculation of the Iribarren number in most conditions, with the exception of low tide when the offshore bar becomes important. It was also found that the incident frequencies of runup were only saturated for low Iribarren numbers; this was confirmed by Baldock et al. (1997). Also, infragravity frequencies were found to be unsaturated for all Iribarren numbers.

Holman (1986) extended the analysis of wave runup data by introducing extreme value statistics using the same data set as Holman and Sallenger (1985). Runup was

defined as the local maximum shoreline elevation between consecutive zero up-crossings. The four extreme value statistics he introduced are 1) - the 2% shoreline elevation, which is the shoreline elevation exceeded only by 2% of the data, 2) - the 2% runup, 3) - the 2% swash, and 4) - the maximum runup. It was determined that the data is less scattered when plotted in terms of swash values as opposed to runup values. This is due to the scatter in setup values. It was noted that during storm conditions, Iribarren numbers are usually low. Holman (1986) used this to introduce a storm Iribarren number.

$$\xi_{0\ \mathrm{storm}} = 6.3\ \beta \tag{2-26}$$

This was used to determine equations for all four extreme statistics that are functions of the beach slope and significant wave height; for example the 2% runup could be calculated as follows.

$$R_2 = (5.2\ \beta + 0.2)H_s \tag{2-27}$$

Ruggiero et al. (2004) again found that for dissipative beaches with low Iribarren numbers, runup was dominated by the infragravity band, with an average of 96% of the total variance occurring in the infragravity band. It was also found that significant wave runup elevation is dependent on the local foreshore beach slope. An experiment by Stockdon et al. (2006) resulted in an expression for the 2% runup for all natural beaches. This was significant as previous runup expressions applied to mostly dissipative, low slope beaches with low Iribarren numbers. The expression followed previous work, as R_2 was found to be dependent on deep water wave height, H_0, deep water wavelength, L_0, and the local beach slope, β_f.

$$R_2 = 1.1\left(0.35\beta_f(H_0L_0)^{1/2} + \frac{\left[H_0L_0\left(0.563\beta_f^2 + 0.004\right)\right]^{1/2}}{2}\right) \quad (2\text{-}28)$$

Stockdon et al. (2006) also determined that significant infragravity swash was best parameterized by wave height and wavelength, as follows.

$$S_{IG} = (H_0L_0)^{0.5} \quad (2\text{-}29)$$

The significant infragravity swash data from the Stockdon et al. (2006) study is shown below in Figure 2-8.

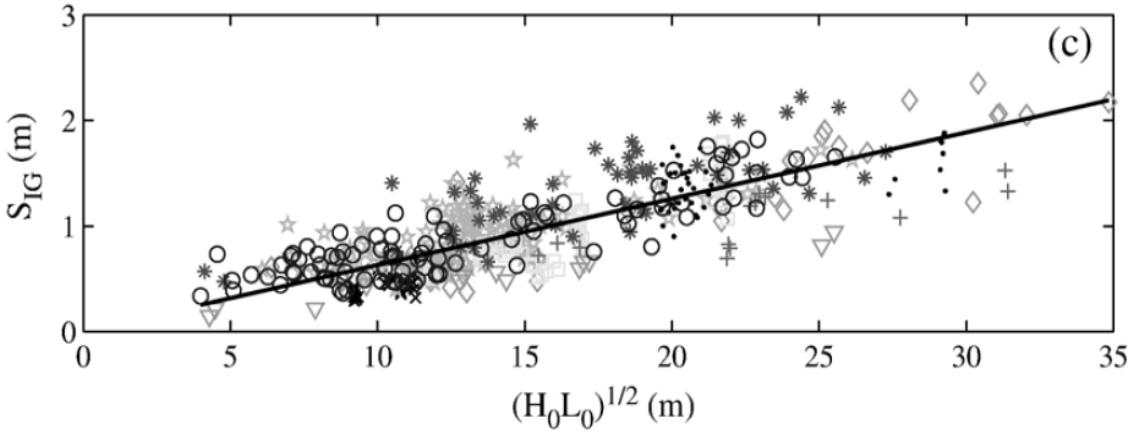

Figure 2-8 Stockdon et al. (2006) Parameterization of S_{IG}.

The parameterization includes data from a multitude of swash data for measurements from different locations, and does not differentiate between areas with different bathymetric features such as nearshore sandbars. The parameterization results in a correlation coefficient of 0.65, and a root mean square error of 25.7 cm.

Runup and swash processes are often assumed to be Gaussian, normally

distributed (e.g. Holland and Holman, 1993). For a Gaussian process, 95.4% of the values are accounted for within plus or minus 2 standard deviations from the mean, leaving 2.3% in each of the tails of the distribution. Therefore any value larger than 2 standard deviations greater than the mean has approximately a 2% chance of occurring. This leads to the definition of the 2% runup (Stockdon et al., 2006).

Many different ideas have been proposed about water level variations at the shoreline. Following is a brief summary to bring all of these ideas together. The water level at the shoreline is composed of two different components. These are setup and swash. Local maximum shoreline elevations between consecutive up-crossings about the setup are defined as runup, which is the combination of setup and swash at that point. For low Iribarren numbers, shoreline water level variations are dominated by infragravity energy, and incident energy is saturated. For higher Iribarren numbers, shoreline water level fluctuations are dominated by incident energy, which is not saturated. The exact source of the infragravity energy is unknown, but it may be due to either three dimensional edge waves, or two dimensional long waves in the cross-shore direction; this is most likely dependent on the bathymetry of the beach being studied. Various empirical formulations have been proposed for runup and swash on beaches. Nearly all use a combination of wave height, wave length, and/or beach slope.

2.5.7 Sediment Transport

Sediment transport is a highly dynamic and complex process which is even further complicated by surf zone processes. The existence of long waves has been shown to be an important factor in runup and swash motions at the shoreline, and these same

long wave motions are one of the most important mechanisms in sediment transport in the surf zone (Butt and Russell, 2000).

One of the main difficulties in modeling sediment transport is the lack of field data due to the challenge of accurately measuring sediment transport. This is further complicated by distinguishing between the bed load and suspended sediment load. Bed load has been defined as the sediment that is supported by forces from other sediment particles, while the suspended sediment is supported by the fluid (Bagnold, 1956). It has also been suggested that sediment transport in the surf zone should be modeled by sheet flow due to the high shear stresses (Hughes et al., 1997). In most coastal situations, sediment transport is driven by waves and current; the waves stir up the sediment, and the current acts as the transport mechanism (Soulsby, 1997).

The basic mass-balance equation for suspended sediment transport in a 2D flow is given by Gallappatti and Vreugdenhil (1985), where $\hat{c}$ is the sediment concentration, and ε is vertical turbulent diffusion.

$$\frac{\partial \hat{c}}{\partial t} + u\frac{\partial \hat{c}}{\partial x} + w\frac{\partial \hat{c}}{\partial z} = w_s\frac{\partial \hat{c}}{\partial z} + \frac{\partial}{\partial z}\left(\varepsilon\frac{\partial \hat{c}}{\partial z}\right) \tag{2-30}$$

An equation for calculating the total sediment transport, including bed load sediment and suspended sediment, is given by the Soulsby-Van Rijn equation (Soulsby, 1997), where C_D is the drag coefficient due to the current, A_s is the sum of coefficients for the bed load transport and the suspended sediment transport, $\overline{U}$ is the depth averaged velocity, and U_{rms} is the room mean square wave orbital velocity for stirring up sediment. The final term in the formula accounts for the bed slope, β, so the equation is applicable in areas with a sloping bottom.

$$q_t = A_s \overline{U} \left[\left(\overline{U^2} + \frac{0.018}{C_D} U_{rms}^2 \right)^{0.5} - \overline{U_{cr}} \right]^{2.4} (1 - 1.6 \tan \beta) \qquad (2\text{-}31)$$

2.5.8 Nearshore Processes Summary

The purpose of this thesis is to determine how nearshore sandbars affect beach vulnerability during storm events. This is accomplished by studying how the bathymetry affects infragravity energy in the surf zone. In order to do this, it is important to understand the many complicated processes that are simulated in a numerical model of the nearshore environment. This review of nearshore processes was intended to give a general understanding of how the numerical model XBeach simulates nearshore processes including infragravity energy and its effects on nearshore processes.

2.6 Modeling Nearshore Processes

Numerical modeling has proven to be an effective method for studying the nearshore processes that affect beaches during extreme storm conditions (e.g. Roelvink et al., 2009; McCall et al., 2010; Reniers et al., 2004). These robust nearshore models, which are capable of simulating processes such as flow velocities, sediment transport, infragravity motions, shoaling, refraction, wave dissipation, etc. are a result of earlier work on modeling individual nearshore processes such as dissipation (e.g. Roelvink, 1993). The implementation of early models came from an improved knowledge of nearshore processes, and a need to study these processes numerically. These models described wave properties that could be time averaged over the period of a wave, such as the wave height and the energy dissipation as waves break in the surf zone. Examples of

such models include Battjes and Janssen (1978), Svendsen (1984), and Dally et al. (1985). These models used the non-linear shallow water equations, and relied on assumptions of hydrostatic pressure. The models were depth integrated and yielded a uniform vertical distribution of horizontal velocity. Schaffer et al. (1993) points out that another result of using the non-linear shallow water equations is that they do not necessarily give a true description of the location of wave breaking in part due to the omission of frequency dispersion. In deep water wave speed is dependent on wavelength; therefore frequency dispersion is necessary to describe wave speed for waves of changing wavelength, such as shoaling waves. However in shallow water, the wave speed is only dependent on water depth, so the relationship between wavelength and wave speed provided by frequency dispersion is not necessary. This means that by not including frequency dispersion, the non-linear shallow water equations are only useful in very shallow water where wavelengths can be assumed long, and the wave speed is only dependent on water depth.

The use of Boussinesq equations by Schaffer et al. (1993) allowed for the inclusion of frequency dispersion. This allowed for the propagation of waves from deep water into the nearshore region. Frequency dispersion also provides the advantage of balancing the non-linear effect of amplitude dispersion, which is a non-linear effect that changing wave amplitude has on wave speed. This is a problem that had been pointed out by Dally et al. (1985), as this criterion works well for steep beach slopes only. Schaffer et al. (1993) applied the concept of a surface roller, as discussed by Svendsen (1984) as a volume of water that is carried by a wave that reaches a certain slope and

begins to break. The effect of the surface roller is to increase the energy flux and radiation stress. This concept was also used by Deigaard (1989), who expressed the roller as a pressure term in the depth averaged momentum equation. The results of the numerical model of Schaffer et al. (1993) showed good skill in simulating the evolution of wave heights through the surf zone; modeled wave heights compared well with measurements from physical experiments for both regular and irregular waves.

A numerical study by Reniers et al. (2004) on a barred beach combined the advances in modeling capabilities of both wave propagation and wave breaking, as well as advances in sediment transport modeling. The study focused on simulating wave group propagation in order to predict changes in bathymetry due to infragravity waves. This model also showed good results, concluding that infragravity waves play a part in sediment transport. Also, it was found that directional spreading can have a large effect on the way a beach responds to the wave forcing. For this reason, the effects of directional spreading are removed from the simulations completed for this thesis by propagating all waves at a 90 degree angle to the shoreline.

A study by Roelvink et al. (2009) on the impacts of extreme storm events on the coastline, including the effect on beaches, dunes and barrier islands was completed in order to validate the results of the numerical model XBeach (eXtreme Beach behavior) (Roelvink et al., 2010). XBeach is the numerical model that is used for the work completed in this thesis. Important innovations include the capability to model wave groups traveling in multiple directions, as well as the inclusion of multiple wave dissipation models and the ability to simulate avalanching; the periodic slumping of

eroded sand faces (Roelvink et al., 2010). An important aspect of XBeach is its capability to accurately simulate swash oscillations at the shoreline. This is due to the innovative description of wave groups used in the model, including the variation of wave heights in time (surf beat), which leads to the production of infragravity waves that are associated with much of the energy that arrives at the shoreline in the form of swash (Tucker, 1950). Swash is important, as it is a dominant forcing mechanism during storm conditions (e.g. Ruggiero et al., 2001). A detailed description of the model as it relates to this thesis can be found in section 3.2.

The Roelvink et al. (2009) study was designed to test the capability of XBeach to simulate the four impact regimes described by Sallenger (2000). Different test cases for each of the four impact regimes were completed. The computational results were then compared with data collected from both lab and field studies. For the swash regime was tested against analytical results. The model accurately described the swash oscillations produced by infragravity energy and also accurately reproduce analytical solutions for long-wave runup. Wave flume experiments and field tests were completed to test the model for the collision and overwash regimes. The volume of eroded sediment from the dune, along with the change in dune position showed good correlation between the model and test case, showing the models capability to simulate the collision regime. Again, good qualitative and quantitative results were obtained for the overwash regime. Finally, the models hydrodynamics were tested against a field experiment during storm conditions. Based on the results of this study, the model XBeach showed good skill in simulating the nearshore environment. In particular, XBeach shows skill in simulating

infragravity waves, and their effect on nearshore processes. (Roelvink et al., 2009)

Numerical modeling has been shown to be an effective way of studying the nearshore processes that affect beaches during extreme storm conditions. Specifically, the numerical model XBeach has been shown to effectively simulate storm impacts on beaches, dunes and barrier islands. This is due to its ability to accurately describe infragravity energy, which dominates during storm conditions. Therefore, XBeach can effectively be used to study how nearshore bathymetric features such as nearshore sandbars affect infragravity energy in the surf zone.

2.7 Literature Review Summary

In order to study how local bathymetric features such as nearshore sandbars affect the vulnerability of beaches during storm conditions through the use of a numerical model, many different processes must be studied and understood. This literature review has briefly examined the processes involved in studying beach vulnerability. The nearshore bathymetry was studied to accurately create a model grid. Generation of wind waves was important to examine for model forcing. Nearshore processes were reviewed in order to understand the complicated physics that the model simulates. Finally, the current knowledge of wave runup and swash was reviewed in order to determine the best way to analyze the effects of the bathymetry on beach vulnerability. It has been shown that infragravity energy is dominant during storm conditions, which are described by small Iribarren numbers. Infragravity energy can be measured in water levels offshore as well as in runup and swash variations at the

shoreline. Offshore infragravity energy can be compared to infragravity energy at the shoreline to determine how the local bathymetry affects the infragravity energy, which can be used as an indicator of how the bathymetry affects the vulnerability of beaches during storm conditions.

3 METHODS

3.1 Introduction

This section provides a detailed description of the numerical model used for this thesis, along with the creation of the various input files necessary to run the model, and the general methods used to complete the research done for this research. The equations used by the numerical model XBeach (eXtreme Beach behavior) (Roelvink et al., 2009) are described in section 3.2. A location with numerous nearshore sandbars was investigated, as detailed in section 3.3, and data from the site was used to determine several cross-shore bathymetric scenarios involving nearshore sandbars and bar-rips. The methods used to create profiles for the grids are described in section 3.4. All inputs necessary to use the numerical model XBeach for hydrodynamic and morphological simulations are discussed in section 3.5. Section 3.6 gives a brief description of the supercomputer used to run the XBeach simulations. Finally, section 3.7 details the analysis completed for the data output from each XBeach simulation.

3.2 XBeach

The numerical model XBeach is a robust model which solves coupled equations for nearshore hydrodynamics and morphodynamics. It is used to simulate nearshore processes and the response of the coastline during extreme storms with time-varying environmental conditions such as surge and waves (Roelvink et al., 2010). XBeach is designed to effectively simulate the four impact regimes described by Sallenger (2000), which were discussed earlier in this thesis. This includes simulating beach erosion, dune

erosion, overwash, and dune breaching.

The coordinate system employed in XBeach is shown in Figure 3-1. The grid must be specified as rectilinear (Roelvink et al., 2010).

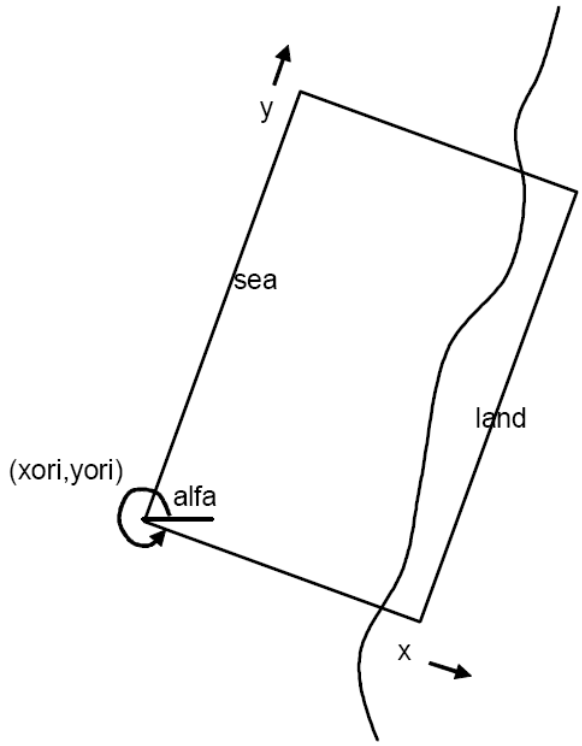

Figure 3-1 XBeach Coordinate System. The coordinate system used by XBeach orients the x-axis in the cross-shore direction, perpendicular to the shoreline, and the y-axis in the alongshore direction, parallel to the shoreline. The grid can be oriented at an angle alfa (From Roelvink et al. 2009).

XBeach uses a staggered grid, where values are defined at both cell center and cell edges, as shown below in Figure 3-2. Water levels, bed levels and concentrations are defined in the center of the cell, while velocities and sediment transport values are defined at the edge of cells (Roelvink et al., 2010).

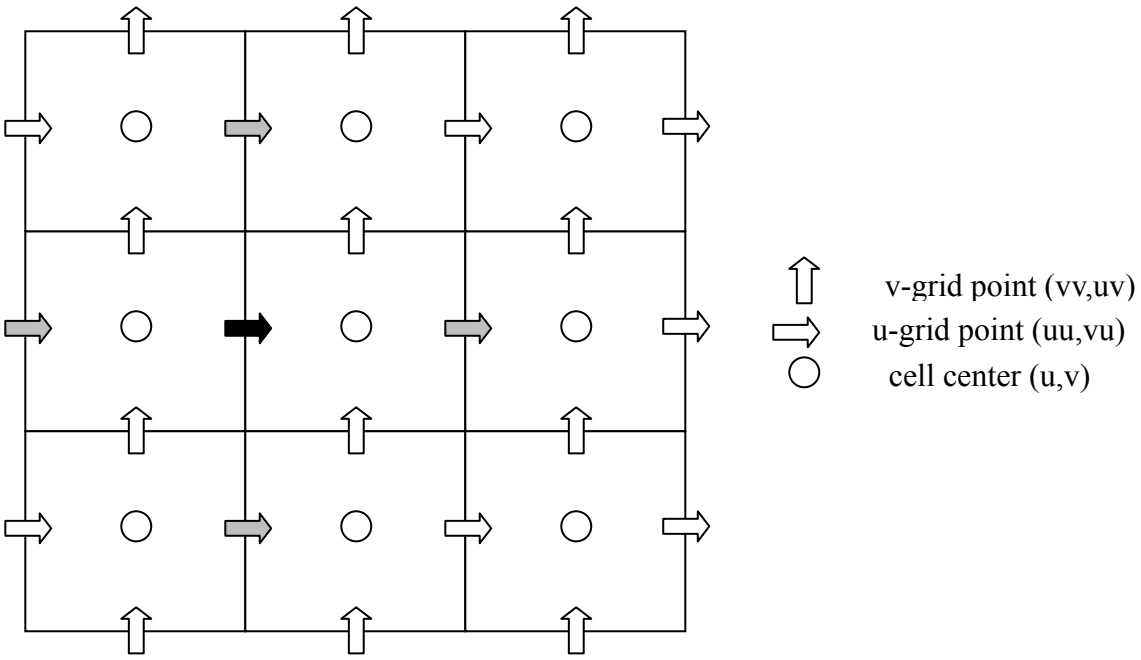

Figure 3-2 XBeach Grid. XBeach uses a staggered grid, with water levels, bed levels and concentrations defined in the center of each cell, while velocities and sediment transport rates are defined at the edge of each cell (Modified from Roelvink et al., 2010).

XBeach solves the non-linear shallow water equations for water velocities. The form of the non-linear shallow water equations used by XBeach are as follows, where τ_{bx} and τ_{by} are the bed shear stresses, η is the water surface level, F_x and F_y are stresses due to the waves, ν_h is the horizontal viscosity, and f is the Coriolis force (Roelvink et al., 2010).

$$\frac{\partial u^L}{\partial t}+u^L\frac{\partial u^L}{\partial x}+v^L\frac{\partial u^L}{\partial y}-fv^L-\nu_h\left(\frac{\partial^2 u^L}{\partial x^2}+\frac{\partial^2 u^L}{\partial y^2}\right)=\frac{\tau_{sx}}{\rho h}-\frac{\tau_{bx}^E}{\rho h}-g\frac{\partial \eta}{\partial x}+\frac{F_x}{\rho h} \qquad (3\text{-}1)$$

$$\frac{\partial v^L}{\partial t}+u^L\frac{\partial v^L}{\partial x}+v^L\frac{\partial v^L}{\partial y}-fu^L-v_h\left(\frac{\partial^2 v^L}{\partial x^2}+\frac{\partial^2 v^L}{\partial y^2}\right)=\frac{\tau_{sy}}{\rho h}-\frac{\tau_{by}^E}{\rho h}-g\frac{\partial \eta}{\partial y}+\frac{F_y}{\rho h} \tag{3-2}$$

$$\frac{\partial \eta}{\partial t}+\frac{\partial hu^L}{\partial x}+\frac{\partial hv^L}{\partial y}=0 \tag{3-3}$$

In order to calculate the wave forcing input to the non-linear shallow water equations, the wave action balance is solved. The wave action balance is time dependent and accounts for directional distribution of waves. The wave action balance accounts for frequency dispersion, which allows for a better prediction of the point of wave breaking, as described by Schaffer (1993). It is important to note that the wave action balance describes wave energy variations on the wave group timescale, as XBeach solves for wave group propagation. The wave action balance equation is shown below,

$$\frac{\partial A}{\partial t}+\frac{\partial c_x A}{\partial x}+\frac{\partial c_y A}{\partial y}+\frac{\partial c_\theta A}{\partial \theta}=-\frac{D_w}{\sigma} \tag{3-4}$$

where A represents the wave action, θ represents the angle of incidence with respect to the x-axis,

$$A(x,y,t,\theta)=\frac{S_w(x,y,t,\theta)}{\sigma(x,y,t)} \tag{3-5}$$

and σ is the intrinsic frequency as calculated from the linear dispersion relationship (Roelvink et al., 2010).

$$\sigma^2=gk\tanh kh \tag{3-6}$$

The wave number, k, is calculated as follows (Roelvink et al., 2010),

$$\frac{\partial k_y}{\partial t} + \frac{\partial \omega}{\partial y} = 0 \tag{3-7}$$

$$\frac{\partial k_x}{\partial t} + \frac{\partial \omega}{\partial x} = 0 \tag{3-8}$$

$$k = \sqrt{k_x^2 + k_y^2} \tag{3-9}$$

where ω is the absolute radial frequency.

$$\omega = \sigma + k_x u^L + k_y v^L \tag{3-10}$$

Wave energy dissipation is accounted for in the wave action balance. The total wave energy dissipation, integrated over all directions, is calculated according to the Roelvink dissipation model (Roelvink, 1993), where T_{rep} is a representative wave period, α is a factor of the order one, ρ is the water density, and γ is the breaker index (Roelvink, et al. 2010).

$$\overline{D_w} = 2\frac{\alpha}{T_{rep}} Q_b E_w \tag{3-11}$$

$$Q_b = 1\text{-}\exp\left(-\left(\frac{H_{rms}}{H_{max}}\right)^n\right) \tag{3-12}$$

Finally, to close the wave action balance, XBeach employs wave dissipation due to bed friction as follows (Roelvink et al., 2010).

$$D_f = \frac{2}{3}\rho\pi f_w \left(\frac{\pi H}{T_{rep} \sinh kh}\right)^3 \tag{3-13}$$

The wave action balance determines the spatial distribution of wave energy, which in turn yields radiation stresses from linear wave theory (Roelvink et al., 2010). The radiation stress equations are shown below.

$$S_{xx,\,w}(x,y,t) = \int \left(\frac{c_g}{c}(1+\cos^2\theta)-\frac{1}{2}\right) S_w \, d\theta \tag{3-14}$$

$$S_{xy,\,w}(x,y,t) = S_{yx,\,w}(x,y,t) = \int \sin\theta \cos\theta \left(\frac{c_g}{c} S_w\right) d\theta \tag{3-15}$$

$$S_{yy,\,w}(x,y,t) = \int \left(\frac{c_g}{c}\left(1+\sin^2\theta\right)-\frac{1}{2}\right) S_w \, d\theta \tag{3-16}$$

The wave energy dissipation term, D_w, from the wave action balance is used as input to the roller energy balance, which is coupled to the wave action balance. The roller energy describes the energy that is stored in the surface rollers. By accounting for the additional momentum that is stored in the rollers, the radiation stress is increased, and there is a shoreward shift in the location of maximum setdown. The roller energy balance does not account for the full range of frequencies, but instead uses the value of the mean frequency to represent all frequencies. The roller energy balance is as follows, where $S_r(x,y,t,\theta)$ represents the roller energy (Roelvink et al. 2009).

$$\frac{\partial S_r}{\partial t}+\frac{\partial c_x S_r}{\partial x}+\frac{\partial c_y S_r}{\partial y}+\frac{\partial c_\theta S_r}{\partial \theta} = -D_r+D_w \tag{3-17}$$

The wave celerity is calculated as follows, where the celerity, c, is calculated with linear theory (Roelvink et al., 2010).

$$c_x(x,y,t,\theta) = c\cos\theta + u^L \tag{3-18}$$

$$c_y(x,y,t,\theta) = c\sin\theta + v^L \tag{3-19}$$

The total roller energy dissipation is calculated using the method of Reniers et al. (2004).

$$\overline{D_r} = \frac{2g\beta_r E_r}{c} \tag{3-20}$$

In order to close the set of equations for the roller energy balance, the total roller dissipation is directionally distributed over all wave directions proportionally (Roelvink et al., 2010).

The roller contributes an additional radiation stress to the system. This is described by XBeach as follows (Roelvink et al., 2010).

$$S_{xx,\,r}(x,y,t) = \int \cos^2\theta\, S_r\, d\theta \tag{3-21}$$

$$S_{xy,\,r}(x,y,t) = S_{yx,\,r}(x,y,t) = \int \sin\theta\cos\theta\, S_r\, d\theta \tag{3-22}$$

$$S_{yy,\,r}(x,y,t) = \int \sin^2\theta\, S_r\, d\theta \tag{3-23}$$

The radiation stress contributions from the wave and from the roller can then be used to calculate the wave forcing to the non-linear shallow water equations (Roelvink et al., 2010).

$$F_x(x,y,t) = -\left(\frac{\partial S_{xx,w}+\partial S_{xx,r}}{\partial x}+\frac{\partial S_{xy,w}+S_{xy,r}}{\partial y}\right) \tag{3-24}$$

$$F_y(x,y,t) = -\left(\frac{\partial S_{xy,w}+\partial S_{xy,r}}{\partial x}+\frac{\partial S_{yy,w}+S_{yy,r}}{\partial y}\right) \tag{3-25}$$

For simulations completed with morphological updating, XBeach simulates sediment transport with a depth-averaged advection-diffusion equation from Galappatti and Vreugdenhil (1985),

$$\frac{\partial hC}{\partial t}+\frac{\partial hCu^E}{\partial x}+\frac{\partial hCv^E}{\partial y}+\frac{\partial}{\partial x}\left[D_s h\frac{\partial C}{\partial x}\right]+\frac{\partial}{\partial y}\left[D_s h\frac{\partial C}{\partial y}\right] = \frac{hC_{eq}-hC}{T_s} \tag{3-26}$$

$$T_s = \max\left(0.05\frac{h}{w_s},0.2\right)s \tag{3-27}$$

where C is the depth-averaged sediment concentration, C_{eq} is the equilibrium sediment concentration, D_s is the sediment diffusion coefficient, and T_s is an adaption time that represents sediment entrainment (Roelvink et al., 2010). Sediment deposition or entrainment is governed by the difference between the actual sediment concentration and the equilibrium sediment concentration. After each time step, XBeach accounts for the sediment transport, and the bed level is updated. The sediment concentration C varies on the wave group time scale (Roelvink et al., 2010).

The sediment transport formulation of Soulsby-van Rijn (Soulsby, 1997) is used to calculate the equilibrium sediment concentration,

$$C_{eq} = \frac{A_{sb}+A_{ss}}{h}\left(\left(|u^E|^2+0.018\frac{u_{rms}^2}{C_d}\right)^{0.5} - u_{cr}\right)^{2.4}(1-\alpha_b m) \tag{3-28}$$

where the short wave orbital velocity near the bed, u_{rms}, is used along with the Eulerian mean and infragravity velocity to force sediment stirring (Roelvink et al., 2010).

$$u_{rms} = \frac{\pi H_{rms}}{T_{rep}\sqrt{2}\sinh(kh)} \tag{3-29}$$

C_d is a drag coefficient that is based only on the flow velocity, and α_b is a calibration factor for the bed slope, m. Finally, A_{sb} and A_{ss} represent the bed load and suspended bed load coefficients, respectively, and are a function of sediment grain size, relative density of the sediment, and the local water depth (Roelvink et al,. 2010).

To close the set of sediment transport equations, the sediment concentration C is used to calculate the sediment transport rates (McCall, 2010).

$$S_x = hCu^E - D_s h\frac{\partial C}{\partial x} \tag{3-30}$$

$$S_y = hCv^E - D_s h\frac{\partial C}{\partial y} \tag{3-31}$$

3.3 Development of Sandbar Scenarios

Nearshore sandbars occur in many different areas of the United States, however with its generally small to moderate wave climate and small tidal range the northern Gulf of Mexico is a prime location for sandbar formation (Wright et al., 1986). Also, the Gulf of Mexico experiences a large amount of hurricane activity. Several large, highly

destructive hurricanes in the past several years include Hurricane Katrina, which devastated the Gulf Coast in and around New Orleans, and Hurricane Ike, which directly impacted the city of Houston. Due to this tendency to develop large scale nearshore sandbars, and the high frequency of hurricane activity, nearshore bathymetric data from the area around Panama City Beach, FL was investigated. The three bathymetric scenarios that are studied in this thesis include no-bar, continuous alongshore bar, and bar-rip. All three scenarios were found to occur in the nearshore bathymetry of the Panama City Beach, FL area. Using the bathymetric data, the typical alongshore and cross-shore spatial distributions and scales of these bathymetric scenarios was studied.

In order to accurately describe the nearshore bathymetry for numerical modeling with XBeach, it is important to have accurate, high resolution bathymetric surveys from areas where the complex bathymetric features that are studied in this thesis occur. The United States Army Corps of Engineers Joint Airborne Lidar Bathymetry Technical Center of Expertise (JALBTCX) routinely collects LiDAR data for the Panama City Beach, FL area. The set of LiDAR data used was collected in 2010. The spatial extents of the data analyzed are approximately 24 kilometers to the northwest of Panama City Beach, and approximately 14 kilometers to the southeast of Panama City Beach. This is shown in Figure 3-3, along with an example of the LiDAR data in Figure 3-4. The offshore extent of the LiDAR data is approximately 1 kilometer from the shoreline.

Figure 3-3 Location of LiDAR Data. The LiDAR data used for this research ranged from about 24 km to the northwest of Panama City Beach to about 14 km to the southeast of Panama City Beach.

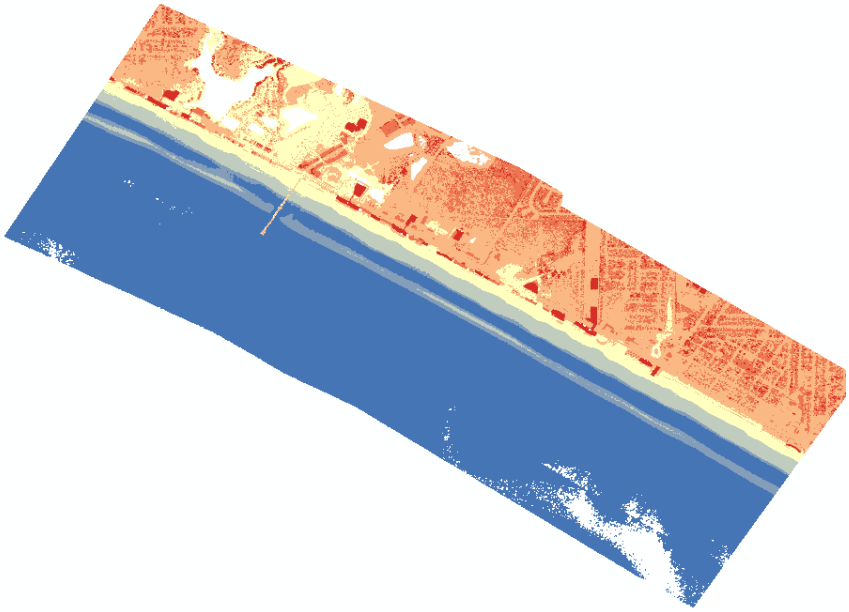

Figure 3-4 Example of Raw LiDAR data from Panama City Beach, FL.

The spatial resolution of LiDAR data allows for investigating the size and spatial distribution of nearshore sandbars. In order to gather a basic understanding of how the distance from the shoreline to the sandbar and the depth of the sandbars varies in the alongshore direction, the LiDAR data was analyzed using the geographic information system software ArcGIS (ESRI). Profiles were taken at many different locations along the coastline to obtain an idea of the variability in the offshore distance to the sandbar from the shoreline, and the depth of the sandbar. It was found that the bar depth varies linearly with the offshore location of the sandbar. Generally, as the sandbar migrates further offshore, the depth to the crest of the bar decreases. Figure 3-5 graphically describes the variability in sandbar location and depth.

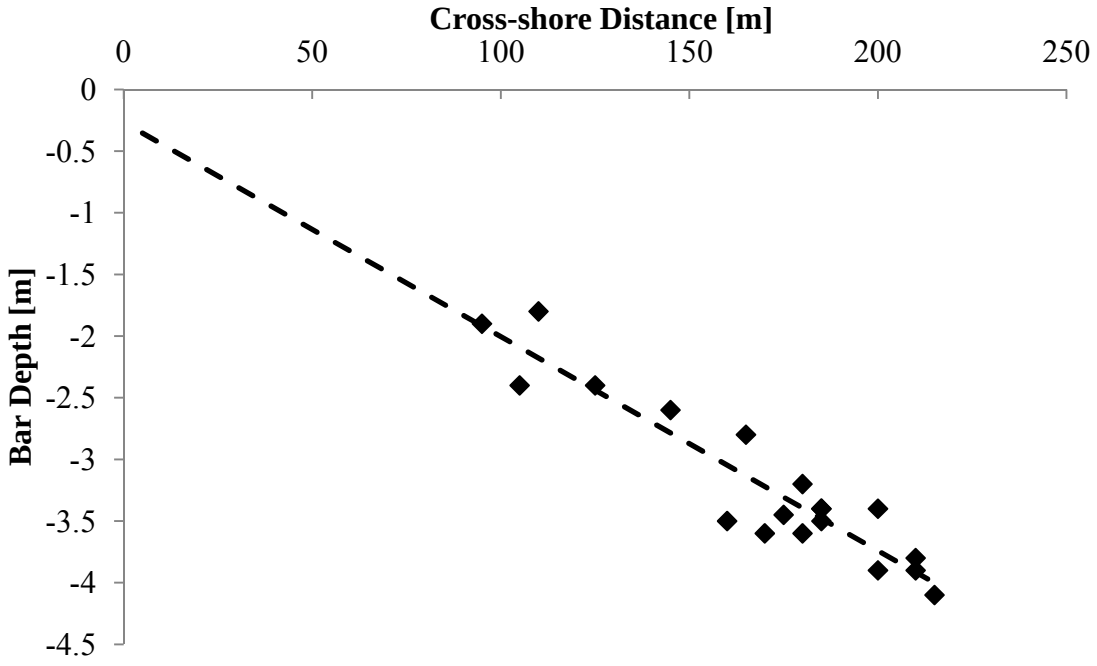

Figure 3-5 Bar Locations from LiDAR Data. This figure describes the correlation between bar depth and cross-shore distance. In general, as the bar moves offshore, the bar depth decreases.

Extracting multiple different profiles from the LiDAR data was necessary to ensure that the bathymetry used to develop the grid for the numerical model was representative of the true bathymetry in the Panama City Beach area. An example of a profile extracted from the LiDAR data is shown below in Figure 3-6.

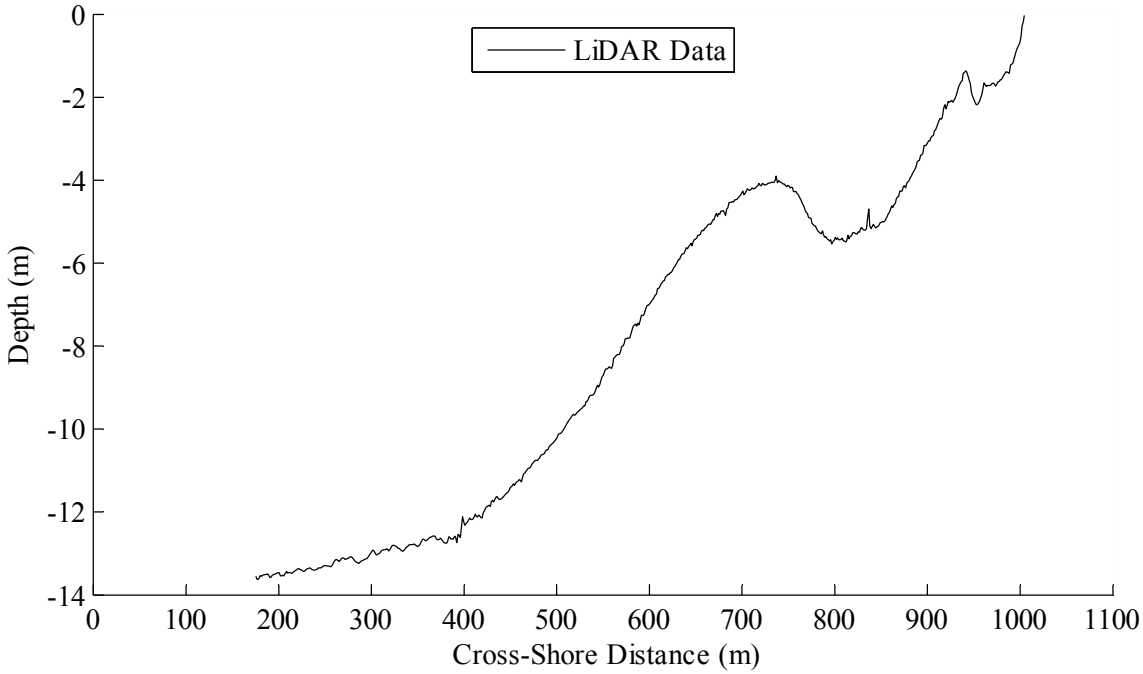

Figure 3-6 Raw Bathymetric Profile. An example raw profile extracted from the LiDAR data from the area around Panama City Beach, FL.

From this data, multiple idealized sandbar configurations were created to account for the full range of sandbar locations that were observed to occur in the Panama City Beach region.

Multiple idealized bar scenarios were created to cover the range of bar locations shown above in Figure 3-5. For each distance to the bar, two scenarios were created, one

representing the bar depth at mean sea level, and one representing the bar depth at an extreme low tide, about 0.6 m below the mean sea level. The shallower bar depth scenarios will have a greater effect on the waves, and an idea of the maximum effect that nearshore sandbars have on wave energy could be obtained. The bar locations for each scenario are shown below in Table 3-1.

Table 3-1 Bar Locations and Depths for Each Scenario

Scenario Number	Distance to Bar (m)	Bar Depth (m NAVD88)
1	50	1.20
2	75	1.60
3	100	2.00
4	125	2.40
5	150	2.75
6	200	3.50
7	50	0.60
8	75	1.00
9	100	1.40
10	125	1.80
11	150	2.15
12	200	2.90

3.4 Profile Fitting

The different scenarios created for this research involve specific bar locations and depths (see Table 3-1). In order to simplify the bathymetric data for use in a computational grid, a general bathymetric profile was extracted from the LiDAR data, and a piece-wise function was used to fit the profile. This function was then modified in order to create simplified bathymetric profiles for any bar location and depth. This section describes fitting the piece-wise function to a bathymetric profile and how this

was used to define multiple idealized profiles that were then used to describe the bathymetry for the grids.

3.4.1 Continuous Alongshore Bar Profile

The piece-wise function used to describe the nearshore bar profile consists of four parts. The first part describes the bathymetry from the shoreline to the bottom of the trough, which is the deepest point before the bar. The second and third parts describe the bar itself, and the fourth part describes the bathymetry after the bar in the offshore direction. The initial bathymetric profile from the LiDAR data, as well as the four parts of the profile that individual parts of the piece-wise function describe, is shown in Figure 3-7.

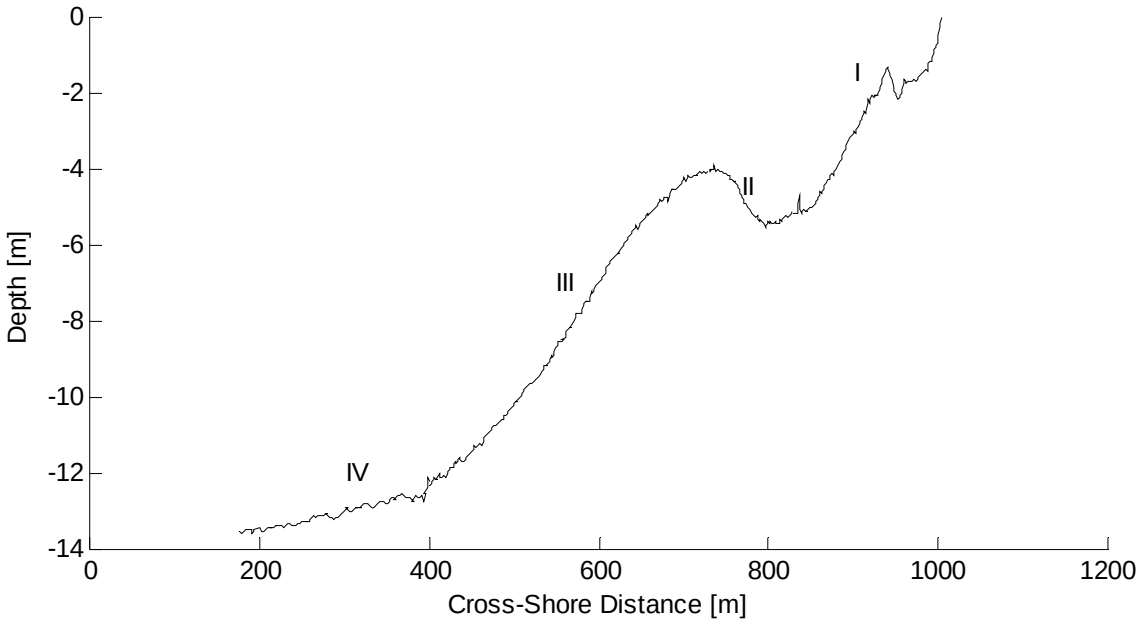

Figure 3-7 Division of Bar Profile. This figure illustrates how the bar profile was divided into the four distinct regions used for the piece-wise function. Region I is the initial equilibrium profile. Regions II and III are sine curves. Region IV is the second equilibrium profile with a virtual origin.

The equilibrium profile (Equation 2-1) was used to characterize the first part of

the piece-wise function. As can be seen above in Figure 3-7 there is a smaller sandbar in the first part of the profile. In order to simplify the profile, this sandbar was not considered, and is not described by the equilibrium profile. As discussed earlier, smoothing of bathymetric features is an important aspect of creating a computational grid for numerical modeling. Depending on the specific model being used, it may be important to smooth small-scale variations in the bathymetry to avoid numerical errors. XBeach does not react to small-scale bathymetric variations, therefore they are not included in the computational grids. The second and third parts of the piece-wise function are simple sine functions. For the second part, the phase of the sine function ranges from -0.5π to 0.5π. For the third part, the phase of the sine function ranges from 0.53π to 1.35π. The fourth part of the piece-wise function is again the equilibrium profile, however this time a virtual origin is used. The virtual origin is the origin that is necessary for an equilibrium profile to reach the depth where the fourth part of the piece-wise function will start. Figure 3-8 shows the original LiDAR data along with the four parts of the piece-wise function that is fit to the LiDAR data.

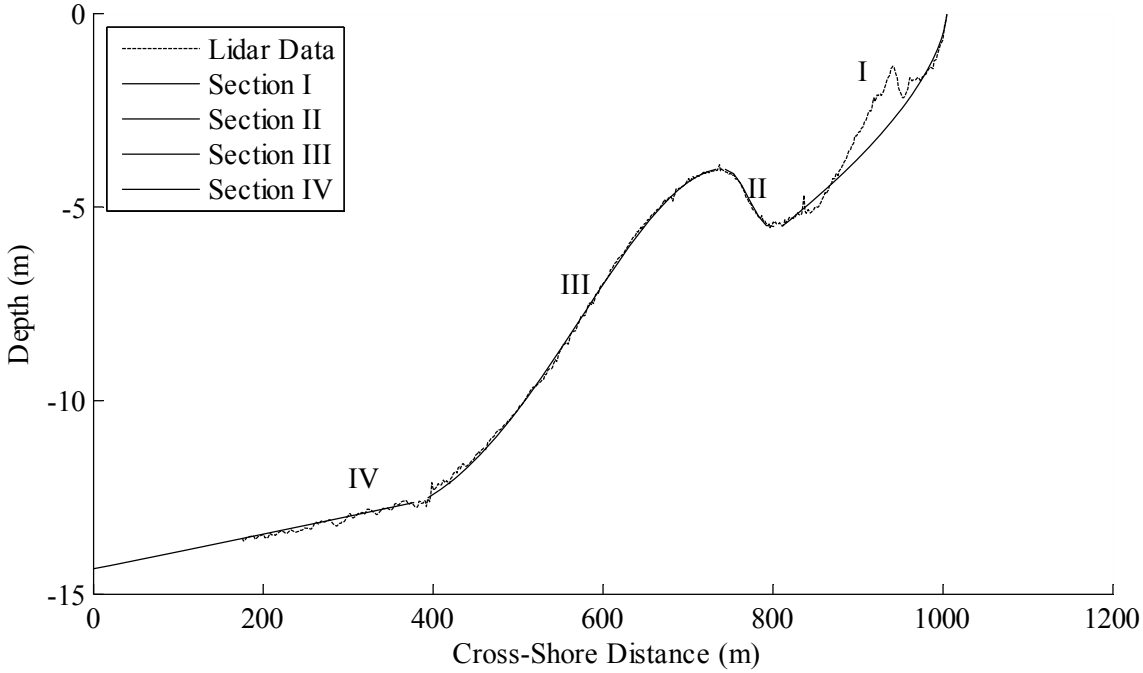

Figure 3-8 Piece-Wise Function Fit to Raw Data. Example of how the piece-wise function is fit to the raw LiDAR data. The piece-wise function effectively smoothes minor bathymetric variations while keeping the bar.

At this point, the general shape of the bar has been fit, and all of the small-scale features have been removed (by not including them in the fit). The next step is to create the idealized profiles, with the specific scenarios specified in Table 3-1 In order to do this, it was important to think about how the bar would be changed in the process. It is necessary not to change the general shape of the bar or the slopes of the equilibrium profiles. The slopes of the equilibrium profiles, as well as the bar shape will play an important role in the transformation of waves as they propagate toward the shoreline, so it is necessary to keep them the same for accurate comparisons between different profiles. For this reason, the A and m values for the equilibrium profiles and the phases of the sine functions were not changed when developing different profiles for each

scenario. The only variables that were adjusted were the distance to the bar, the depth of the bar, and the height of each sine curve. Figure 3-9 shows an example of an adjusted profile so that the bar is at a distance of 100 meters from the shoreline, and the depth of the bar is 2.0 meters.

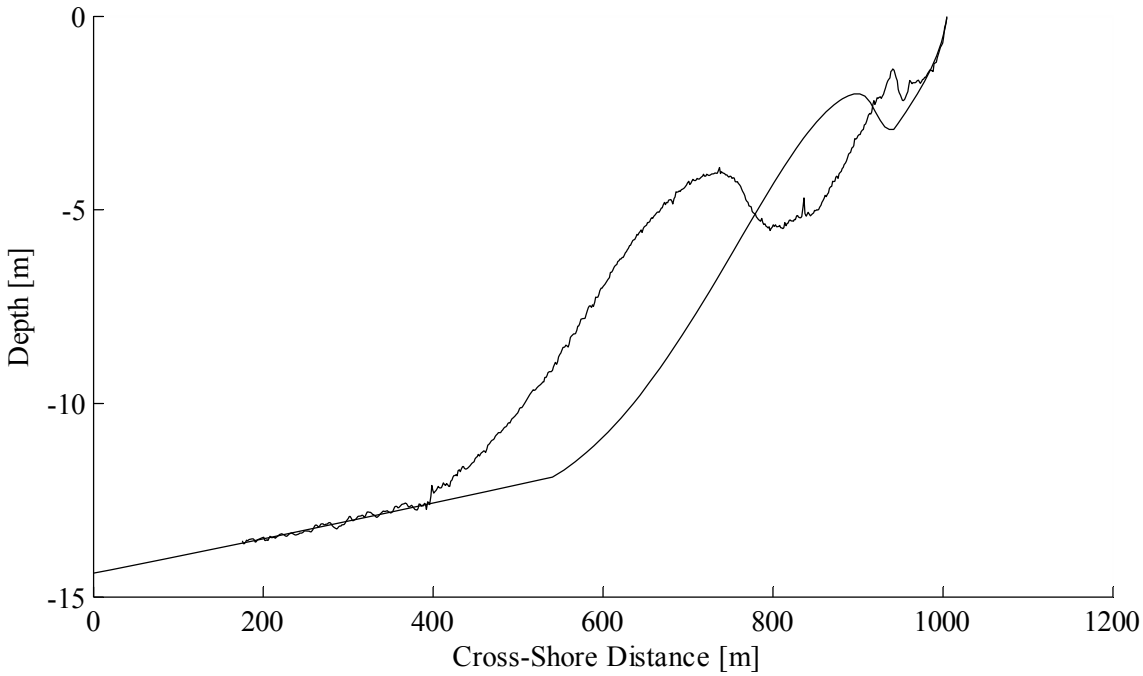

Figure 3-9 Example of a Modified Profile. This figure provides an example of how the bar is moved to a specific distance from the shoreline, and depth. The original raw LiDAR data is shown as the dotted line, while the new profile is the solid line.

It is important to note that the slope of the equilibrium profile leading up to the base of the bar and the slope of the equilibrium profile from the shoreline to the trough of the bar have not been changed. In general the shape of the bar has been kept as close to the original shape as possible. However, it should be noted that the size of the bar has

been changed; the cross-sectional area is smaller when pushed inshore, as can be seen in Figure 3-9 above. It is unclear how this will affect the results of the numerical simulation, but it was determined that keeping the general shape and slopes of the bar the same was more important than maintaining a uniform cross-sectional area of the bar. Figure 3-10 shows the six bathymetric profiles that were created for the mid-tide water level and also illustrates how the slope between the bar trough and the shoreline was kept constant, the similarity in the offshore slopes of the bars, and the change in the cross-sectional area of the bars. Also, the general trend of the bar depth to decrease with increasing offshore distance is shown.

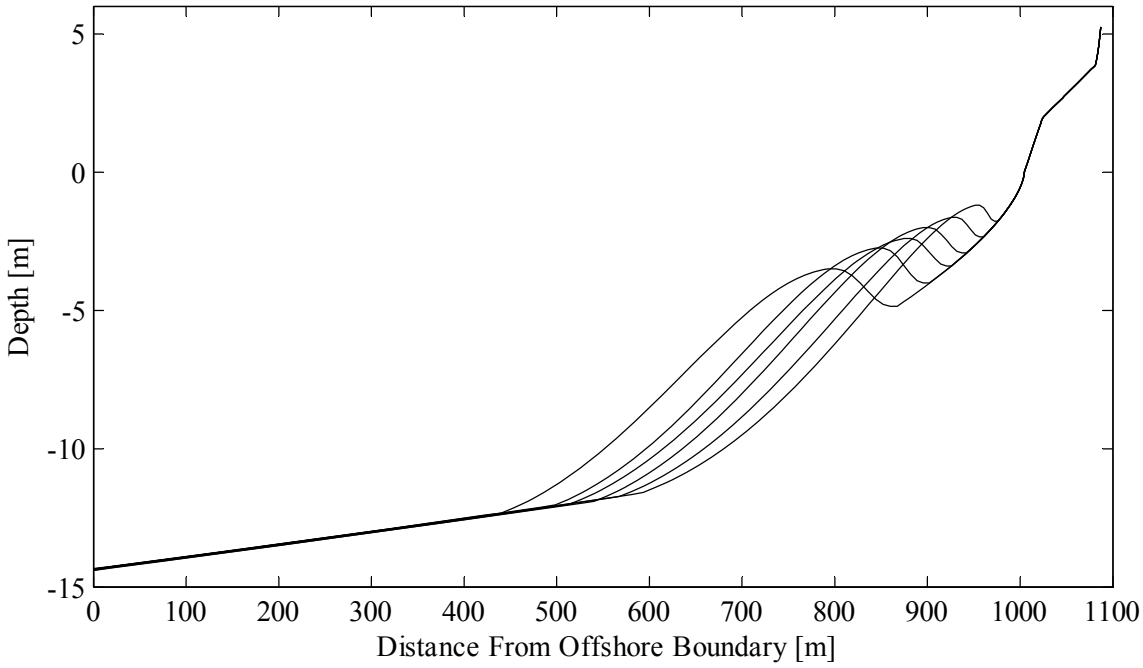

Figure 3-10 Comparison of Bar Bathymetries. This figure provides a comparison of the six different bar profiles created for the mid-tide simulations. Note how the slope of the equilibrium profiles remain the same between the different grids.

3.4.2 Bar-Rip Profile

The bar-rip scenarios consist of two separate profiles. The first is the bar profile. The bar profile for the bar-rip grid uses the same profile as the bar profile for the bar scenario. The second profile used in the bar-rip grid is the rip profile. This profile uses a piece-wise fit of three different functions, similar to the bar profile. The difference is that the two sine curves are removed, and replaced with a line from the bottom of the first equilibrium profile to the start of the second equilibrium profile. The rip profile is shown in Figure 3-11.

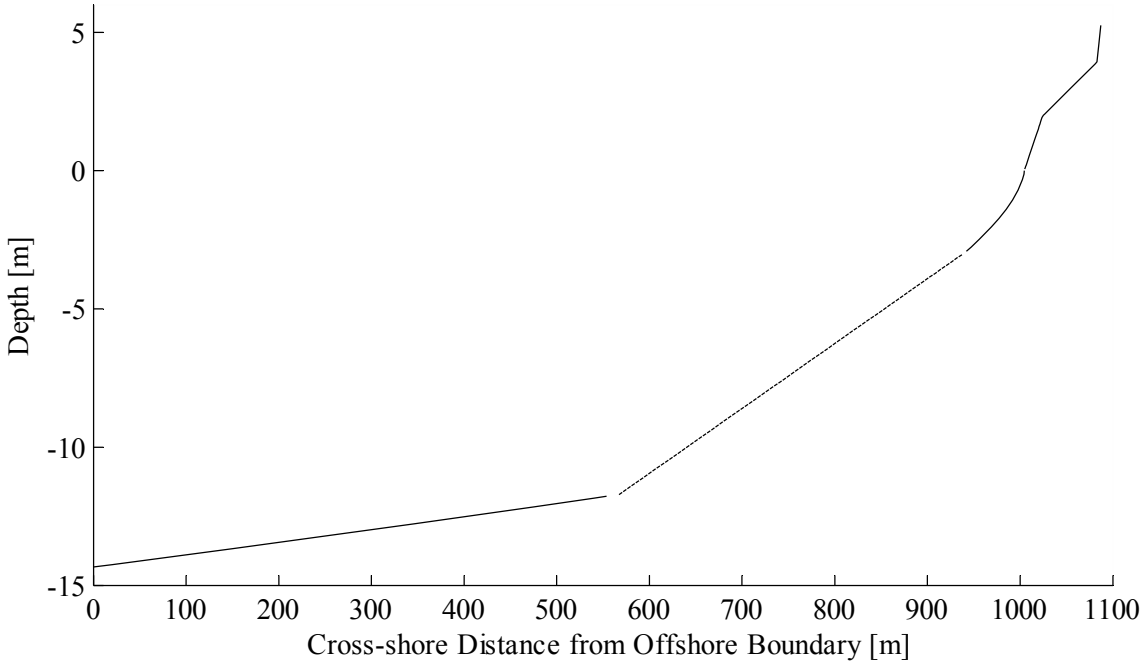

Figure 3-11 Rip Profile. The rip profile consists of three sections. The middle section is a line, and replaces the two sine curves from the bar profile.

3.4.3 No-Bar Profile

The no-bar profile is created as a control scenario to use for comparisons with the bar-rip and continuous alongshore bar scenarios. The no-bar profile consists of two parts. The first is the initial equilibrium profile, which extends from the shoreline to a depth that is past the end of the deepest bar. From that point, the second equilibrium profile that was used in the bar profile is again used to extend the no-bar profile out to the offshore boundary. The no-bar profile along with the raw LiDAR data used to create the profile is shown in Figure 3-12.

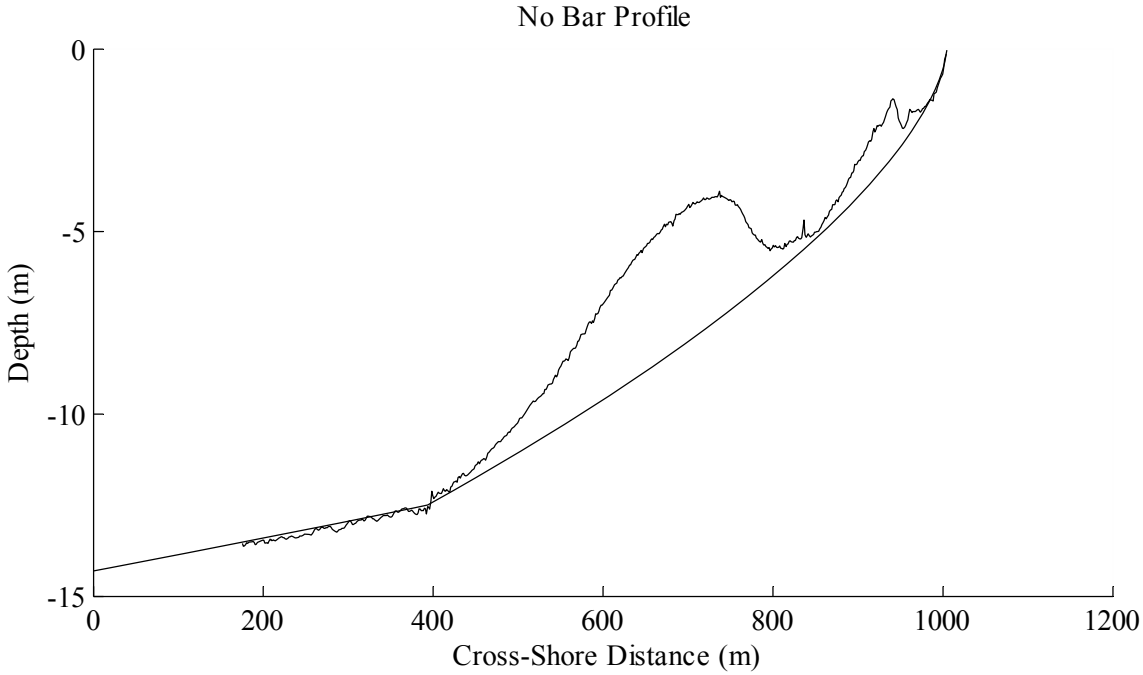

Figure 3-12 No-Bar Profile. The no-bar profile uses two equilibrium profiles. The first ends at the bottom of the bar, with the second continuing offshore from the bottom of the bar.

3.4.4 Beach Profile

Along with creating profiles for the three bathymetric scenarios, a profile was created for the beach topography. This profile is appended to each of the bathymetric profiles. LiDAR data from the Panama City Beach area was again used to determine appropriate beach slopes and dimensions. A beach profile was chosen that represented the general dimensions of the beaches in the Panama City Beach area. From this beach profile, a more general profile to be used in the cross-shore profiles was created. It was found that the beaches generally included three distinct regions; these are a beach face, berm, and dune. The beach face is defined in this thesis as the initial steep portion of the beach as it rises from the shoreline. The berm is then the flatter, longer section that extends from the end of the beach face to the dune. In order to simplify the beach profile used for the grids, these three regions are each represented by a line. The length of the beach face used for all scenarios is 20 m, and the berm length is 60 m. The berm length was extended past the actual beach profile extracted from the LiDAR data in order to ensure that the waves would not reach the dune during the numerical modeling. An example of a raw cross-shore beach profile from the LiDAR data, and the profile used to represent the beach can be seen in Figure 3-13. It is important to note that the beach profiles extracted from the LiDAR data are highly variable, and the beach profile chosen to create the idealized profile is representative of an average beach profile for the area.

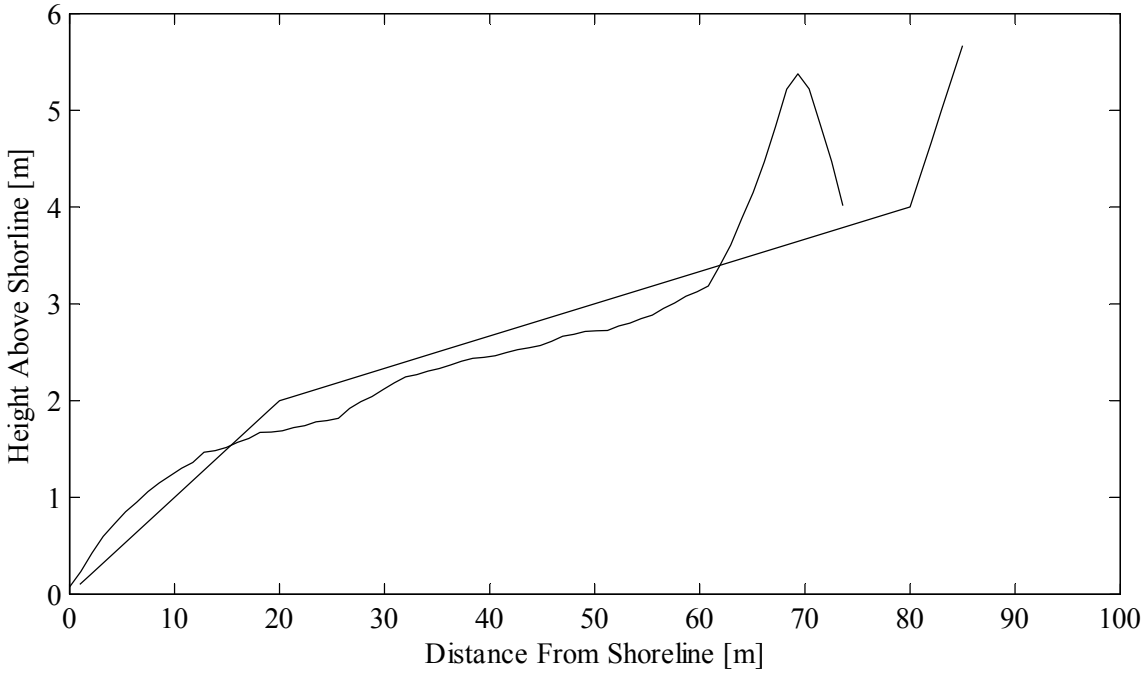

Figure 3-13 Beach Profile. The beach profile used consists of the beach face, berm, and sand dune. The berm has been extended to ensure that waves do not reach the sand dune during the simulations.

3.5 XBeach Setup

3.5.1 XBeach Grid Files

The bathymetry is defined in three files; the x grid file, the y grid file, and the depth file. The depth files for the no-bar and continuous alongshore bar scenarios were created by repeating the idealized profiles so that the bathymetry is constant in the alongshore direction. For the bar-rip grids, the rip bathymetry was repeated for the width of the rip in the center of the depth file, and the bar bathymetry was repeated on either side of the rip. Therefore the rip profile is constant in the alongshore direction for the length of the rip, and the bar profile is constant elsewhere in the alongshore direction. Between the rip and the bar profiles, the bathymetry was smoothed in the alongshore

direction so that there is not a steep drop between the bar and the rip.

XBeach allows for either a constant or variable spacing between grid cells. For this thesis, variable grid spacing was used in the x-direction, and constant grid spacing was used in the y-direction. For the x-direction, it was important to have a small enough grid spacing to accurately describe the wave propagation, but also to have a large enough spacing to save computational time. In order to accomplish this, the x-direction grid spacing starts at 20 m at the offshore boundary, and linearly decreases to a grid spacing of 0.5 m at the shoreline. Small grid spacing at the shoreline was necessary to accurately simulate the wave motions at the shoreline. The waves cause the location of the shoreline to fluctuate with each timestep; therefore the 0.5 m spacing was kept constant for the beach face. From the beach face to the dune, the spacing was again varied linearly, with the spacing varying from 0.5 m to 2 m. The y-direction grid spacing is 10 m. The number of cells in the x-direction for all runs is 170. The number of cells in the y-direction is 100 for the no bar and bar grids, and 200 for the bar-rip grids.

The length of the grid in the x-direction for all runs is 1087 m (the linearly decreasing grid spacing does not allow for a rounded length such as 1100). For the bar and no-bar runs, the length of the grid in the y-direction is 1000 m. The bathymetry for these runs is constant in the alongshore direction, and therefore the grid did not need to be exceptionally long in the alongshore direction. However, for the bar-rip grids, the rip should cause variations that extend alongshore into the bar sections of the grid. Therefore the length of the bar-rip grids is 2000 m in the y-direction in order to capture the variations in the alongshore direction.

Examples of all three grid types, no-bar, bar, and bar-rip, are shown in Figure 3-14, Figure 3-15, and Figure 3-16, respectively. The horizontal plane in all figures represents the still water surface.

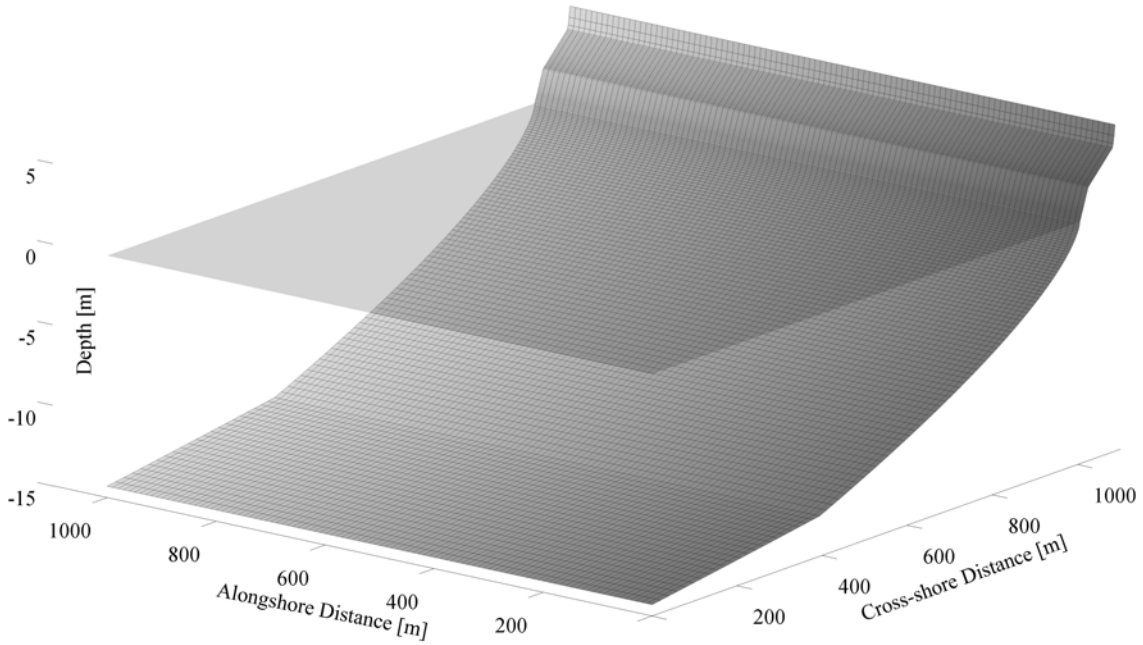

Figure 3-14 3D No-Bar Bathymetry. Three-dimensional example of a no bar bathymetry. The horizontal plane represents the still water surface.

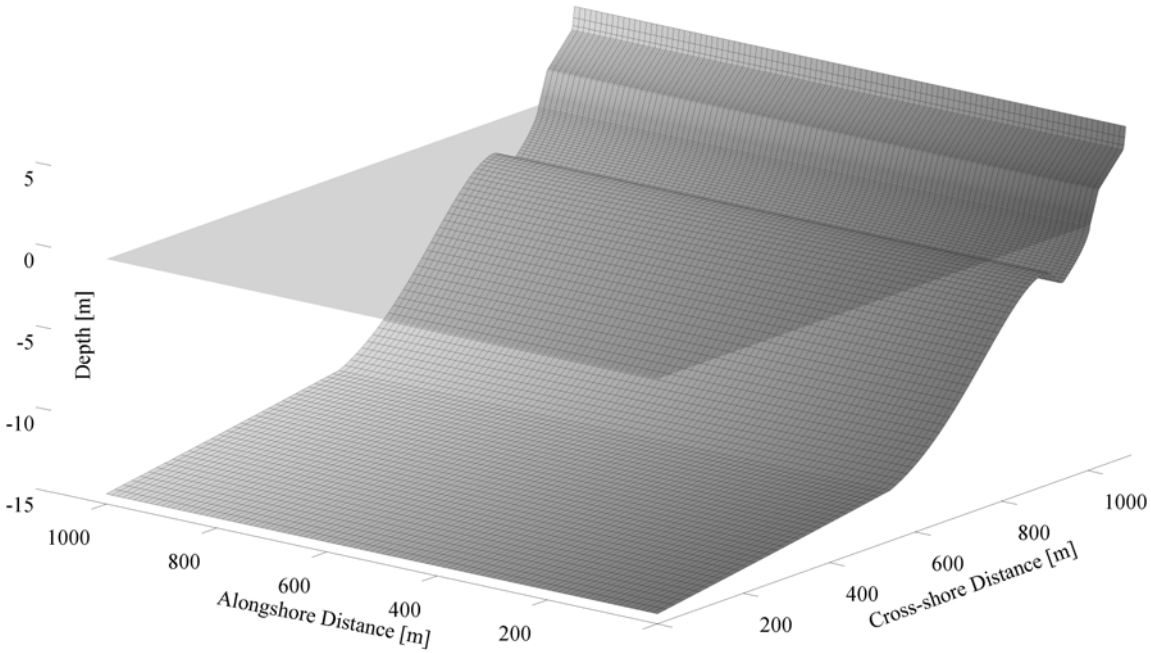

Figure 3-15 3D Bar Bathymetry. Three-dimensional example of a bar bathymetry. The horizontal plane represents the still water surface.

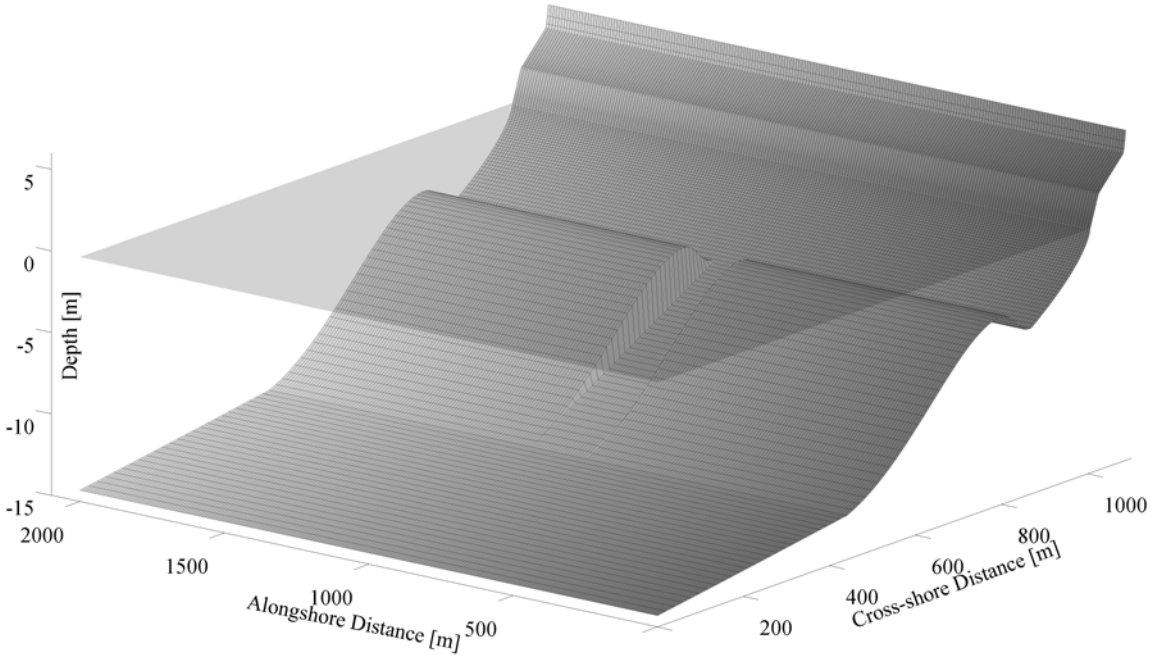

Figure 3-16 3D Bar-Rip Bathymetry. Three-dimensional example of a bar-rip bathymetry. The horizontal plane represents the still water surface.

3.5.2 Boundary Conditions

XBeach calculates an input wave energy time-series for wave energy forcing at the offshore boundary. For this thesis, a JONSWAP (Joint North Sea Wave Observation Project) spectrum (Hasselmann et al., 1973) is used for the wave energy forcing, which is only applied at the offshore boundary McCall 2010).

XBeach uses the method of Van Dongeren (2003), where it is assumed that the input wave spectrum is composed of a certain number of wave components. The phase of each component is determined at random, while the frequencies are distributed uniformly around the peak of the wave spectrum. The wave direction is also determined with a random process, however in this thesis the wave direction is held constant, with all waves normally incident to the shoreline. The wave component amplitude is then calculated after determining the phase, frequency, and direction. This leads to the input time-series of wave energy at the offshore boundary.

3.5.3 Other XBeach Parameters

Along with the grid files and the wave file, the third XBeach input for this thesis is the parameters file. The parameters file controls different parameters for physical processes, grids, physical constants, time management, the wave action balance, wave dissipation model, wave roller model, wave boundary conditions, flow input, tide and surge conditions, sediment transport, morphological updating, avalanching, and limiters for certain physical processes. For many of the parameters, the default value was used. Therefore, this section will describe only parameters that are not set to the default value.

The physical processes that are turned on for the XBeach runs in this thesis include long and short wave generation, and flow. Most of the wave energy input by the model is long wave energy, however by including short wave generation a small amount of short wave energy is included. The amount of short wave energy is not realistic, as the amount of short wave energy input by the model is less than real conditions. Sediment transport and morphological updating is turned off for most runs completed, however several runs were completed with sediment transport and morphological updating on. The reason for this is that currently XBeach is mainly used for modeling dune erosion during extreme storm events, where sediment transport is mostly eroded, and no accretion occurs. Therefore, the beach restoring processes that cause sand to accrete on the beach, and counter the amount of erosion that occurs are not included in the sediment transport equations in XBeach at the present time. This causes an unrealistic amount of erosion on the beach. As XBeach is an evolving model, the inclusion of these processes in the model is currently being completed, and should be finished by Fall 2011. While this rules out quantitatively studying the amount of erosion that occurs during the runs presented in this thesis, the erosion can be studied qualitatively, and was done so for the runs that included sediment transport and morphological updating in this thesis.

The number of wave directions is set with the upper and lower directional limits and directional resolution. For this thesis, the upper and lower directional limits for the wave directions are set so that only 1 directional wave bin is created. This way all waves propagate normal to the shoreline.

Each numerical simulation is run for 9000 seconds, or 2.5 hours. The model is

given 0.5 hours to “ramp up”, meaning the offshore forcing is gradually increased to full strength over the first 0.5 hours. This is done to prevent any numerical instabilities.. Therefore, 2.0 hours worth of data is recorded for each run. In order to accurately resolve the wave motions at the shoreline, the time interval was set to 1 second. The period of the wave motions at the shoreline vary from 15 seconds to more than a minute, so a 1 second time interval ensured that the peak of the wave was recorded.

Artificial boundary conditions are specified in XBeach for all four edges of the grid. Boundary conditions are necessary to treat the waves, currents, and sediment that encounter the edge of the grid. The boundary conditions are necessary to transmit the waves, currents, or sediment through the boundary. The offshore boundary is imposed as a weakly reflective absorbing-generating boundary. The lateral, alongshore boundaries are described as Neumann boundaries.

XBeach also allows for the specification of fluctuations in the water level due to tides or storm surge. For this thesis, the water level over the bar is an important factor in the influence that the bar has on the incoming waves. Therefore, keeping the still water level constant during the runs is important to focus on the influence of the wave and bar conditions between simulations. For this reason, tides were not included in the model for this thesis, and the initial water level is set to zero. Similarly, to keep the number of variables at a minimum, wind was not included in the model.

For runs with sediment transport and morphological updating, sediment transport was not turned on until the ramp time was over. Therefore, two hours of sediment transport and morphological updating occurred during each run. XBeach includes a

factor that speeds up the sediment transport and morphological updating. This is used for simulating longer periods of morphological change with smaller run time, and less computational time. For this thesis, the sediment transport was kept at real-time rates.

3.6 Description of Supercomputer used for Simulations

XBeach was compiled and run on a supercomputer for this thesis. This allowed the simulations to be run in parallel, so that multiple processors could be used at once for the computations. The supercomputer used is eos, located at Texas A&M University, and as of the writing of this thesis contains 372 cores, with 8 processors per core. For each run, 5 processors were utilized, resulting in run times of less than 25 minutes.

3.7 Data Analysis

This section will briefly describe the basic data analysis that was completed for each simulation. This includes extracting the shoreline location and elevation, and calculating the two-percent runup and significant infragravity swash.

For each numerical simulation, XBeach will output time series of water level, bed level, wave height, wave energy and roller energy. The water level and bed level outputs were used to extract the shoreline elevation for each time step. Figure 3-17 shows an example of a shoreline elevation time-series for the first 3000 seconds of a run.

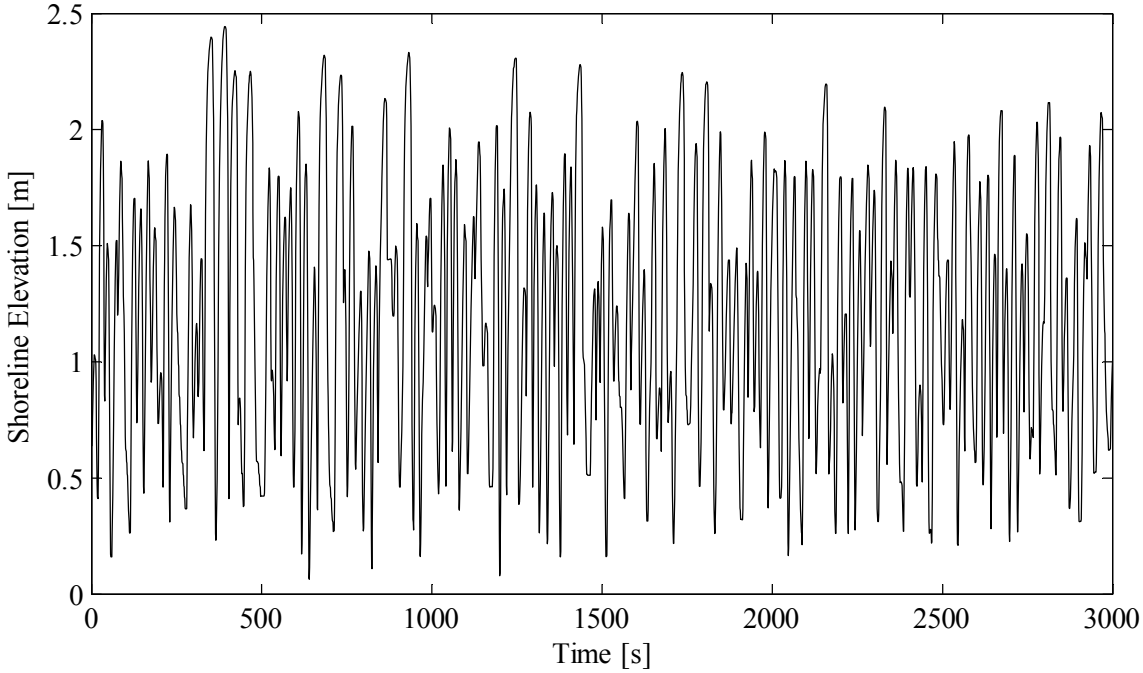

Figure 3-17 Shoreline Elevation Time-Series. Example time-series of shoreline elevation extracted from output of the water level and bed level from the numerical model XBeach.

From the shoreline elevation time-series, the significant runup is calculated. First, the setup is calculated by calculating the mean of the time series. This is the setup at the shoreline, which is defined as the average water level elevation above the still water level. The swash time-series is then calculated by subtracting the setup from the shoreline elevation time series. The swash is the shoreline variation about the setup. The zero up-crossing method is then used to isolate each individual runup occurrence, where the local swash maximum is the maximum swash value between successive zero up-crossing locations.

All local swash maxima are found for the swash time-series. The mean of the original shoreline elevation time-series is added to the local swash maxima to find all

individual runup values. These runup values are ranked in descending order, and the runup cumulative distribution function for the data is calculated. A Gaussian cumulative distribution function is then fit to the raw data. Doing this assumes that the runup values are normally distributed. The Gaussian fit is shown as the solid line in the following figure. From the Gaussian cumulative distribution function, the significant runup is calculated as the 2% runup, which is the runup elevation that is only exceeded 2% of the time (Holman, 1986). Therefore the 2% runup is the runup value that corresponds to the 98% probability of occurrence.

The time-series of the shoreline elevation is also used to determine the significant swash, which is defined as 4 times the standard deviation of the swash time series (Stockdon et al., 2006). The time-series of swash is transformed from time domain to frequency domain with a fast Fourier transform (FFT), to create a plot of the power spectrum density (psd). For this research, the psd is useful in studying the amount of wave energy in the infragravity range, which has been defined previously as frequencies less than 0.05 Hz. An example of a psd of calculated from the swash time-series is shown below in Figure 3-18.

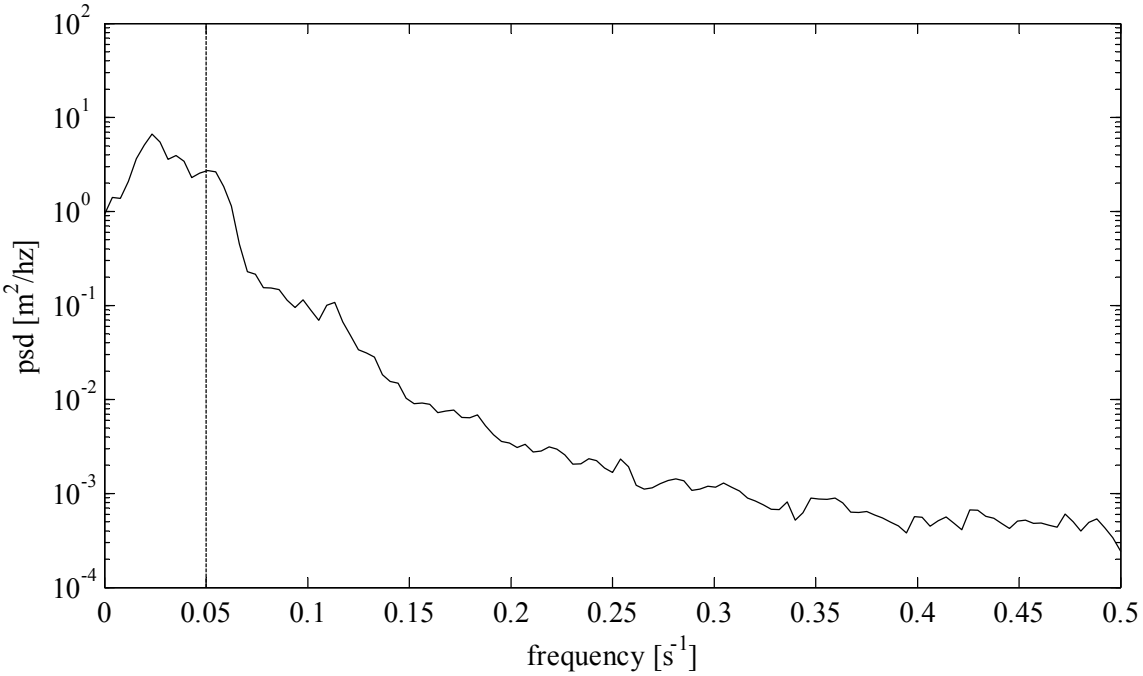

Figure 3-18 Swash PSD. An example of the power spectrum density calculated from the swash time-series. The dotted line represents the upper limit of the infragravity range, 0.05 Hz.

The area under the power spectrum density curve from 0 to 0.05 Hz represents the variance in the swash time-series that is associated with infragravity motions. The standard deviation, σ, is the square root of the variance, σ^2. The standard deviation is used to calculate the significant infragravity swash elevation, S_{IG}.

$$\sigma^2 = \sum \mathrm{PSD}(f)df,\ f<0.05\ \mathrm{Hz} \tag{3-32}$$

$$S_{IG} = 4\sigma \tag{3-33}$$

The significant infragravity swash and 2% runup are used as indicators of erosion at the shoreline, as wave motions at the shoreline have been shown to be a main source of erosion on beaches (Ruggiero et al., 2004). The values of significant swash and runup

for simulations with bar and bar-rip bathymetry are compared with simulations for no bar bathymetry to determine the influence of the bar and bar-rip on the amount of wave energy that reaches the shoreline.

Finally, the wave energy and roller energy outputs from XBeach are used to investigate the location of the start of wave breaking and the location where wave breaking ceases, with the distance between defined as the surf zone width. This is used in analyzing alongshore differences in infragravity energy as wave breaking is one method for the release of infragravity waves (Holman, 1981).

To briefly summarize the main data analysis done for this thesis, XBeach simulations are completed and the data is analyzed to determine the 2% runup and the significant infragravity swash. These parameters are viewed as important indicators of beach erosion during storm events and are used to determine the effect of local nearshore sandbars on the beach vulnerability.

4 RESULTS OF NUMERICAL SIMULATIONS

4.1 Introduction

This section provides results from the numerical simulations completed with the nearshore processes model XBeach. The results will determine the influence of the bar and bar-rip scenarios on the infragravity energy at the shoreline, and may be used as part of a beach vulnerability index. Results from the no-bar, bar, and bar-rip scenarios are discussed. Section 4.2 introduces the results of the no-bar scenario, which are used as a control in order to determine the influences of the bar and bar-rip bathymetries on the infragravity energy. Section 4.3 presents results from the bar scenario. The dependence of infragravity energy on wave height, as well as the dependence on the water level over the bar is shown. Finally, a new parameterization for the significant infragravity swash for an area with a nearshore sandbar in the local bathymetry is developed. Section 4.4 discusses the results of the bar-rip scenario. The results of the numerical simulations with no morphological changes, and results of the numerical simulations with morphological changes enabled are both discussed.

For simplicity, in the remainder of this thesis the location of a bar is represented by the distance to the bar and the bar depth separated by a forward slash. For example the 50 / 1.20 bar references a grid with a bar located 50 m from the shoreline at a depth of 1.20 meters.

4.2 General Results

This section briefly discusses several aspects of this research that apply to all

three bathymetric scenarios, including the directional distribution of wave energy and its effect on the alongshore distribution of infragravity energy, the distribution of runup, as well as information about the wave heights used to develop parameterizations of the infragravity energy.

For all numerical simulations, the directional distribution of wave energy was set up in the input to the numerical model such that all waves would approach the beach from a 90 degree angle, known as shore normal. Also, the bar and no-bar bathymetric scenarios are designed so that both are continuous and uniform in the alongshore direction. Given the shore normal alongshore distribution of wave energy, and the constant alongshore bathymetry, the alongshore distribution of infragravity energy for the no-bar and bar scenarios was expected to be uniform as well. The results of the simulations for the no-bar scenario show that the distribution of infragravity energy is uniform in the alongshore direction, and confirm that the waves are shore normal. This is also true for the simulations completed for all bar scenarios. This shows that the presence of a uniform alongshore bar in the nearshore bathymetry does not cause any alongshore variability of infragravity energy. Uniform alongshore variations of infragravity energy for uniform alongshore bathymetric scenarios allow for alongshore variations in the distribution of infragravity energy for the bar-rip scenarios to be attributed to the bathymetry.

The runup cumulative distribution function for the 50 / 1.20 m bar bathymetry and 1 m wave height is shown in Figure 4-1.

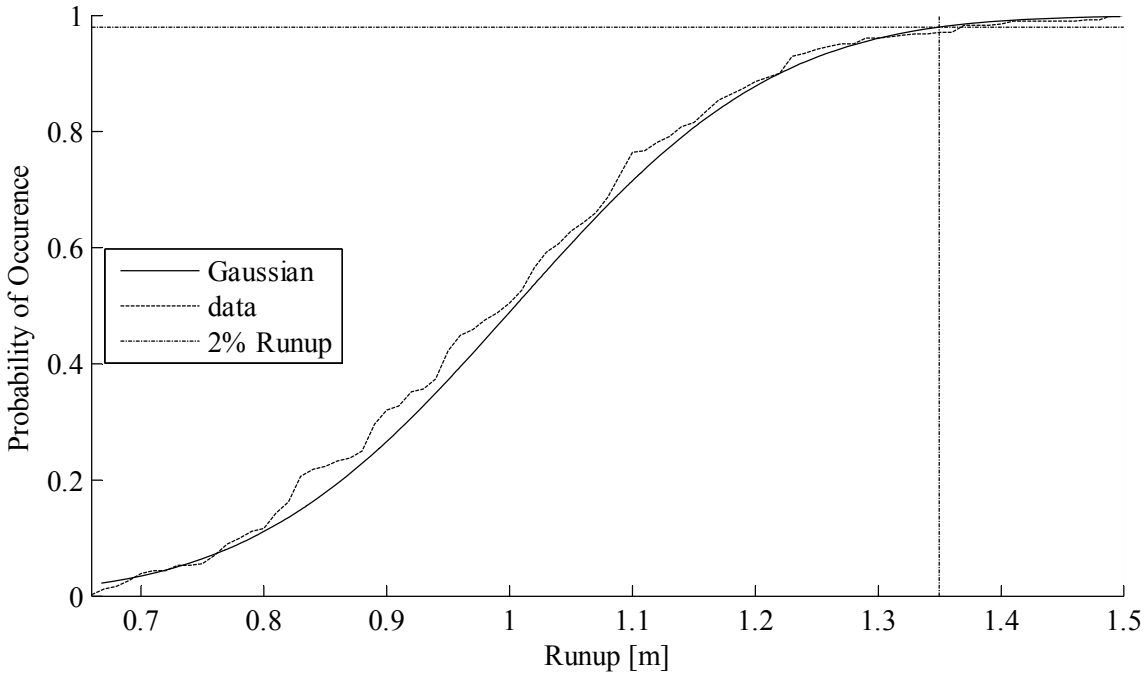

Figure 4-1 Runup CDF. The two-percent runup is calculated from the cumulative distribution function of the runup values. The dotted line is the cumulative probability as determined from the data, while the solid line is the cumulative distribution function fitted to the data. The dot-dash line represents the location of the 2% runup value.

In Figure 4-1 the dotted line represents the cumulative distribution calculated from the raw data, while the solid line represents the cumulative distribution function that has been fit to the data. The dot-dash line then represents the location and value of the two-percent runup. Figure 4-1 shows that the two-percent runup data tend to follow a normal distribution.

In order to determine the best parameterization of infragravity energy at the shoreline, wave heights at two different water depths were considered. The first is the offshore spectral wave height, which is used as input to the wave spectrum. The second is the spectral wave height calculated at a depth of 10 m. The wave height at this depth

was also considered by Guza and Thornton (1982) for research dealing with swash oscillations on beaches. For each specific bathymetry, simulations were completed for seven different wave heights: 1, 1.5, 2, 2.5, 3, 3.5, and 4 m. Figure 4-2 and Figure 4-3 show the two-percent runup and the significant infragravity swash plotted as functions of both the offshore spectral wave height and the spectral wave height calculated in a water depth of 10 m for the 50 / 1.20 bar grid for all seven wave heights.

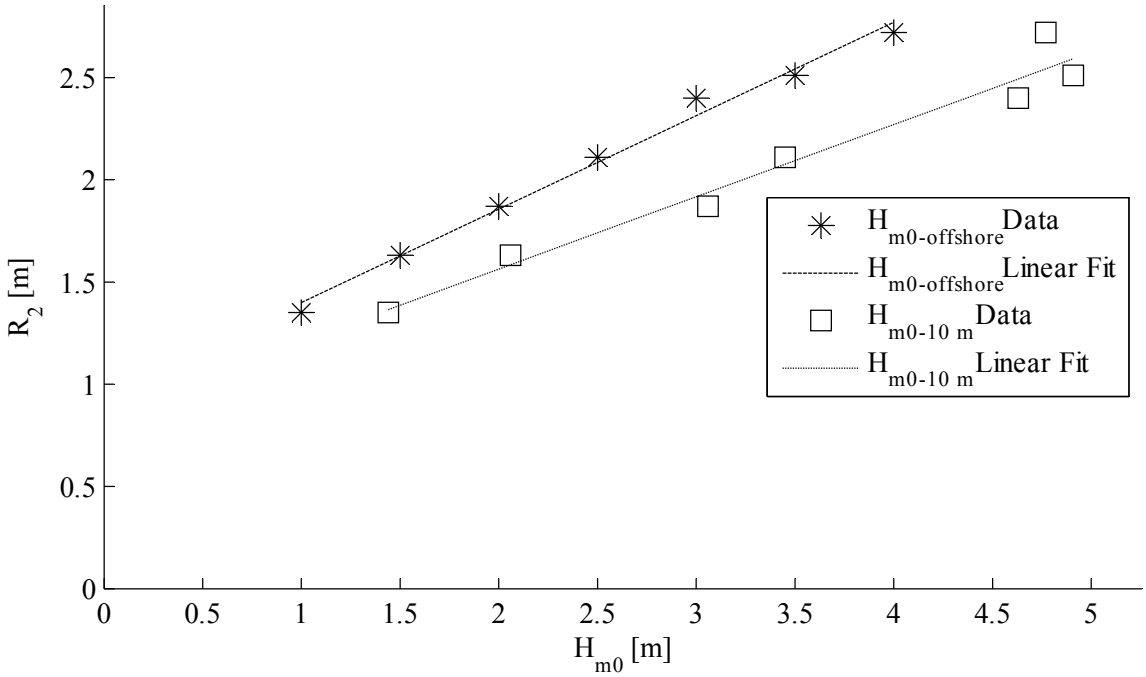

Figure 4-2 Two-Percent Runup vs. Offshore Wave Height for 50 / 1.20 m Bar. The two-percent runup increases linearly with an increase in spectral wave height. The spectral wave height provides a better fit than the significant wave height, calculated at a 10 m water depth, which is shown in Figure 4.4.

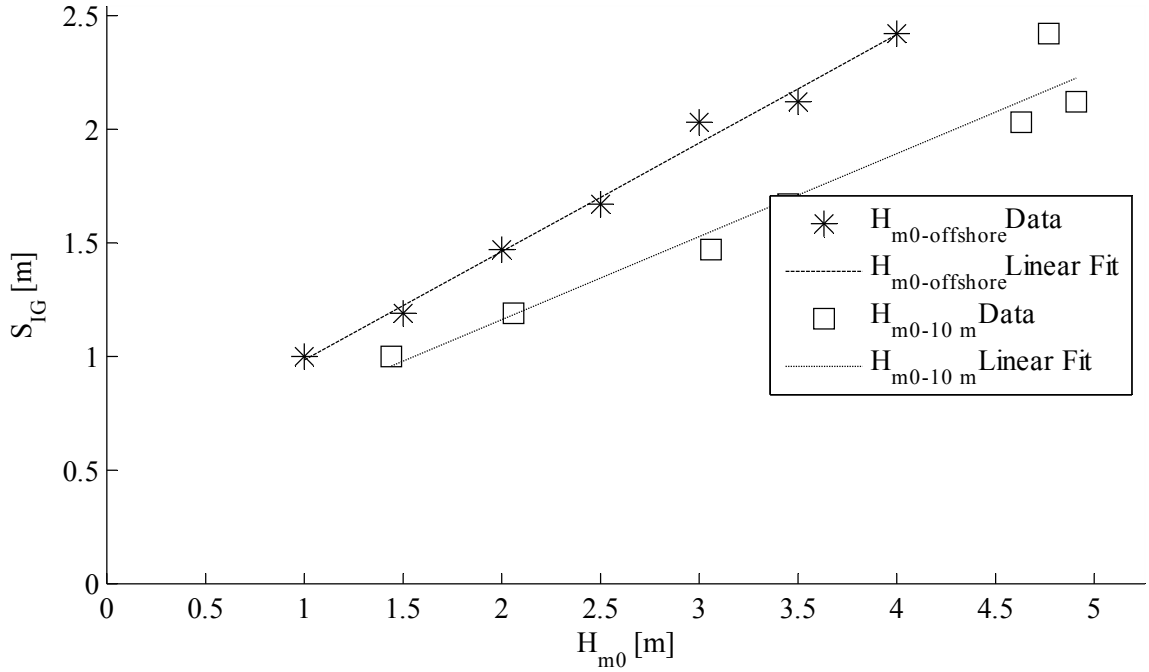

Figure 4-3 Significant Infragravity Swash vs. Wave Height for 50 / 1.20 m Bar. The two-percent runup increases linearly with an increase in significant wave height, calculated at a 10 m water depth. However, the fit is better when the two-percent runup is plotted against the spectral wave height, as shown in Figure 4-3.

Comparing Figure 4-2 with Figure 4-3, the fit is better with the offshore spectral wave height compared to the spectral wave height calculated at a water depth of 10 m. This is most likely due to the larger waves beginning to break before reaching the 10 m water depth, limiting the significant wave height at 10 m depth. For this reason, the offshore spectral wave height is used for all further analysis in this thesis.

4.3 Results of No-Bar Simulations

The no-bar bathymetry scenario is the control case for the bar and bar-rip scenarios. Simulations for the no-bar scenario were completed to make comparisons

with the bar and bar-rip simulations in order to determine how the infragravity energy is influenced by the presence of the nearshore sandbar and the bar-rip bathymetries.

Seven simulations were completed for the no-bar bathymetry. All variables were held constant between the seven simulations with the exception of the wave height. The wave height was varied between simulations from 1 to 4 meters at 0.5 m increments. For each simulation, the significant runup, which is defined as the two-percent runup, and the significant infragravity swash elevations were found. These values are used to determine the reduction of infragravity energy due to the presence of the nearshore sandbars. The results of the seven no-bar simulations are shown below in Table 4-1. The two-percent runup and infragravity energy both increase with an increase in the wave height.

Table 4-1 Results of No-Bar Simulations

H_{m0}	R_2	S_{IG}
1.0	1.50	1.21
1.5	1.90	1.65
2.0	2.29	2.23
2.5	2.55	2.48
3.0	2.71	2.62
3.5	2.74	2.63
4.0	2.96	2.79

4.4 Results of Bar Simulations

4.4.1 Bar Simulations Introduction

The bar simulations were completed to determine the influence of a uniform alongshore bar in the nearshore bathymetry on the amount of infragravity energy at the

shoreline. The location of the bar and the wave height are varied between simulations. For each of the simulations, the two-percent runup and significant infragravity swash were calculated. These values are compared to the values of two-percent runup and infragravity swash for the no-bar grids. Two sets of simulations were completed for the bar bathymetry. Each set contains 6 different bathymetries with varying distances to the bar from the shoreline. The distance to the bar from the shoreline for the six different bar locations in each set is the same. The difference between the sets is that one set has bar depths that correspond to a mid-tide water level while the other set has bar depths that correspond to an extreme low-tide water level. For each of the 12 total bathymetric setups, simulations were completed for 7 different wave heights. Therefore there were 84 total simulations completed with a bar bathymetry. In the following sections, the alongshore variation of infragravity energy and the differences in infragravity energy for bars at different tide levels are discussed. The dependence on wave height and the amount of infragravity energy reduction between bar and no-bar cases are shown, and the results for all 84 simulations are combined to present a new parameterization of significant infragravity swash.

4.4.2 Typical Bar Simulation Results

Due to the large number of simulations completed for the bar scenario, this section will only provide typical results from a simulation completed for the bar bathymetry. This includes the relationship between wave height and infragravity energy, and the influence of the nearshore sandbars on the infragravity energy at the shoreline. Results are shown for the 50 / 1.20 bar bathymetry. The 50 m distance from the bar to

the shoreline is the closest bar distance from the shoreline tested in this thesis.

The relationship between the two-percent runup and the wave height, as well as the relationship between the infragravity runup and the wave height is linear. For these simulations, both the two-percent runup and the significant runup increase linearly with increasing spectral wave height. This result was expected, as an increase in wave height should lead to an increase in energy associated with infragravity motions (e.g. Stockdon et al., 2006; Ruggiero, 2004). A table with the results for both two-percent runup and significant infragravity wave height for all bar simulations is located in the appendix. For all bar simulations, the general trend is for the two-percent runup and infragravity swash to increase with an increase in wave height.

The influence of the bar on the infragravity motions at the shoreline can be determined by comparing the results of the bar simulations with results from the no-bar simulations. Figure 4-4 and Figure 4-5 show the difference between the no-bar simulation and 50 / 1.20 bar simulation for both the two-percent runup and significant infragravity swash.

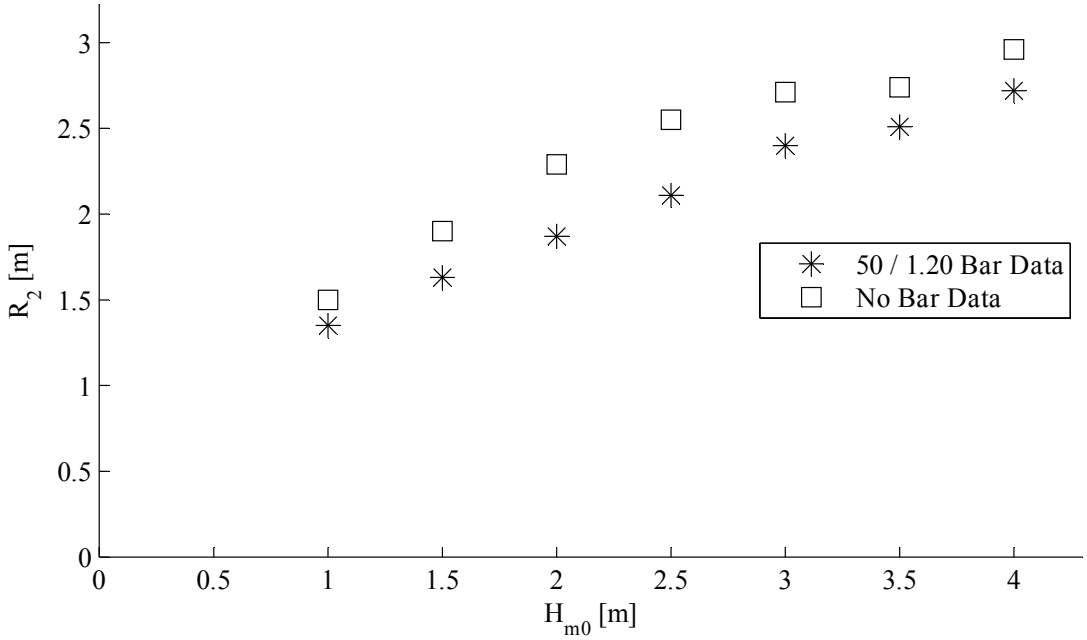

Figure 4-4 Bar and No-Bar Two-Percent Runup. The two-percent runup for the bar scenario is less than the no-bar scenario with the same wave height. This demonstrates that the bar influences the infragravity energy at the shoreline.

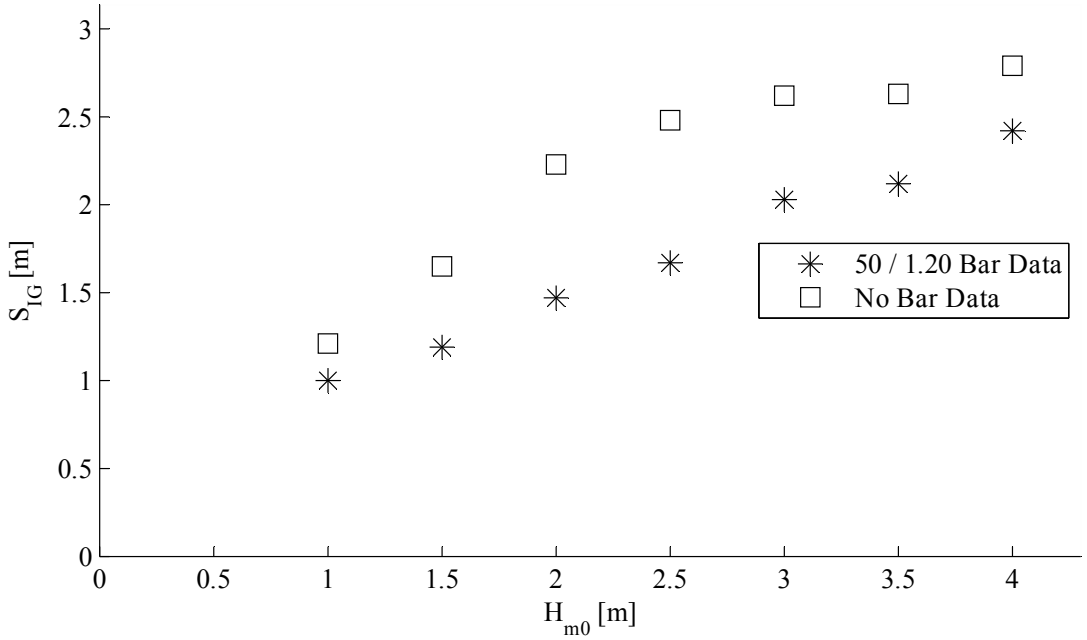

Figure 4-5 Bar and No-Bar Significant Infragravity Swash. The significant infragravity swash for the bar scenario is less than the no-bar scenario with the same wave height. This demonstrates that the bar influences the infragravity energy at the shoreline.

Figure 4-4 and Figure 4-5 show that for both two-percent runup and infragravity swash, the presence of the nearshore sandbar has the effect of decreasing the amount of infragravity at the shoreline. For both two-percent runup and infragravity swash, the difference between the bar and no-bar bathymetric scenarios is greater for the 2, 2.5 and 3 m wave heights than the other wave heights. The difference between the bar and no-bar bathymetric scenarios is smallest for the 1 m wave height. This is expected as the bar should not affect the 1 m wave height as much as the larger wave heights.

4.4.3 Influence of Water Level on Infragravity Energy

The 50 / 0.60 bar grid is the low-tide version of the 50 / 1.20 bar grid, which represents the bar at mid-tide. By comparing the results of the two scenarios, the influence of the water level over the bar for the same bar distance to the shoreline is observed. The infragravity energy and two-percent runup results for both water levels over the bar are shown in Figure 4-6 and Figure 4-7, respectively.

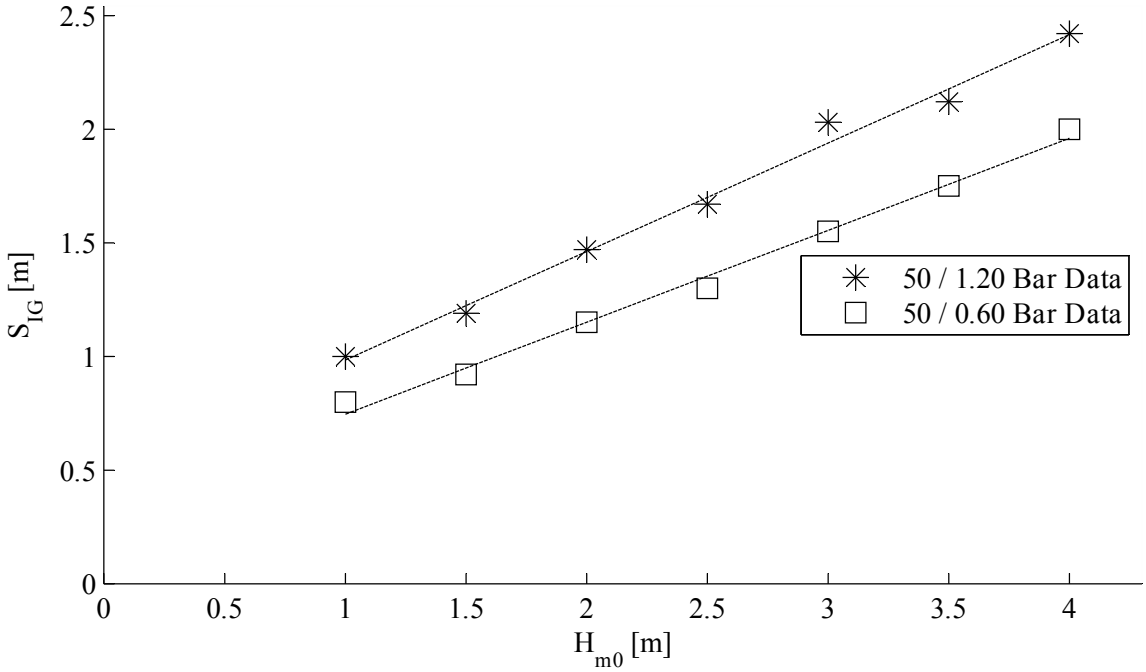

Figure 4-6 Mid-Tide and Low-Tide Significant Infragravity Swash. The low-tide simulation results in less significant infragravity swash than the mid-tide simulations. This demonstrates the effect of the water level over the bar on the infragravity energy at the shoreline.

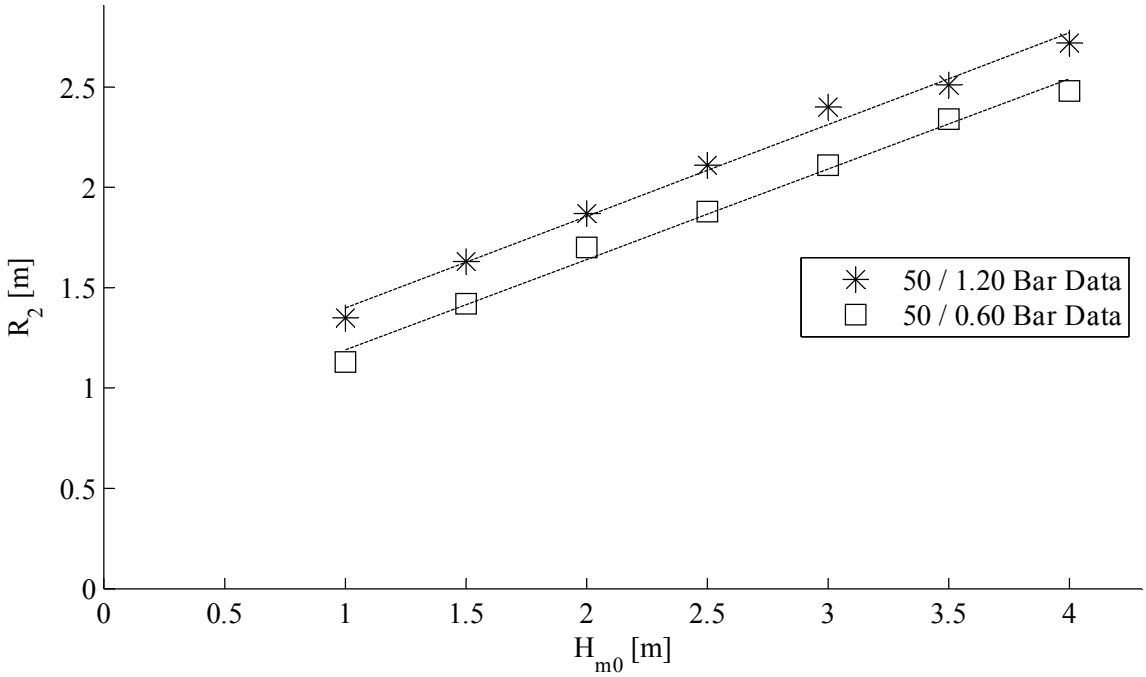

Figure 4-7 Mid-Tide and Low-Tide Two-Percent Runup. The low-tide simulation results in a lower two-percent runup elevation than the mid-tide simulations. This demonstrates the effect of the water level over the bar on the infragravity energy at the shoreline.

Figure 4-6 and Figure 4-7 show that the bar with the low-tide water level results in less infragravity energy at the shoreline than the mid-tide water level bar in terms of both the significant infragravity swash and the two-percent runup.

The percent reduction in infragravity energy for both tide levels when compared to the no-bar case is shown in Table 4-2.

Table 4-2 Bar Bathymetry Infragravity Energy Reduction. The percent reduction in significant infragravity swash and two-percent runup when compared to no-bar simulations for mid-tide and low-tide simulations.

Wave Height [m]	**Percent Reduction of S_{IG} [%]**		**Percent Reduction of R_2 [%]**	
	Mid-Tide 50 / 1.20	Low-Tide 50 / 0.60	Mid-Tide 50 / 1.20	Low-Tide 50 / 0.60
1.0	17	34	10	25
1.5	28	44	14	25
2.0	34	48	18	26
2.5	33	48	17	26
3.0	23	41	11	22
3.5	19	33	8	15
4.0	13	28	8	16

For both significant infragravity swash and two-percent runup, the 50 / 0.60 bar reduces the infragravity energy at the shoreline by a higher percentage than the 50 / 1.20 bar when compared to the no bar condition for all wave heights. This demonstrates that the water level over the bar plays a role in the amount of infragravity energy that reaches the shoreline.

It should also be noted in Table 4-2 that the percent reduction is higher for the infragravity energy than the two-percent runup. This is most likely due to the fact that

the short wave energy is included in the two-percent runup, but not in the significant infragravity swash. The short waves break over the bar, but then reform over the trough, gaining back lost energy. Therefore the influence of the bar on the short wave energy is different than the influence of the bar on the infragravity energy.

4.4.4 A Parameterization for Significant Infragravity Swash

The main goal of this thesis is to determine a parameterization for infragravity energy at the shoreline for beaches in areas with bathymetries that include nearshore sandbars. This parameterization could possibly be used as part of an erosion vulnerability scale for areas with nearshore sandbars. It was shown in Figure 4-2 and Figure 4-3 that the infragravity energy at the shoreline increases with an increase in spectral wave height. Also, Figure 4-6 and Figure 4-7 show that the depth of the bar influences the reduction of infragravity energy at the shoreline when compared to the no bar cases. Thus a parameterization of infragravity energy should include wave height and the depth of the bar.

Stockdon et al. (2006) determined that the significant infragravity energy was best parameterized by the offshore significant wave height, H_0, and the deepwater wave length, L_0.

$$S_{IG} = 0.06(H_0 L_0)^{0.5} \tag{4-1}$$

The data from all 84 bar simulations are plotted using the Stockdon (2006) parameterization for infragravity swash in Figure 4-8.

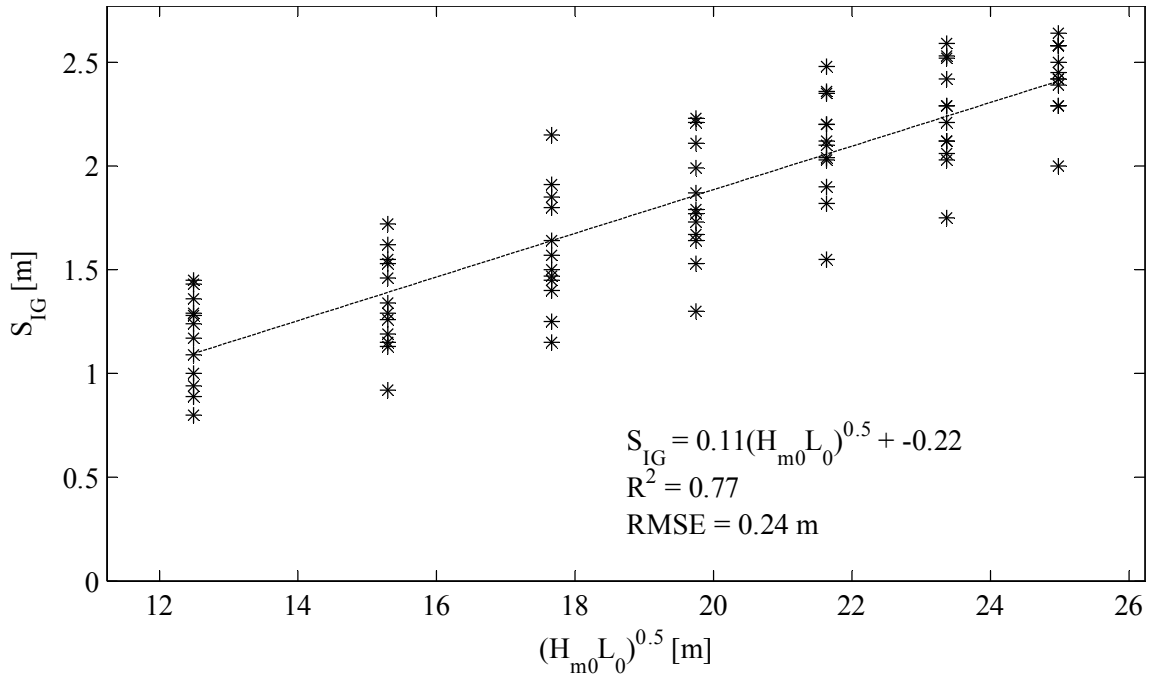

Figure 4-8 Stockdon et al. (2006) Parameterization. Parameterization of significant infragravity swash using data from all 84 bar simulations and the formulation of Stockdon et al. (2006). The trend is a linear; S_{IG} increases with increasing spectral wave height. However there is significant variance about each specific wave height. This variance is due to the difference in the location of the nearshore sandbar between each grid.

It is important to note that the peak wave period input to the JONSWAP wave spectrum is kept constant at 10 s for all simulations. Therefore the deepwater wavelength is also constant for all simulations. As expected, the data increase linearly with the Stockdon et al. (2006) parameterization. However, it is obvious that there is a large amount of variation between simulations at each specific wave height. This variation is due to the difference in the bar location between the different grids. This plot shows again that the presence of the nearshore sandbar in the local bathymetry can have a large influence on the infragravity energy at the shoreline, in this case the significant infragravity swash. It also shows the need for a parameterization that includes features of

the nearshore sandbars.

In order to create a parameterization that includes features of the nearshore sandbars a new variable, $\frac{h_B}{h_{NB}}$, is introduced, where h_B represents the bar depth and h_{NB} represents the no-bar depth. This variable represents the percent reduction in the water depth due to the bar when compared to a theoretical water depth if a bar was not present. The h_{NB} term is determined by connecting a line from the deepest part of the bar trough with the end of the bar. The depth of the line at the point corresponding to the top of the bar is then h_{NB}. The numerator, $h_{B,}$ is the depth of the top of the bar. An example is shown in Figure 4-9. The dotted line is the line between the bar trough and the end of the bar, while the dot-dash line represents the theoretical no-bar depth.

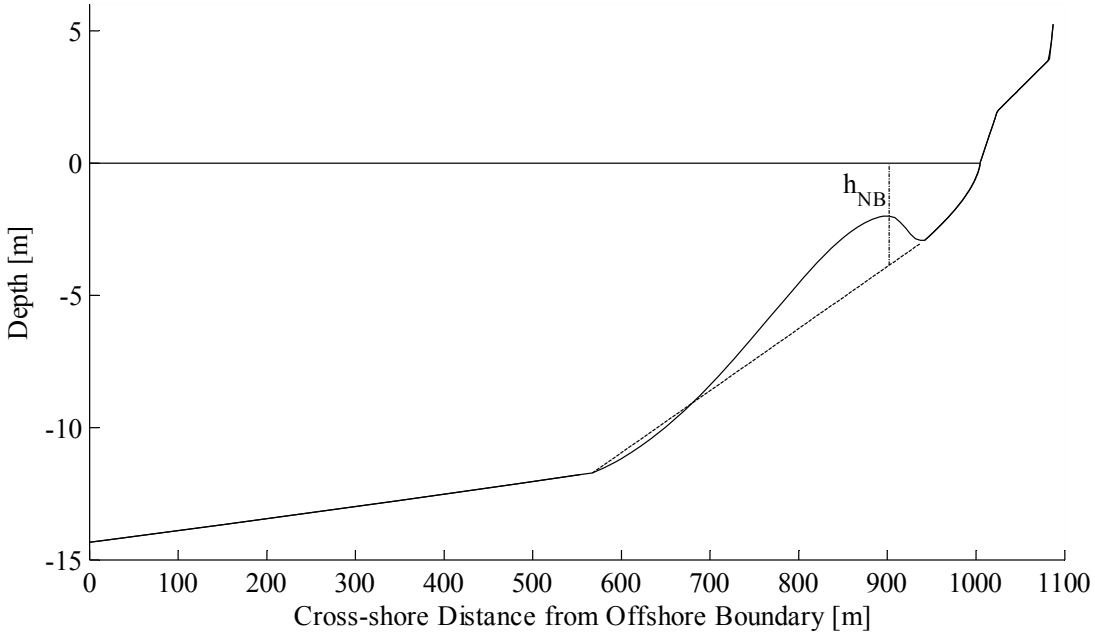

Figure 4-9 Theoretical No-Bar Depth. Example of theoretical no-bar depth calculation for bar grids. The dotted line is the line between the bar trough and the end of the bar, while the dot-dash line represents the theoretical no-bar depth.

The use of a more complex method for determining the no-bar depth such as using an equilibrium profile instead of a line was explored; however the difference in results was not significant enough to warrant using a different, more complex method.

The variable $\frac{h_B}{h_{NB}}$ is combined with the parameterization by Stockdon et al. (2006), where α is a constant.

$$S_{IG} = \left(\frac{h_B}{h_{NB}}\right)^{\alpha} (H_0 L_0)^{0.5} \quad (4\text{-}2)$$

The results of curve fitting show that by including the variable $\frac{h_B}{h_{NB}}$ with the wave height and wavelength terms inside the square root (α = 0.5), the variance is greatly decreased when compared to the Stockdon et al. (2006) parameterization. This is shown in Figure 4-10.

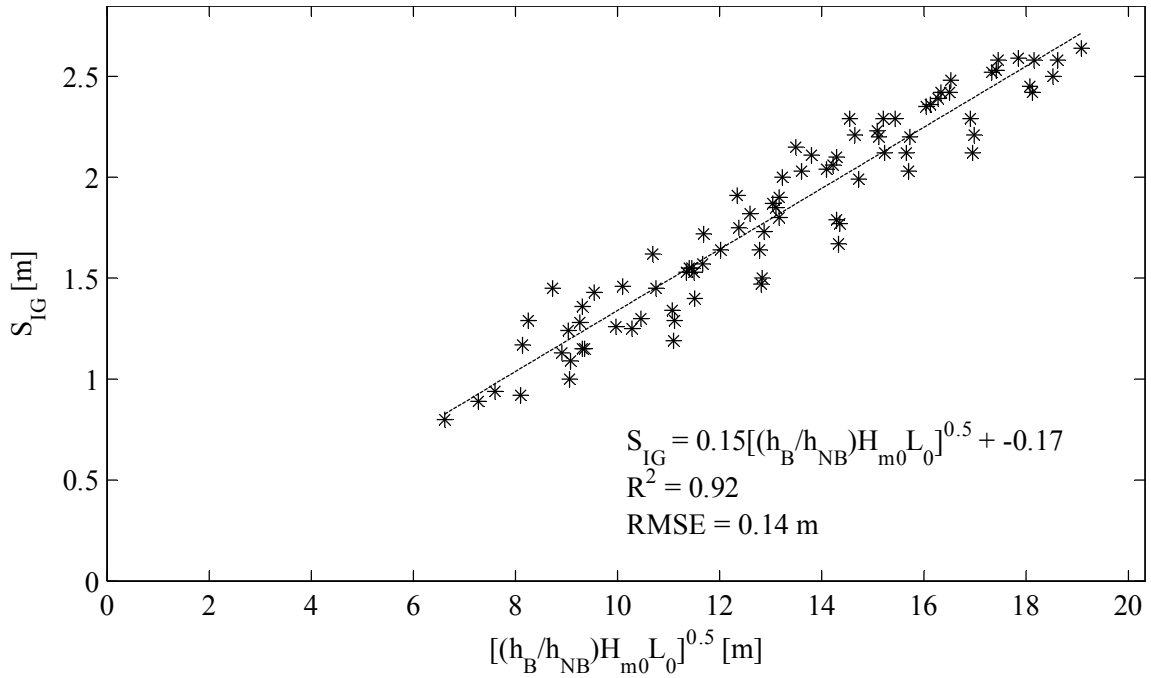

Figure 4-10 Parameterization of Significant Infragravity Swash. Parameterization of significant infragravity swash by including the variable $\frac{h_B}{h_{NB}}$ with the Stockdon et al. (2006) parameterization.

The inclusion of the term $\frac{h_B}{h_{NB}}$ in the Stockdon et al. (2006) parameterization results in a large decrease in the scatter. The correlation, R^2, increases from 0.77 to 0.92, and the root mean square error decreases from 24 cm to 14 cm. This shows that in areas with nearshore sandbars in the local bathymetry, the infragravity energy is not only dependent on wave height and wavelength, but also on the dimension of the bar.

It was shown above in Figure 4-10 that the amount of scatter in the parameterization of significant infragravity swash is reduced with the inclusion of the term $\left(\frac{h_B}{h_{NB}}\right)^{\alpha}$, with $\alpha = 0.5$. However, in order for the parameterization to be physically correct, the y-intercept should be zero. This is because as the wave height reaches zero,

the swash should also be zero. In the above parameterization, this is not the case, as a 0 m wave height would result in -17 cm of significant infragravity swash. However, by setting α equal to 0.75 instead of 0.5, the y-intercept becomes zero, as shown in Figure 4-11.

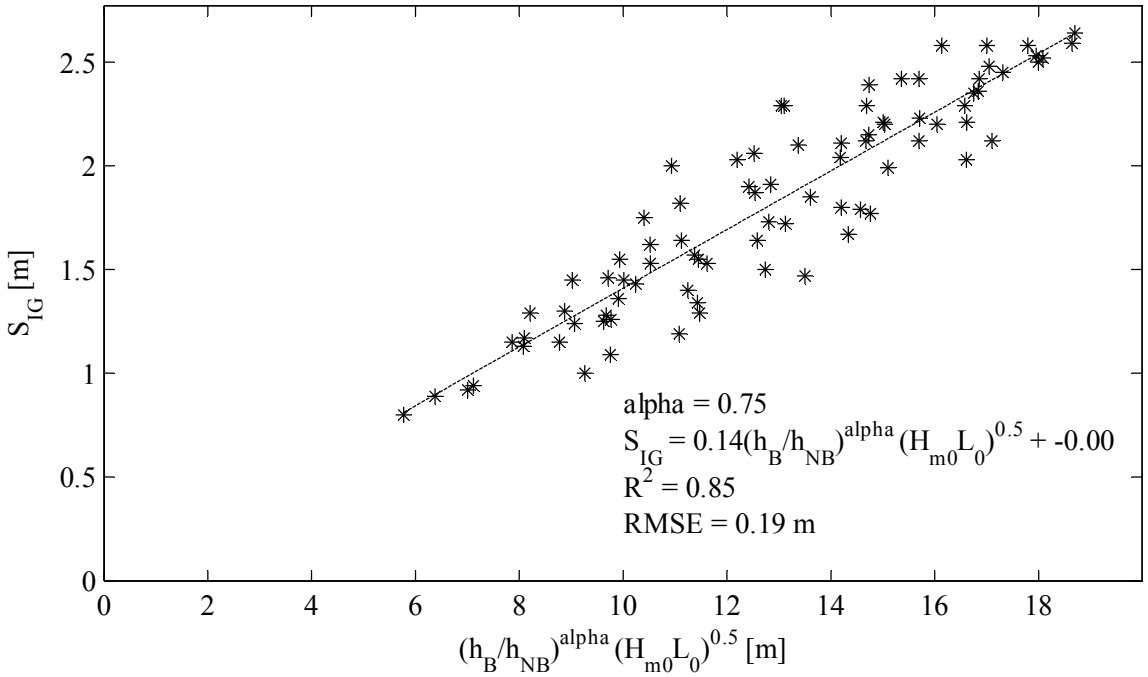

Figure 4-11 Parameterization of Significant Infragravity Swash, α = 0.75. The scatter is increased slightly, however the y-intercept is now 0, which is physically correct.

Using α = 0.75 slightly increases the scatter in the parameterization. The correlation decreases from 0.92 to 0.85, and the root mean square error increases from 14 cm to 19 cm. However, the parameterization is now physically correct, and the correlation and root mean square error show that the scatter is less than the parameterization of Stockdon et al. (2006).

This section presented the development of a new parameterization for the significant infragravity swash for an area with a nearshore sandbar in the local bathymetry. The parameterization is based on the general significant infragravity swash parameterization given by Stockdon et al. (2006). A new term representing the percent reduction of the water column due to the bar, compared to a no-bar bathymetry is presented. Adding this term to the parameterization was shown to improve the overall fit of the swash parameterization.

4.5 Bar-Rip Results

4.5.1 Morphological Updating Off

4.5.1.1 Bar-Rip Introduction

The bar-rip scenario bathymetry is a combination of the bar and no-bar bathymetry. It consists of a continuous, uniform nearshore sandbar with a break in the middle of the grid where there is no sandbar; this section is known as the rip. The width of the rip is varied, but is always located in the middle of the grid in the alongshore direction for all simulations. This way the length of the alongshore bar is equal on either side of the rip.

Two sets of simulations were completed for the bar-rip scenario. The difference between the two different sets is the width of the rip. The rip widths that were tested for this thesis are 100 and 200 meters. For each rip width, simulations were completed for four different bathymetries. The variable between the four different bathymetries is the location of the sandbar. For each separate bathymetry, a simulation was completed for

the same seven wave heights as the no-bar and bar scenarios; 1, 1.5, 2, 2.5, 3, 3.5 and 4 m. A total of 42 simulations were completed for the bar-rip bathymetry.

For each simulation, the two-percent runup and significant infragravity swash were calculated at the shoreline for each grid point in the alongshore direction. In order to analyze the data, the grid was split into five sections. The first section is the area directly behind the rip. The next two sections are defined as the transition regions on either side of the rip. They consist of the area behind the bar from the edge of the rip out to a distance equal to the width of the rip away from the edge of the rip. For example, with a rip width of 100 m, the transition regions span from the edge of either side of the rip to the point that is 100 m away from the edge of the rip. Finally, the last sections are the regions behind the bar, excluding the transition regions. The different sections can be seen below in Figure 4-12. The maximum and average values of both two-percent runup and significant infragravity swash were calculated for the area behind the rip, the area behind the transition regions, and the area behind the bar. A table containing these values for all simulations completed for the bar-rip scenario is located in the appendix.

4.5.1.2 Alongshore Variation of Infragravity Energy

The presence of the rip in the bar-rip bathymetry results in significant alongshore variation of the distribution of infragravity energy. This is different than the bar and no-bar scenarios, which resulted in uniform alongshore distribution of infragravity energy. Therefore the alongshore variation of infragravity energy can be attributed to the presence of the rip. The alongshore distribution of infragravity energy varies as the wave height varies from 1 m up to 4 m. An example of the alongshore variation of the two-

percent runup is given below in Figure 4-12.

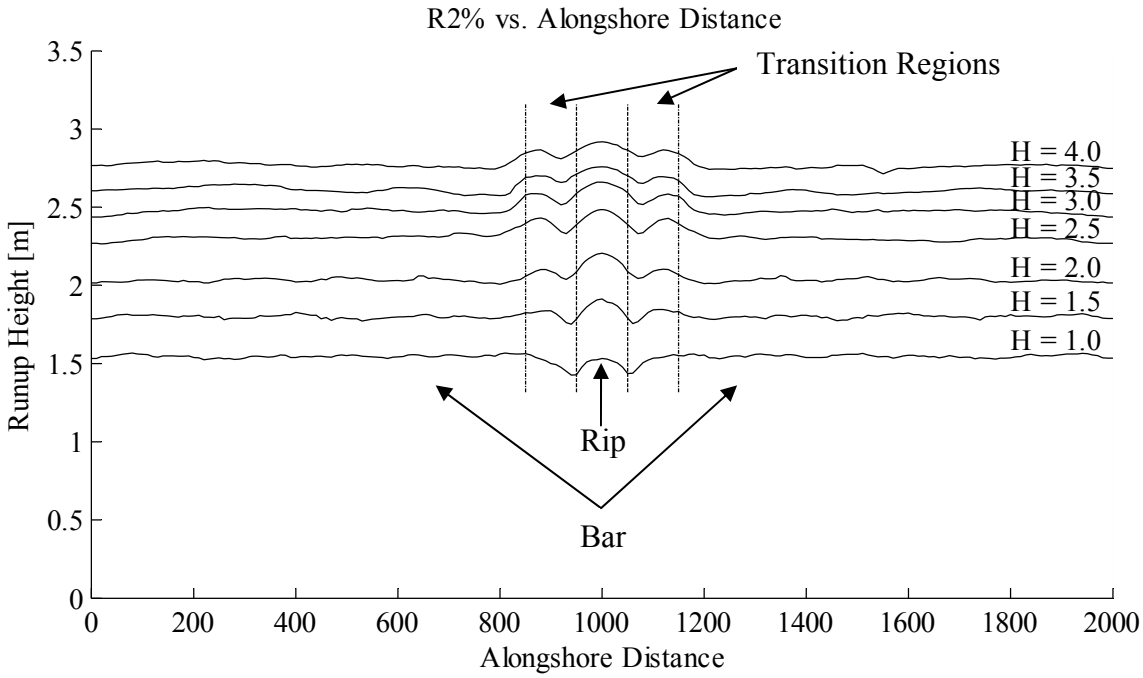

Figure 4-12 Bar-Rip Two-Percent Runup. Alongshore distribution of two-percent runup for wave heights of 1-4 m.

In general, the alongshore shape of the two-percent runup contains a peak at the point in the shoreline that corresponds to the middle of the rip, with separate peaks to the left and right of the main peak, which occur in the transition region. The values of the two-percent runup then tend to smooth out towards the sides of the grid, with only minor variations. It is obvious that the cause of the alongshore variations is the presence of the rip interrupting the alongshore bar. The exact effect of the rip on the infragravity energy however is unknown. One idea is that the rip bathymetry may cause local refraction, turning the energy towards the bar on either side of the rip, and consequently producing

the peaks in the transition regions. Another idea is that an edge wave is produced as the infragravity energy travels through the rip. The edge wave can then become trapped in the nearshore region by the local bathymetry (e.g. Holman, 1981).

In Figure 4-12 the alongshore variation is different for the 1 m wave height compared to all other wave heights. Interestingly, only the center peak occurs, and the peak value from the area behind the rip is less than the values for the areas behind the bar. The same pattern also occurs for the other bar-rip bathymetries that were tested. For the simulations completed, it was determined that when the wave height is greater than about 60% of the bar depth, the two-percent runup is greater for areas behind the rip, and if the wave height is less than about 60% of the bar depth the two-percent runup is greater for areas behind the bar. The exact reason for this is unknown; however it was found that there is a correlation between the surf zone width and the magnitude of the two-percent runup. The surf zone width is defined as the distance from the point where the wave begins breaking to the point where the wave ceases breaking. For all simulations, the alongshore location where the surf zone width was longer resulted in a higher two-percent runup than the location where the surf zone width was shorter. One idea about infragravity wave creation states that infragravity waves bound to wave groups are released as the short waves break (Holman, 1981). Therefore the surf zone width may influence the infragravity energy that is released by creating a larger infragravity wave. It is also possible that the larger surf zone width results in an infragravity wave with a longer period, which might cause the higher runup values. Finally, it should be noted that while the presence of a current through the rip might

affect the waves through the rip and influence the infragravity energy, wave-current interaction was not calculated by XBeach for the simulations completed for this thesis.

4.5.1.3 Significant Infragravity Swash Parameterization

The parameterization that was developed for the bar scenario (Equation 4-2) is applied separately to the significant infragravity swash data from the bar and rip sections of the bar-rip scenario. This is done to examine how the parameterization performs for the rip, and to compare the bar section of the bar-rip to the continuous bar scenario. Figure 4-13 below displays the parameterized data for the bar and rip sections of the bar-rip scenario with a 100 m rip.

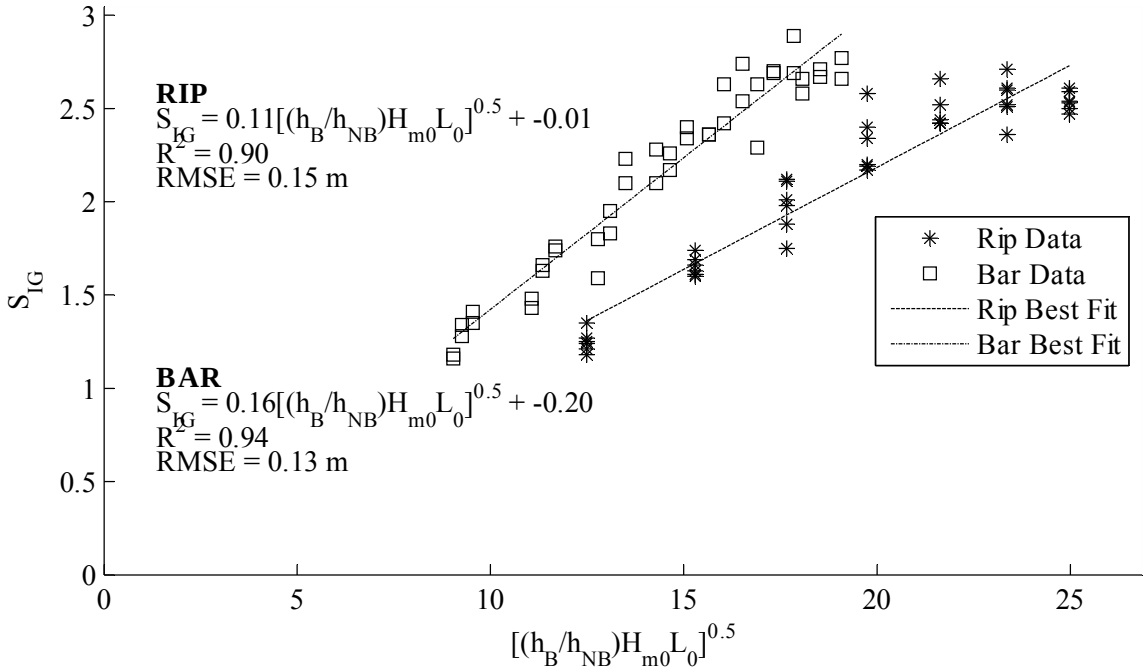

Figure 4-13 Bar-Rip Parameterization of Significant Infragravity Swash. Parameterization of data from the bar and rip sections of the bar-rip scenario. Data from both 100 m and 200 m rip widths are included in the plot.

Figure 4-13 shows that the response of significant infragravity swash to an increase in wave height is different for areas behind the bar and areas behind the rip. The significant infragravity swash data for areas behind the bar follow the same general trend as the data from the uniform alongshore bar scenario. The data from the area behind the rip respond differently however; the amount of infragravity energy does not increase as fast with an increase in the wave height. Also, the swash values for areas behind the rip reach a limit at a wave height of 3 m, while the swash values for areas behind the bar do not. This is an area that needs further research. Variables that describe the rip such as the rip width may need to be included to optimize the parameterization of infragravity energy for areas behind a rip.

4.5.1.4 Comparison of All Three Scenarios

In order to further investigate the effect of the bar-rip bathymetry on infragravity energy, the two-percent runup for all three bathymetric scenarios is compared. The alongshore distribution of two-percent runup for all three bathymetric scenarios for a 2 m wave height is shown in Figure 4-14. The bar location for the bar-rip and continuous alongshore bar is 100 / 2.00, and the rip width is 100 m.

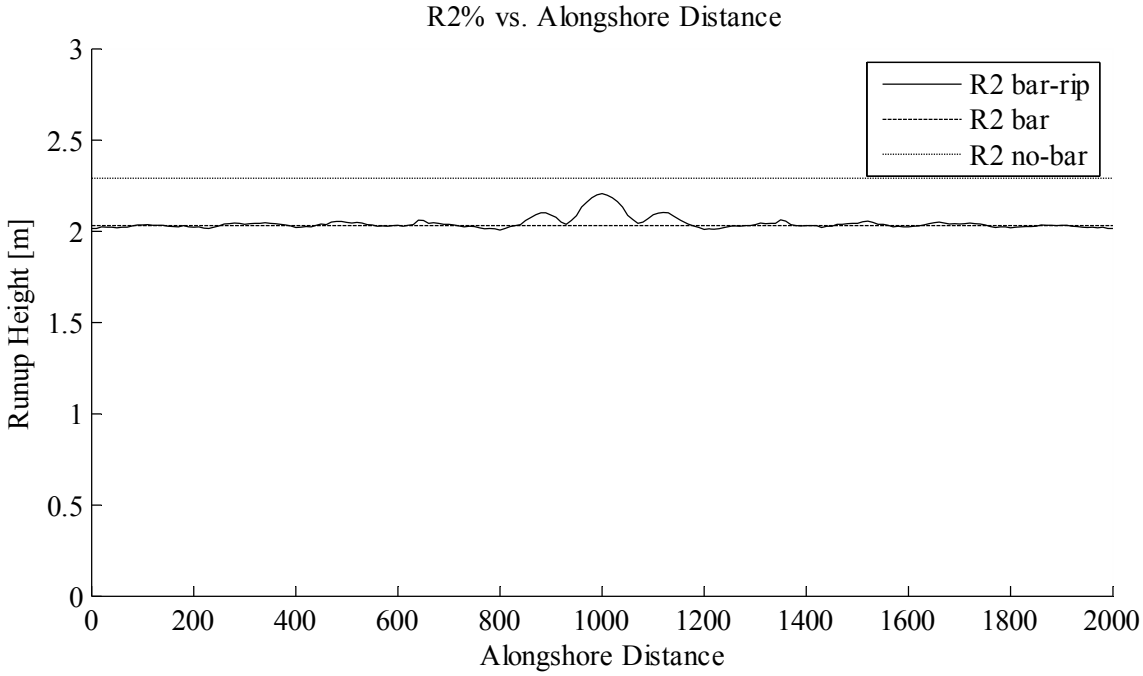

Figure 4-14 Comparison of All Three Bathymetric Scenarios: 100m Rip. The alongshore distribution of two-percent runup for all three bathymetric scenarios for the 100 m rip and a 2 m wave height.

The two-percent runup is higher in the area behind the rip, and also in the transition regions on either side of the rip when compared to the continuous alongshore bar scenario. Outside of the transition regions however, the two-percent runup value for the bar-rip scenario is very close to that of the continuous alongshore bar scenario. Therefore away from the rip, for areas behind the bar the rip does not have a major effect on the infragravity energy. Finally, at all alongshore locations the two-percent runup for the bar-rip scenario is lower than it is for the no-bar scenario. This suggests that during a storm event, for a bar-rip bathymetry with a 100 m rip width, all areas are protected to a certain degree by the presence of the sandbars.

To determine if the above is also true for a wider rip, Figure 4-15 compares the

two-percent runup for the bar-rip scenario with a 200 m rip width and the corresponding bar and no-bar scenarios.

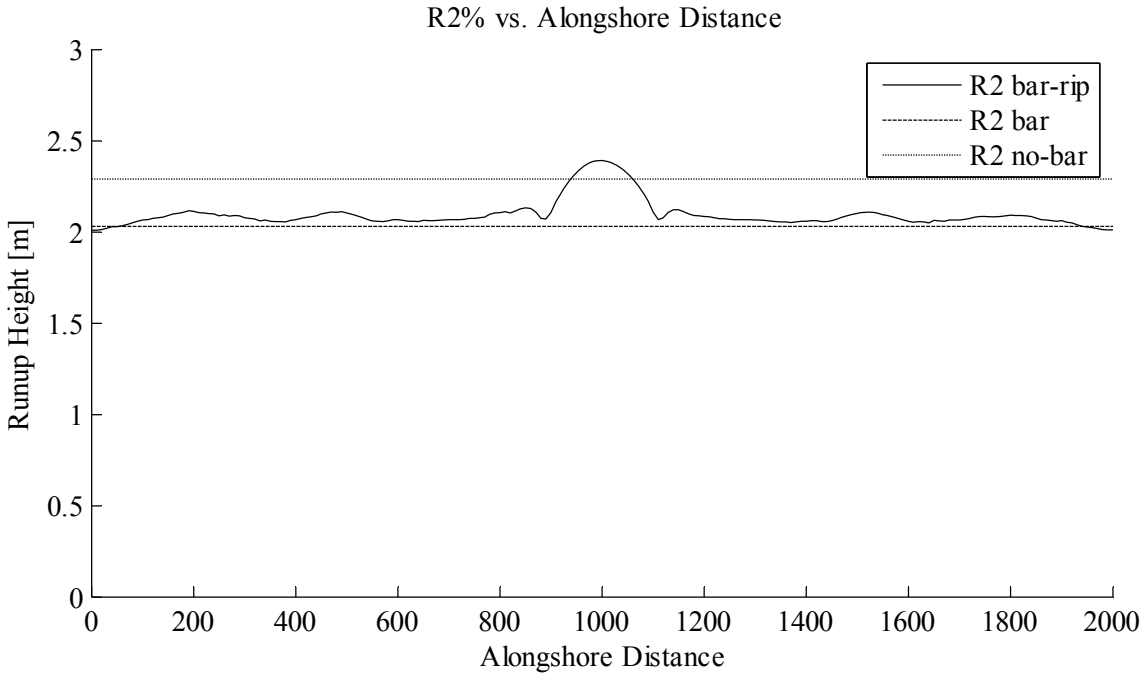

Figure 4-15 Comparison of All Three Bathymetric Scenarios: 200m Rip. The alongshore distribution of two-percent runup for all three bathymetric scenarios for the 200 m rip and a 2 m wave height.

The runup is greater for areas behind the bar in the bar-rip scenario than the bar scenario, and also for areas behind the center of the rip in the bar-rip scenario than the no-bar scenario, which is not expected. This is most likely due to small differences in the wave energy forcing at the offshore boundary between the two simulations, as there is an element of randomness in the process used by XBeach to determine the offshore wave energy.

Figure 4-15 shows that the bar-rip bathymetry with a 200 m rip results in a

different outcome than the 100 m rip. For the 100 m rip width, the two-percent runup elevation for the area behind the rip was less than that of the no-bar scenario; however for the 200 m rip width it is greater than the no-bar scenario. This shows that the infragravity energy for areas behind the center of the 200 m rip is not as affected by the presence of the sandbars on each side of the rip as areas behind the center of a 100 m rip. Therefore, for a bar-rip bathymetry with a 200 m rip, the area behind the center of the rip may not be protected by the presence of the sandbars during a storm event, and more erosion may occur.

4.5.2 Morphological Updating On

This section will briefly discuss results from the bar-rip simulations that were completed with morphological updating calculated, and will focus on qualitatively examining patterns of erosion on the beach. The version of XBeach used for this thesis over-predicts the amount of beach erosion that occurs, as the beach restoring processes that cause sand to accrete on the beach, and counter the amount of erosion that occurs are not included in the sediment transport equations. This causes an unrealistic amount of erosion on the beach. Because of this, erosion is not studied quantitatively. Figure 4-16 displays the cross-shore and alongshore distribution of erosion for the 100 / 2.00 bar with a 100 m rip and 3 m wave height. This represents typical qualitative erosion results for the bar-rip scenarios.

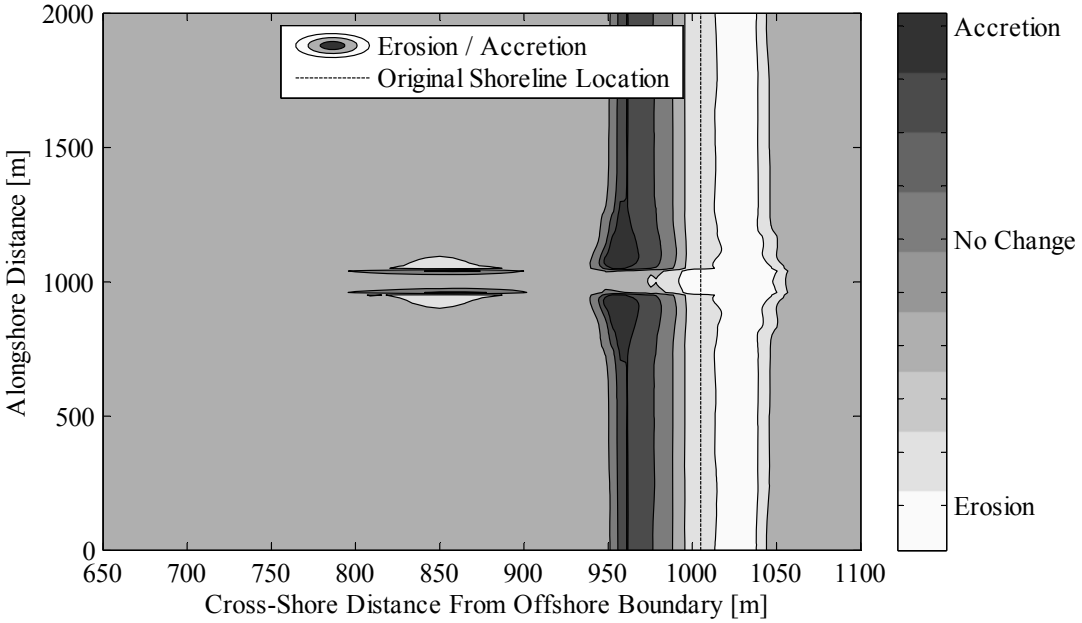

Figure 4-16 Bar-Rip Erosion. Alongshore and cross-shore distribution of erosion for the 100 / 2.00 bar 100 m rip scenario with 3 m wave height. Note that the dashed line represents the original shoreline location.

Note that the dashed line at 1005 m in the cross-shore direction represents the original shoreline location. The eroded sediment from the beach face is transported in the offshore direction. The largest areas of accretion are pockets on either side of the rip about 50 m offshore of the original shoreline. These pockets correspond to the section of the beach that was the most heavily eroded. There is not any significant accretion in the rip, which is most likely due to the presence of a strong current not allowing the sediment to settle.

The main alongshore patterns of erosion tend to follow the alongshore distribution of infragravity energy, as the amount of erosion is higher in areas where the amount of infragravity energy at the shoreline is also increased compared to other areas.

The amount of shoreline retreat is highest through the rip, where the highest amounts of infragravity energy also occur. The shoreline around the rip at the end of the run contains variations that match the peaks of the alongshore two-percent runup distribution as in Figure 4-14. Away from the rip, for areas directly behind the bar, the erosion is fairly constant in the alongshore direction. The alongshore patterns of erosion support the idea that the amount of erosion that occurs during storm events is highly influenced by the infragravity energy during those storm events (e.g. Ruggiero et al., 2001). There are two separate areas of erosion / accretion centered at 850 m in the cross-shore direction. These areas occur on either side of the rip, and may be due to a large slope between the bar and the rip causing an area of sediment to avalanche.

4.5.3 Bar-Rip Conclusions

The bar-rip scenario differs from the bar and no-bar scenarios in that it produces significant alongshore variation of the infragravity energy. The rip bathymetry may cause local refraction, turning the energy towards the bar on either side of the rip, consequently producing the peaks in the transition regions. An edge wave might also be produced as the infragravity energy travels through the rip. Further, it was determined that the infragravity energy is higher for areas behind the rip compared to the infragravity energy for areas behind the bar when the wave height is greater than about 60% of the bar depth.

The significant infragravity swash parameterization developed for the bar scenario was found to work well for the areas behind the bar. For areas behind the rip, variables such as the rip width may need to be added to the parameterization for

significant infragravity swash. This is an area that needs more research in order to determine a more optimal parameterization.

A rip width of 100 m results in less infragravity energy for all alongshore locations when compared to the no-bar scenario with the same amount of offshore wave energy. Increasing the rip width to 200 m changes this result, and the infragravity energy for the area behind the middle of the rip is close to that of the no-bar scenario. Therefore, for rip widths of approximately 200 m or greater, the bar no longer provides any protection from infragravity energy at the center of the rip.

Finally, erosion was qualitatively studied for the bar-rip scenario. The erosion is greater for the area behind the rip, and the shape of the new shoreline created follows the shape of the alongshore distribution of infragravity energy. The sediment from the area behind the rip is transported in the alongshore direction away from the rip, indicating a current velocity that does not allow the sediment to settle directly offshore from the rip.

5 SUMMARY AND CONCLUSIONS

The threat of extreme storm events leaves beaches vulnerable to large, destructive waves that have the ability to cause severe erosion on beaches. During these storm events, infragravity energy plays an important role in the amount of erosion that occurs. For this thesis, the influence of local bathymetric features such as continuous alongshore sandbars and bar-rips on infragravity energy at the shoreline were studied. This information can be used as part of a beach erosion vulnerability scale based on local nearshore bathymetry.

Numerical simulations were completed with the nearshore processes model XBeach, which shows particular skill in simulating infragravity energy (Roelvink et al., 2010). Simulations were completed for three different bathymetric scenarios; no-bar, bar, and bar-rip. The infragravity energy was analyzed in terms of two-percent runup and significant infragravity swash. Results from the bar and bar-rip scenarios were compared with the no-bar scenario to determine the influence of the bar and bar-rip bathymetries on the infragravity energy at the shoreline.

Compared with simulations for the no-bar scenario, the simulations for the continuous alongshore bar scenario showed that nearshore sandbars have the effect of decreasing the amount of infragravity at the shoreline. For the bar scenario, two sets of simulations were completed; one set of simulations considered mid-tide bar depths, while the second set considered extreme low-tide bar depths. The set of low-tide bar simulations resulted in a greater decrease in infragravity energy when compared to the no-bar scenario than the mid-tide simulations. Within each set, the location and depth of

the bar as well as the input wave height was modified between simulations. It was determined that when a sandbar is present in the local nearshore bathymetry, the amount of significant infragravity swash that reaches the shoreline is a function of wave height and a parameter that characterizes the percentage of the water column that is replaced by a sandbar when compared to a theoretical no-bar scenario. Using this information, the parameterization of significant infragravity swash from Stockdon et al. (2006) was modified to determine a new parameterization, shown below.

$$S_{IG} = \left(\frac{h_B}{h_{NB}}\right)^{\alpha} (H_0 L_0)^{0.5} \tag{5-1}$$

Simulations completed for the bar-rip scenario resulted in significant alongshore variation of infragravity energy. This variation was attributed to the presence of the rip. It was found that when the wave height is less than 57% of the bar depth, the infragravity energy is less for areas behind the rip than areas behind the bar. This was found to be correlated with the surf zone width. Areas with larger surf zone widths resulted in larger values of infragravity energy.

The parameterization determined from the bar data was tested against the bar-rip data. It was found that the parameterization performs well for the bar-rip data behind the bar, but needs improvement in order to determine an optimal fit for areas behind the rip. This area needs to be investigated further, and variables that describe the rip dimensions may need to be added to the parameterization.

Preliminary simulations were completed with morphological updating for the bar-rip scenario. The amount of shoreline retreat due to erosion was greater for areas behind the rip than areas behind the bar for large wave heights. The shape of the new

shoreline followed the shape of the alongshore distribution of infragravity energy, demonstrating the correlation between infragravity energy and erosion (e.g. Ruggiero et al., 2001).

The influence of nearshore bathymetric features on infragravity at the shoreline is an important piece of information that can be used as part of an erosion vulnerability scale for beaches. The work completed for this thesis has provided a better understanding of how infragravity energy is influenced by the presence of nearshore sandbars, and has shown that bathymetric features such as nearshore sandbars can reduce the impact of infragravity energy on a beach during storm events. In order to improve on this study, this research can be continued by considering different nearshore bathymetric features such as beach cusps, considering wave-current interaction, and by completing simulations with a new version of XBeach that has a better capability of quantitatively modeling beach erosion.

REFERENCES

Bagnold, R.A., 1956. The flow of cohesionless grains in fluids. Philosophical Transactions of the Royal Society of London, A 249(964), 235-297.

Baldock, T.E., Holmes, P., Horn, D.P., 1997. Low frequency swash motion induced by wave grouping. Coastal Engineering, 32, 197-222.

Battjes, J.A., 1974. Surf Similarity. Proceedings of the 14th Conference on Coastal Engineering, 466-480. American Society of Civil Engineers, New York.

Battjes, J.A., Janssen, J.P.F.M., 1978. Energy loss and setup due to breaking of random waves. Proceedings of 16th International Conference on Coastal Engineering, ASCE, 569-587.

Bowen, A.J., Guza, R.T. 1978., Edge waves and surf beat. Journal of Geophysical Research. 83(C4), 1913-1920.

Bowen, A.J., Inman, D.L., Simmons, V.P. 1968., Wave "set-down" and set-up. Journal of Geophysical Research, 73(8), 2569-2577.

Brock, J.C. Purkis, S.J., 2009. The emerging role of lidar remote sensing in coastal research and resource management. Journal of Coastal Research, SI(53), 1-5.

Brock, J.C., Wright, C.W., Sallenger, A.H., Krabill, W.B., Swift, R.N., 2002. Basis and methods of NASA airborne topographic mapper lidar surveys for coastal studies. Journal of Coastal Research, 18(1), 1-13.

Butt, T., Russell, P., 2000. Hydrodynamics and cross-shore sediment transport in the swash-zone of natural beaches: a review. Journal of Coastal Research, 16(2), 255-268.

Dally, W.R., Dean, R.G., Dalrymple, R.A., 1985. Wave height variation across beaches of arbitrary bottom profile. Journal of Geophysical Research, 90(C6), 11917-11927.

Davis, R.A., Wang, P., Silverman, B.R., 2000. Comparison of the performance of three adjacent and differently constructed beach nourishment projects on the gulf peninsula of Florida. Journal of Coastal Research, 16(2), 396-407.

Dean, R.G., Dalrymple, R.A., 2002. Coastal processes with engineering applications. Cambridge University Press, Cambridge, U.K.

Dean, R.G., Dalrymple, R.A., 1984. Water wave mechanics for engineers and scientists. World Scientific, Singapore.

Deigaard, R., 1989. Mathematical modelling of waves in the surf zone. Progress Report 69. ISVA, Technical University of Denmark, Lyngby, 47-59.

Dulou, C., Belzons, M., Rey, V., 2002. Bar formation under breaking wave conditions: a laboratory study. Journal of Coastal Research, 18(4), 802-809.

Emery, W.J., Thomson, R.E., 2001. Data analysis methods in physical oceanography. Elsevier, Second Edition.

ESRI (Environmental Systems Research Institute). 2011. www.esri.com.

Galapatti, R., Vreugdenhil, C.B., A depth-integrated model for suspended sediment transport. Report 83-7, Communications on Hydraulics, Department of Civil Engineering, Delft University of Technology.

Guza, R.T., Thornton, E.B., 1981. Wave set-up on a natural beach. Journal of Geophysical Research, 86(C5), 4133-4137.

Guza, R.T., Thornton, E.B., 1982. Swash oscillations on a natural beach. Journal of Geophysical Research, 87(C1), 483-491.

Hasselmann, K., Barnett, T.P., Bouws, E. Carlson, H., Cartwright D.E., et al., 1973. Measurements of wind-wave growth and swell decay during the Joint North Sea Wave Project (JONSWAP). Erganzungsheft zur Deutschen Hydrographischen Zeitschrift. Reihe A (80), Nr. 12.

Holman, R.A., 1981. Infragravity energy in the surf zone. Journal of Geophysical Research, 86(C7), 6442-6450.

Holman, R.A., 1986. Extreme value statistics for wave run-up on a natural beach. Coastal Engineering, 9, 527-544.

Holman, R.A., Bowen, A.J., 1984. Longshore structure of infragravity wave motions. Journal of Geophysical Research, 89(4), 6446-6452.

Holman, R.A., Sallenger, A.H. Jr., 1985. Setup and swash on a natural beach. Journal of Geophysical Research, 90(C1), 945-953.

Hughes, M.G., Masselink, G., Hanslow, D., Mitchell, D., 1998. Towards a better understanding of swash-zone sediment transport. Proceedings of Coastal Dynamics 1997, ASCE, 804-813.

Hunt, I.A. Jr., 1959. Design of seawalls and breakwaters. Journal of the Waterways, Harbors and Coastal Engineering Division, ASCE, 85(3), 123-152.

Huntley, D.A., 1976. Long-period waves on a natural beach. Journal of Geophysical Research, 81(36), 6441-6449.

Irish, J.L., McClung, J.K., Lillycrop, W.J., 2000. Airborne lidar bathymetry: the SHOALS system. PIANC Bulletin, 103, 43-53.

Longuet-Higgins, M.S., Stewart, R.W., 1962. Radiation stress and mass transport in gravity waves, with application to "surf-beats." Journal of Fluid Mechanics, 13, 481-504.

McCall, R.T., Van Thiel de Vries, J.S.M., Plant, N.G., Van Dongeren, A.R., Roelvink, J.A., Thompson, D.M., Reniers, A.J.H.M., 2010. Two-dimensional time dependent hurricane overwash and erosion modeling at Santa Rosa Island. Coastal Engineering, 57, 668-683.

McComb, R., Moh, Young-Kyu., Schiller, A.R. 2011., Measuring long-run economic effects of natural hazard. Natural Hazards, 58,559-566.

Miche, A., 1951. Exposes a l'action de la houle. Ann, Ponts Chaussees, 121, 285-319.

Munk, W.H., 1959. Surf Beats. Eos Trans. AGU, 30,849-854.

McCowan, J., 1894. On the highest wave of permanent type. Phil. Mag., 38, 351-357.

Parsons, G.R., Powell, M., 2001. Measuring the cost of beach retreat. Coastal Management, 29,91-103.

Plant, N.G., Edwards, K.L., Kaihatu, J.M., Veeramony, J., Hsu, L., Holland, K.T., 2009. The effect of bathymetric filtering on nearshore processes. Coastal Engineering 56, 584-493.

Raubenheimer, B., Guza, R.T., 1996. Observations and predictions of run-up. Journal of Geophysical Research, 101(C10), 25,575-25,587.

Raubenheimer, B., Guza, R.T., 1995. Swash on a gently sloping beach. Journal of Geophysical Research, 100(C5), 8751-8760.

Reniers, A.J.H.M., Roelvink, J.A., Thornton, E.B., 2004. Morphodynamic modeling of an embayed beach under wave group forcing. Journal of Geophysical Research, 109, C01030.

Robertson, V., Zhang, K., Whitman, D., 2007. Hurricane-induced beach change derived from airborne laser measurements near Panama City, Florida. Marine Geology, 237, 191-205.

Roelvink, J.A., 1993. Dissipation in random wave groups incident on a beach. Coastal Engineering, 19, 127-150.

Roelvink, D., Reniers, A., van Dongeren, A.,van Thiel de Vries, J.,Lescinski, J.,McCall, R., 2010. XBeach model description and manual. Unesco-IHE Institute for Water Education, Deltares and Delft University of Technology.

Roelvink, D., Reniers, A., van Dongeren, A., van Thiel de Vries, J., McCall, R., Lescinski, J., 2009. Modelling storm impacts on beaches, dunes and barrier islands. Coastal Engineering, 56, 1133-1152.

Ruggiero, P., Komar, P.D., McDougal, W.G., Marra, J.J., Beach, R.A., 2001. Wave runup, extreme water levels and the erosion of properties backing beaches. Journal of Coastal Research, 17(2), 407-419.

Ruggiero, P., Holman, R.A., Beach, R.A., 2004. Wave run-up on a high energy dissipative beach. Journal of Geophysical Research. 109, C06025.

Sallenger, A.H., Jr., 2000. Storm impact scale for barrier islands. Journal of Coastal Research, 16(3), 890-895. West Palm Beach (Florida). ISSN 0749-0208.

Saville, T., 1961. Experimental determination of wave set-up. Proceedings of the 2nd Technical Conference on Hurricanes, 242.

Schaffer, H.A., Madsen, P.A., Deigaard, R., 1993. A Boussinesq model for waves breaking in shallow water. Coastal Engineering, 20, 185-202.

Soulsby, R., 1997. Dynamics of marine sands. Thomas Telford Publications, London.

Stockdon, H.F., Holman, R.A., Howd, P.A., Sallenger, A.H. Jr., 2006. Empirical parameterization of setup, swash, and runup. Coastal Engineering, 53, 573-588.

Suhayda, J.N., 1974. Standing waves on beaches. Journal of Geophysical Research, 79(21), 3065-3071.

Svendsen, I.A., 1984. Wave heights and set-up in a surf zone. Coastal Engineering, 8, 303-329.

Svendsen, I.A., 2006. Introduction to nearshore hydrodynamics. World Scientific Publishing Co.

Tucker, M.J., 1950. Surf beats: sea waves of 1 to 5 minute period. Proceedings of the Royal Society of London, A 202, 565-573.

Van Dongeren, A.R., Reniers, A.J.H.M., Battjes, J.A., Svendsen, I.A., Numerical modeling of infragravity wave response during Delilah. Journal of Geophysical Research, 108 (C9), 3288.

Van Dorn, W.G., 1976. Breaking invariants in shoaling waves. Journal of Geophysical Research, 83, 2981-2987.

Wozencraft, J., Millar, D., 2005. Airborne lidar and integrated technologies for coastal mapping and nautical charting. Marine Technology Society Journal, 39(3), 27-34.

Wright, L.D., Nielsen, P., Shi, N.C., List, J.H., 1986. Morphodynamics of a bar-trough surf zone. Marine Geolory, 70, 251-285.

Wright, L.D., Short, A.D., 1984. Morphodynamic variability of surf zones and beaches: a synthesis. Marine Geology, 56, 93-118.

APPENDIX

Table A-1. R_2 and S_{IG} for a bar bathymetry simulations.

Bar Bathymetry Data				
$\mathbf{x_B}$	$\mathbf{h_B}$	$\mathbf{H_{m0}}$	$\mathbf{R_2}$	$\mathbf{S_{IG}}$
50	1.20	1.0	1.35	1.00
50	1.20	1.5	1.63	1.19
50	1.20	2.0	1.87	1.47
50	1.20	2.5	2.11	1.67
50	1.20	3.0	2.40	2.03
50	1.20	3.5	2.51	2.12
50	1.20	4.0	2.72	2.42
75	1.60	1.0	1.46	1.09
75	1.60	1.5	1.75	1.29
75	1.60	2.0	1.90	1.50
75	1.60	2.5	2.22	1.77
75	1.60	3.0	2.39	2.20
75	1.60	3.5	2.55	2.21
75	1.60	4.0	2.74	2.58
100	2.00	1.0	1.53	1.24
100	2.00	1.5	1.76	1.34
100	2.00	2.0	2.03	1.64
100	2.00	2.5	2.23	1.79
100	2.00	3.0	2.42	2.12
100	2.00	3.5	2.60	2.29
100	2.00	4.0	2.71	2.45
125	2.40	1.0	1.63	1.36
125	2.40	1.5	1.90	1.55
125	2.40	2.0	2.14	1.80
125	2.40	2.5	2.33	1.99
125	2.40	3.0	2.52	2.36
125	2.40	3.5	2.67	2.53
125	2.40	4.0	2.73	2.58

x_B	h_B	H_{m0}	R_2	S_{IG}
150	2.75	1.0	1.60	1.28
150	2.75	1.5	1.97	1.53
150	2.75	2.0	2.14	1.85
150	2.75	2.5	2.37	2.21
150	2.75	3.0	2.56	2.35
150	2.75	3.5	2.65	2.52
150	2.75	4.0	2.76	2.50
200	3.50	1.0	1.62	1.43
200	3.50	1.5	2.07	1.72
200	3.50	2.0	2.29	2.15
200	3.50	2.5	2.41	2.23
200	3.50	3.0	2.61	2.48
200	3.50	3.5	2.73	2.59
200	3.50	4.0	2.84	2.64
50	0.60	1.0	1.13	0.80
50	0.60	1.5	1.42	0.92
50	0.60	2.0	1.7	1.15
50	0.60	2.5	1.88	1.3
50	0.60	3.0	2.11	1.55
50	0.60	3.5	2.34	1.75
50	0.60	4.0	2.48	2.00
75	1.00	1.0	1.29	0.89
75	1.00	1.5	1.60	1.13
75	1.00	2.0	1.80	1.25
75	1.00	2.5	2.08	1.53
75	1.00	3.0	2.28	1.82
75	1.00	3.5	2.45	2.03
75	1.00	4.0	2.61	2.29
100	1.40	1.0	1.36	0.94
100	1.40	1.5	1.66	1.15
100	1.40	2.0	1.90	1.45
100	1.40	2.5	2.11	1.64
100	1.40	3.0	2.32	1.90
100	1.40	3.5	2.47	2.06
100	1.40	4.0	2.67	2.29

x_B	h_B	H_{m0}	R_2	S_{IG}
125	1.80	1.0	1.48	1.17
125	1.80	1.5	1.72	1.26
125	1.80	2.0	1.96	1.40
125	1.80	2.5	2.22	1.73
125	1.80	3.0	2.42	2.04
125	1.80	3.5	2.53	2.12
125	1.80	4.0	2.70	2.39
150	2.15	1.0	1.60	1.29
150	2.15	1.5	1.81	1.46
150	2.15	2.0	2.04	1.57
150	2.15	2.5	2.27	1.87
150	2.15	3.0	2.44	2.10
150	2.15	3.5	3.59	2.29
150	2.15	4.0	2.69	2.42
200	2.90	1.0	1.63	1.45
200	2.90	1.5	1.95	1.62
200	2.90	2.0	2.21	1.91
200	2.90	2.5	2.35	2.11
200	2.90	3.0	2.52	2.20
200	2.90	3.5	2.63	2.42
200	2.90	4.0	2.70	2.58

Table A-2. R_2 and S_{IG} for all bar-rip bathymetry simulations.

100 m Rip Width														
x_B	h_B	H_{m0}	R_{2bar}		R_{2trans}		R_{2rip}		S_{IGbar}		$S_{IGtrans}$		S_{IGrip}	
			Avg	Max	Avg	Max	Avg	Max	Avg	Max	Avg	Max	Avg	Max
100.00	2.00	1.00	1.55	1.57	1.51	1.56	1.50	1.53	1.11	1.16	1.02	1.14	1.10	1.18
100.00	2.00	1.50	1.80	1.82	1.81	1.84	1.86	1.91	1.38	1.43	1.41	1.46	1.53	1.60
100.00	2.00	2.00	2.03	2.06	2.08	2.10	2.16	2.21	1.54	1.59	1.64	1.70	1.71	1.75
100.00	2.00	2.50	2.30	2.37	2.39	2.43	2.44	2.48	1.94	2.10	2.14	2.23	2.16	2.20
100.00	2.00	3.00	2.47	2.54	2.56	2.58	2.63	2.66	2.19	2.36	2.42	2.45	2.40	2.42
100.00	2.00	3.50	2.61	2.65	2.68	2.70	2.74	2.76	2.24	2.29	2.39	2.41	2.32	2.36
100.00	2.00	4.00	2.76	2.83	2.84	2.87	2.89	2.92	2.49	2.58	2.60	2.62	2.40	2.50

x_B	h_B	H_{m0}	R_{2bar}		R_{2trans}		R_{2rip}		S_{IGbar}		$S_{IGtrans}$		S_{IGrip}	
			Avg	Max	Avg	Max	Avg	Max	Avg	Max	Avg	Max	Avg	Max
150.00	2.75	1.00	1.65	1.66	1.58	1.62	1.55	1.56	1.24	1.28	1.10	1.19	1.18	1.25
150.00	2.75	1.50	1.98	2.02	1.93	1.97	1.89	1.92	1.63	1.66	1.52	1.62	1.59	1.66
150.00	2.75	2.00	2.14	2.20	2.13	2.18	2.16	2.20	1.82	1.95	1.79	1.93	1.82	1.88
150.00	2.75	2.50	2.31	2.40	2.35	2.39	2.39	2.42	2.00	2.17	2.09	2.18	2.13	2.17
150.00	2.75	3.00	2.55	2.64	2.59	2.63	2.63	2.66	2.43	2.63	2.56	2.62	2.51	2.52
150.00	2.75	3.50	2.68	2.78	2.73	2.76	2.76	2.77	2.49	2.69	2.59	2.67	2.49	2.52
150.00	2.75	4.00	2.79	2.89	2.85	2.88	2.87	2.89	2.50	2.67	2.58	2.65	2.41	2.47
200.00	3.50	1.00	1.66	1.68	1.59	1.62	1.57	1.60	1.33	1.35	1.18	1.23	1.28	1.35
200.00	3.50	1.50	2.04	2.05	1.98	2.00	1.93	1.94	1.71	1.74	1.57	1.62	1.65	1.69
200.00	3.50	2.00	2.31	2.33	2.28	2.30	2.26	2.27	2.05	2.10	1.94	2.04	1.97	2.01
200.00	3.50	2.50	2.44	2.49	2.44	2.48	2.44	2.46	2.23	2.34	2.16	2.29	2.15	2.19
200.00	3.50	3.00	2.61	2.68	2.62	2.65	2.63	2.64	2.38	2.54	2.41	2.50	2.40	2.42
200.00	3.50	3.50	2.74	2.83	2.77	2.79	2.79	2.80	2.53	2.69	2.59	2.66	2.50	2.51
200.00	3.50	4.00	2.86	2.97	2.89	2.92	2.91	2.93	2.53	2.66	2.57	2.62	2.51	2.53
200 m Rip Width														
x_B	h_B	H_{m0}	R_{2bar}		R_{2trans}		R_{2rip}		S_{igbar}		$S_{igtrans}$		S_{igrip}	
			Avg	Max	Avg	Max	Avg	Max	Avg	Max	Avg	Max	Avg	Max
100.00	2.00	1.00	1.53	1.55	1.46	1.50	1.50	1.51	1.14	1.18	1.06	1.22	1.17	1.21
100.00	2.00	1.50	1.85	1.87	1.86	1.95	2.01	2.04	1.45	1.48	1.50	1.68	1.72	1.74
100.00	2.00	2.00	2.07	2.12	2.15	2.29	2.36	2.39	1.66	1.80	1.84	2.03	2.10	2.12
100.00	2.00	2.50	2.42	2.48	2.53	2.65	2.71	2.73	2.10	2.28	2.33	2.48	2.55	2.58
100.00	2.00	3.00	2.47	2.54	2.56	2.58	2.63	2.66	2.19	2.36	2.42	2.45	2.40	2.42
100.00	2.00	3.50	2.67	2.77	2.81	2.93	2.99	3.02	2.44	2.63	2.60	2.64	2.60	2.60
100.00	2.00	4.00	2.78	2.88	2.92	3.02	3.07	3.09	2.49	2.66	2.63	2.68	2.53	2.54
150.00	2.75	1.00	1.62	1.64	1.51	1.54	1.52	1.53	1.31	1.34	1.14	1.26	1.22	1.24
150.00	2.75	1.50	1.94	1.97	1.87	1.91	1.93	1.94	1.59	1.63	1.47	1.60	1.62	1.63
150.00	2.75	2.00	2.16	2.21	2.18	2.27	2.30	2.32	1.74	1.83	1.75	1.92	1.96	1.98
150.00	2.75	2.50	2.39	2.46	2.45	2.55	2.59	2.60	2.10	2.26	2.19	2.34	2.38	2.40
150.00	2.75	3.00	2.59	2.68	2.65	2.75	2.79	2.80	2.26	2.42	2.36	2.44	2.43	2.44
150.00	2.75	3.50	2.75	2.84	2.83	2.91	2.95	2.97	2.55	2.70	2.63	2.64	2.59	2.61
150.00	2.75	4.00	2.76	2.83	2.87	2.97	3.01	3.03	2.55	2.71	2.65	2.69	2.60	2.61

x_B	h_B	H_{m0}	R_{2bar}		R_{2trans}		R_{2rip}		S_{igbar}		$S_{igtrans}$		S_{igrip}	
			Avg	**Max**	**Avg**	**Max**	**Avg**	**Max**	**Avg**	**Max**	**Avg**	**Max**	**Avg**	**Max**
200.00	3.50	1.00	1.64	1.66	1.53	1.57	1.53	1.54	1.37	1.41	1.19	1.30	1.26	1.27
200.00	3.50	1.50	2.08	2.11	1.95	2.00	1.98	1.99	1.70	1.76	1.48	1.59	1.60	1.61
200.00	3.50	2.00	2.33	2.36	2.23	2.27	2.30	2.31	2.14	2.23	1.92	2.05	2.09	2.11
200.00	3.50	2.50	2.48	2.53	2.44	2.50	2.52	2.53	2.28	2.40	2.21	2.31	2.33	2.34
200.00	3.50	3.00	2.66	2.73	2.68	2.73	2.77	2.78	2.58	2.74	2.61	2.66	2.65	2.66
200.00	3.50	3.50	2.78	2.88	2.84	2.91	2.93	2.94	2.72	2.89	2.73	2.76	2.70	2.71
200.00	3.50	4.00	2.86	2.96	2.89	2.95	2.99	3.00	2.60	2.77	2.64	2.67	2.59	2.59

VITA

Name:	Nicholas Carroll Cox
Address:	Department of Civil Engineering Texas A&M University 3136 TAMU College Station, TX 77843-3136 USA
Email Address:	nickcox@tamu.edu
Education:	B.S., Civil Engineering, Clemson University, 2009 M.S., Civil Engineering, Texas A&M University, 2011